Growth instabilities of vicinal crystal surfaces during Molecular Beam Epitaxy

Dissertation
zur Erlangung des Grades des
Doktors der Naturwissenschaften
Dr. rer. nat.
vorgelegt am Fachbereich Physik
der Universität Duisburg-Essen

von
Jouni Kallunki
aus Vantaa
Essen, im Mai 2003

Tag der mündlichen Prüfung: 30.07.2003

1. Gutachter: Prof. Dr. J. Krug
2. Gutachter: Prof. Dr. D. Wolf

Abstract

In this work the growth instabilities of vicinal crystal surfaces during MBE are studied theoretically. The vicinal surfaces grow in a step-flow mode, where steps present due to a small miscut relative to a high symmetry direction of a crystal, propagate due to a deposition flux. The number of the steps remains constant as nucleation of atomic island is suppressed by the presence of steps.

In the first part the models used to describe the step-flow growth are presented. Also the different microscopic processes taking place on a growing surfaces are discussed at length, as the large scale morphology is determined by the relative relevance of these processes. The dynamics of atoms diffusing along the atomic steps, which are of central importance for the step-flow growth, are addressed in particular.

The main subject of this thesis are the step meandering instabilities, which lead to a ripple morphology on a growing surface. The atomic steps become wavy due to growth instabilities as they propagate. The wave patterns formed on the steps are in-phase over multiple steps, thus leading to long ripples running in the direction of the step-train. The wavelength of the pattern, *i.e* the typical separation of the ripples, is set by the competition between the driving force (the deposition flux) and the relaxation of the steps. In equilibrium the steps are straight. In growth experiments the typical scale of the ripples lies in the nanometer scale $l \sim 10 - 1000$ nm. The dynamics of these instabilities are studied employing Monte-Carlo simulations and partial differential equations, describing the time evolution of the steps. A quantitative comparison between these two approaches is made. The results are also related to recent experimental results.

In the last part the destabilization of the step-flow growth due to the appearance of new steps is considered. New steps may result from either island nucleation on terraces, or due to the appearance of vacancy islands that are formed when a strongly deformed step crosses itself.

Contents

Chapter 1

Introduction

When left alone all materials tend to their equilibrium state. The equilibrium state is the one that minimizes the free energy of the system and the probability of the occurrence of a particular state is given by the Boltzmann distribution $P \sim \exp(-\beta E)$, where E is the energy of the state and $\beta = (kT)^{-1}$ the inverse thermal energy. In the equilibrium state the memory of the system of its past has been completely washed away and its macroscopic properties can be derived from equilibrium thermodynamics, which has been studied for a long period of time and is by now fairly well understood.

However, the majority of materials we come in contact with are not in equilibrium. In gases and liquids the constituents, *i.e.* atoms or molecules can move quite freely and the system can reach its equilibrium state rapidly. This is not true for solid materials, where the atoms are bounded to their positions and the system may reach its equilibrium state only after astronomical time. Many of the properties of solid materials, such as thermal or electrical conductivities can be described by equilibrium statistical mechanics since they involve rapidly relaxing degrees of freedom like electron density or lattice vibrations (phonons). This is in contrast to the shape of a macroscopic object or the densities of the composites of the object, which are for all practical purposes frozen to their values acquired when it was formed. Thus in order to understand these properties of solid materials, one has to deal with the process of growth of the object, which takes place in a non-equilibrium state. A good example of such a problem is the shape of a crystal. The equilibrium shape can be deduced from the Wulff construction, once the surface free energy is known; however the crystals practically never have their equilibrium shape as the relaxation to it takes enormously long time.

The question how do atoms or molecules assemble to form a macroscopic body is a very difficult one. It depends also strongly on the environment in which the growth takes place. Generally the growth starts by formation of a small nucleus through a fluctuation, on which new material attaches. Whether the growth takes place in vacuum or in a solution or melt strongly affects the crystal, as the dynamics of the processes are

very different. Also the rate of the growth and how different chemical composites arrive to the growing crystal have an impact on the material. Additional complication for growth from melt or solution is that there may be several nuclei instead of just one. As these nuclei grow and eventually coalesce, their structures have different orientations which leads to *grain boundaries* in the crystal. Also vacancies inside the crystal can be formed this way. To remove these imperfections, originating from the growth process, from the crystal takes extremely long time as it would require mass transport over long distances and thus they are always present and affect the properties of materials.

During growth most of the dynamics takes place on the surface of the growing object. The molecules arrange themselves on the surface according to their dynamics and the formed structures are then buried inside the crystal as new material arrives. Thus during growth it suffices to consider only the surface of the crystal. Clearly the rate of the growth is essential as it determines the time molecules remain mobile on the surface.

In this work crystal growth in a ultra high vacuum on an existing template is considered. The formed crystals are then single crystallites and have no grain boundaries or vacancies in the bulk. New material arrives to the substrate through a deposition beam and all dynamics take place on the surface. This artificial and highly idealized situation provides a possibility to study the *intrinsic* dynamics of the growth, without complications due to interaction with the solution or melt (or their dynamics), or difficulties arising from multiple nuclei. The growth is subjected to various instabilities, which cause self-organized patterns to form on the surface. It turns out that even the simple growth of pure material is unstable. Depending on the orientation of the surface, either mounds or ripples are formed on the surface, due to the suppression of inter-layer mass transport. In this light it seems that instabilities and pattern formation is a generic feature of growth processes rather than an exception and avoiding self-organized structures requires careful tuning of parameters.

Outline

In the second Chapter a short review of the growth method considered in this work, the molecular beam epitaxy, is given. Also some generic features of this growth and some of the common instabilities are presented. The third chapter consist of a reminder for the theoretical models, most importantly the SOS and BCF models, employed in the rest of this thesis. Also a few remarks on the Monte Carlo simulation methods are made, as MC simulation results will be presented in the following chapters. The topic of the fourth chapter are equilibrium dynamics and thermodynamic fluctuations, they serve as a starting point for the studies of the non-equilibrium dynamics. The fifth chapter includes the bulk of the results of this thesis. The step meandering growth instabilities are discussed in detail and simulation results supporting the theories are

presented. The last chapter is a short discussion about the ultimate fate of step-flow growth and includes some rather preliminary results on this topic.

List of symbols

Symbol x	Dimension $[x]$	
a	m	Lattice constant
$\Omega\,(=a^2)$	m^2	Atomic area
$\beta\,(=(kT)^{-1})$	eV^{-1}	Inverse thermal energy
$\Gamma_x\,(=\Gamma_0\,e^{\beta E_X})$	s^{-1}	Rate of an atomic process -
E_x	eV	- corresponding activation energy
$\Gamma_0\,(\sim 10^{-12}\mathrm{s}^{-1})$	s^{-1}	frequency of lattice vibrations.
ℓ	m	Terrace width
ℓ_D	m	Nucleation length on a flat terrace
F	$\mathrm{m}^{-2}\mathrm{s}^{-1}$	Deposition flux
D	$\mathrm{m}^2\mathrm{s}^{-1}$	Terrace diffusion constant
c	m^{-2}	Adatom concentration on a terrace
$\ell_{ES}\,(=ae^{\beta E_{ES}}-a)$	m	Ehrlich-Schwoebel length -
E_{ES}	eV	- Ehrlich-Schwoebel barrier
ζ	m	Step position
$\tilde{\gamma}$	$\mathrm{eV\,m}^{-1}$	Step stiffness
κ	m^{-1}	Step curvature
D_s	$\mathrm{m}^2\mathrm{s}^{-1}$	Step-edge diffusion constant
σ	$\mathrm{m\,eV}^{-1}\,\mathrm{s}^{-1}$	Adatom mobility along the steps
$L_k\,(=(a/2)\,e^{\beta E_k})$	m	Thermal kink distance -
E_k	eV	- kink formation energy
L_D	m	Nucleation length along the steps
$L_{KES}\,(=ae^{\beta E_{kr}}-a)$	m	Kink-Ehrlich-Schwoebel length -
E_{kr}	eV	- additional energy barrier due to kink-rounding in step-edge diffusion (kink-Schwoebel barrier)
ρ_{isl}	m^{-2}	Island density on a surface

Chapter 2

Molecular Beam Epitaxy (MBE)

Crystals can be grown in numerous different ways. In this work only one particular method, namely the deposition of new material through a molecular beam in an ultra high vacuum (UHV), will be considered. The method considered here is called Molecular Beam Epitaxy (MBE) [1]. The main advantage of the vacuum methods is their simplicity compared to growth from a solution, melt or a gas phase. In these cases one needs to deal with the transport of the matter and energy in the fluid phase, which makes the theoretical modeling extremely complicated. From the simplicity also follows a high degree of controllability; contrary to the vacuum methods where the thickness of the deposited layer can be controlled with atomic resolution, controlling the amount of deposited material in fluid phase is next to impossible [66].

Molecular beam epitaxy has been around for over 30 years and there is extensive literature about the subject. A short description will be given here, more detailed reviews can be found in text books [26, 49, 66] and review articles [37, 71]. A cartoon of the MBE is presented in Fig. 2.1. A substrate is placed in an UHV chamber and a piece of material which is to be deposited is heated, so that a cloud of atoms (or molecules) with Maxwell distributed velocities forms near the sample. When the shutter is open, a beam of atoms flies out of the source and meets the substrate. During the flight the beam atoms do not interact with each others and when colliding with the substrate they either stick to it or are reflected. A vacuum pump maintaining the vacuum then removes the reflected atoms. By controlling the shutter openings the amount of deposited matter can be controlled with an accuracy of a single monolayer. By using multiple wafers and opening the shutters subsequently complex multi-layer structures may be manufactured [26].

The type of growth where the deposited material is of different chemical composition than the substrate is called *heteroepitaxy*. The opposing case where the substrate

[1] *epitaxy="arrangement on"*. A situation where the deposit and the substrate crystal lattices have a well defined relative orientation is generally called epitaxy [60].

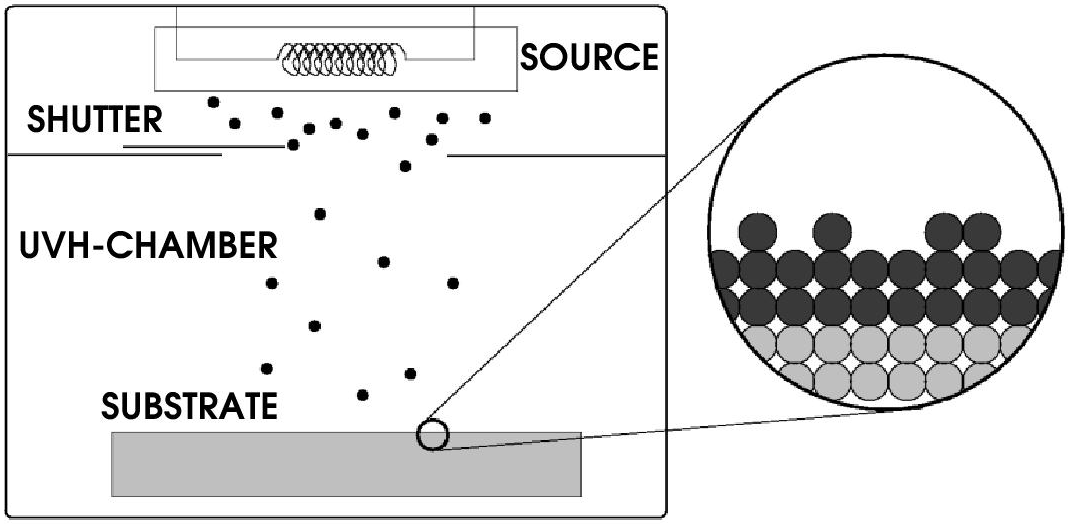

Figure 2.1: A cartoon illustrating the MBE deposition method. Heating a sample creates a beam of molecules, traveling through the ultra-high-vacuum. Eventually molecules attach to the substrate, adapting to its crystal structure

and the adsorbate are of the same kind is called *homoepitaxy*. Obviously the heteroepitaxial case is the relevant one for technical applications. When dealing with heteroepitaxy a major complication arises from the different "sizes" of the materials; the lattice constants a_{subs},a_{dep} of the materials differ, which causes elastic strain in the adlayers [66, 71]. If the lattice misfit $\epsilon \equiv (a_{subs} - a_{dep})/a_{subs}$ is very large, the strain is relaxed by formation of droplets on the substrate surface, leaving parts of the substrate exposed. This type of growth is commonly called *Volmer-Weber* growth. The opposite case, where the adsorbed material forms a complete film on the substrate (the adsorbate is said to *wet* the substrate), is refered as *Frank-Van der Merve* type. The interpolation of these two types is called *Stranski-Krastanov* growth. In this case a wetting layer is first formed on the substrate surface, but as the strain accumulates as the film thickness increases, droplets are eventually formed on the surface in order to relax the elastic strain [66, 71, 83].

Despite of the technical (and theoretical!) interest on the heteroepitaxy, only homoepitaxial growth will be considered in this work. Already homoepitaxy has turned out to be a field with a variety of complex phenomena; different kinetic instabilities influence the surface morphology, causing structure formation on the surface. Modeling the growth kinetics, even without the complication of lattice misfits, is a difficult task. However significant success has been reached in recent years laying the foundation for the studies of heteroepitaxy.

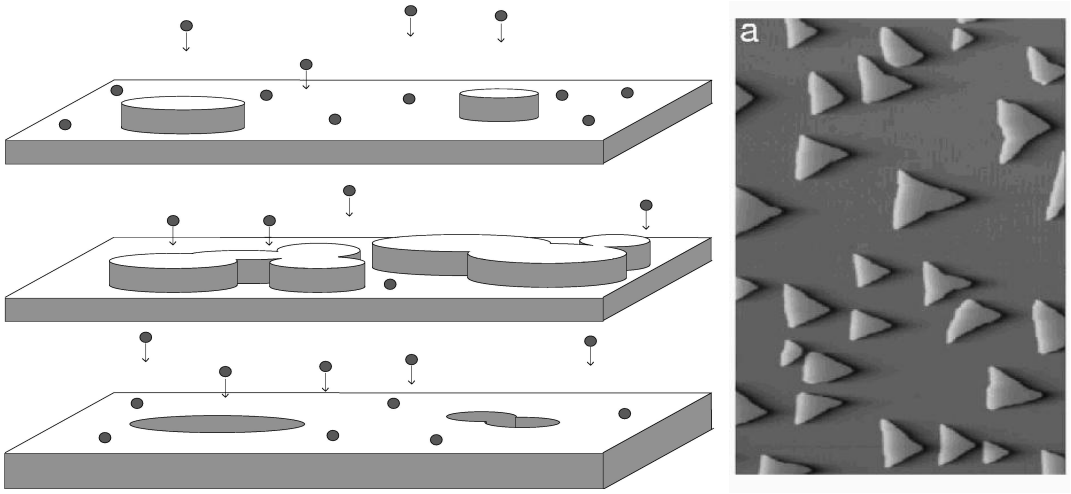

Figure 2.2: A schematic picture of layer-by-layer growth on a singular surface. To the right: a STM topograph of a Pt(1 1 1) surface after deposition of 0.15 ML of material. Taken from Ref. [30]. The triangular island shape reflects the hexagonal symmetry of the Pt(1 1 1) surface.

2.0.1 Structure of growing surfaces

How the surface of the growing crystal evolves depends strongly on the microscopic structure of the surface. The surface consist of flat ***terraces***, *i.e.* pieces of a surface having an orientation that coincides with one of the high symmetry axes of the crystal, atomic ***steps*** separating the terraces and ***adatoms***, diffusing on the surface. The terraces themselves may also have a structure due to surface reconstruction . Depending on the chemical composition, a unit cell on a terrace may be a dimer or a larger composition of atoms, rather than a single crystal atom [15,71]. Surface reconstructions break the isotropy of the terraces, causing the diffusion rate, step energies etc. to depend on the direction [66]. In the following complications arising from the reconstructions are neglected.

The atoms arrive from the beam to the surface at rate F (particles/unit area $[F] = m^{-2}s^{-1}$) and diffuse on the surface by hopping at rate Γ_D to neighboring lattice sites, until they meet a step where they stick, or alternatively meet another adatom and form a dimer [2]. The hopping rate Γ_D is connected to the (tracer-)***Diffusion coefficient*** by $D = (1/4)a^2\Gamma_D$, where a is the lattice constant (assumed isotropic). Being a thermally activated process, the hopping rate has a Arrhenius type temperature dependence $\Gamma_D = \Gamma_0 \exp(-\beta E_S)$. Here $\beta = (kT)^{-1}$ is the thermal energy, $\Gamma_0 \sim 10^{12}s^{-1}$ the trial frequency and E_S is the height of the energy barrier separating the neighboring lattice

[2]Actually also clusters of atoms can diffuse; cluster diffusion is neglected in this work

sites [1, 2, 53] .

The average orientation of the surface is essential; if the surface normal is oriented along a crystal symmetry axis, initially the whole surface can be considered as a large single terrace and no steps are present. Such surfaces are called *singular* or *high symmetry* surfaces. As the steps are absent at the very beginning of the deposition, the adatoms can only stick to other adatoms, forming islands. The nucleation of new islands increases the step density on the surface, creating attachment sites for freshly landed adatoms. Eventually most of the adatoms stick to the island and the island density ceases to increase [39]. The asymptotic island density ρ_{isl} depends on the ratio of the deposition and diffusion rates through [6, 39, 71]

$$\rho_{isl} = \ell_D^{-2} \sim \left(\frac{\Omega F}{\Gamma_D}\right)^{\gamma}. \tag{2.1}$$

Here Ω is the atomic area and ℓ_D is the mean distance between nucleation centers on a terrace, often also called diffusion length, and the exponent γ depends on the type of the islands (fractal or compact islands) and size of a stable nucleus $i^\star + 1$ [39, 66]. In this work the dimers as assumed stable $i^\star = 1$ and only compact island are considered, leading to the value $\gamma = 1/6$ for the exponent [71, 96]. After the nucleation ceases, the islands grow through capture of adatoms and eventually start coalescing, finally filling an entire atom layer and a new layer starts growing. A schematic picture of this *layer-by-layer growth* is shown in Fig. 2.2 [37, 39].

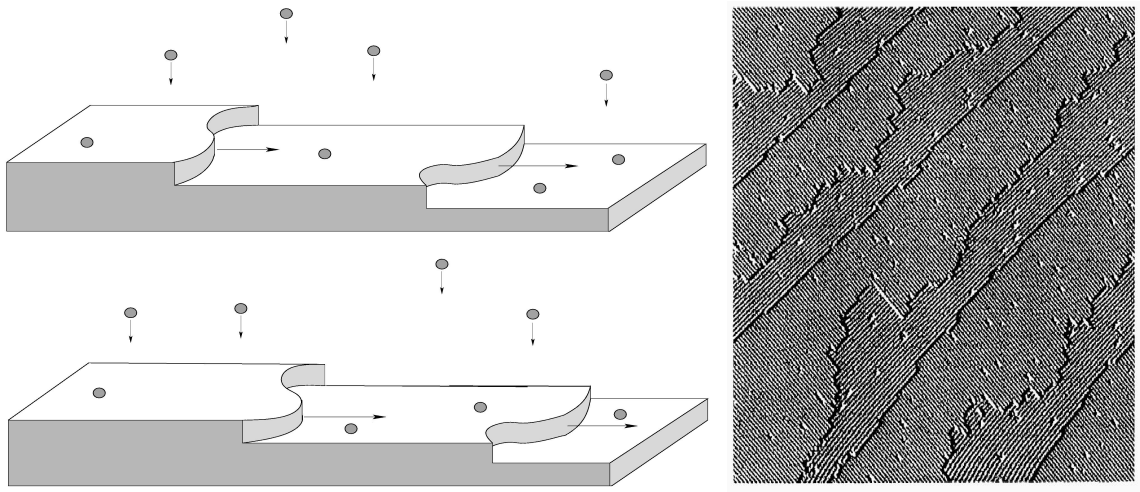

Figure 2.3: An illustration of step flow growth. To the right: a STM picture of a surface vicinal to Si(0 0 1). The Si(0 0 1) terraces are reconstructed and the direction of the reconstruction alternates from layer to layer. Taken from Ref. [88]

A picture where a surface consists only of one terrace is a highly idealized one; in reality steps are always present. Steps originate from the miscut, a crystal is never cut *exactly* along a high symmetry plane, from screw dislocations and thermal fluctuations [71]. When the average distance between the steps ℓ_{step} is much larger than the nucleation length $\ell_{step} \gg \ell_D$ they are irrelevant and the surface may be considered as a singular one. If the surface normal is not parallel to a crystal axis, but has an angle θ relative to one of the axis, there is an array of monoatomic steps at an average distance of $\ell = a(\tan(\theta)^{-1}$. Such surfaces are called *vicinal* or *stepped*. If the step distance is much smaller than the diffusion length $\ell \ll \ell_D$, the adatoms are captured by the steps and no islands nucleation takes place. Then the growth proceeds by the advancement of the steps, in so called *step-flow* mode [71], as illustrated in Fig. 2.3.

2.1 Instabilities in MBE

The picture of the MBE growth given in the previous section is of course an idealized one. In reality the surface becomes rough due to fluctuations in the deposition beam and, more important due to kinetic *instabilities*. The fluctuations in the deposition beam, which are unavoidably present, are very efficiently smoothed by diffusion of the adatoms [37, 94] and the surface remains atomistically flat over large areas [3]. In contrast, the kinetic instabilities may produce highly regular large amplitude structures on the surface [71]. In technical applications it is often desirable to produce atomically flat interfaces between composite materials. In this context instabilities seem like a unfortunate drawback. However, the lateral size of these structures lies in the nanometer scale $l \sim 10 - 1000$ nm, providing thus a possibility for fabrication of nano-size devices. Obviously such ventures require detailed understanding of the underlying instabilities.

2.1.1 Step edge barriers

The origins of the kinetic instabilities lie in the microscopic dynamics of the surface atoms which depend on the local environment in which they move. Of particular importance is the so-called *Ehrlich-Schwoebel* (ES) barrier suppressing the adatom hopping between different atomic layers [71]. In studying diffusion of adatoms on Tungsten surfaces by field ion microscopy Ehrlich and Hudda [16] noticed that migrating adatoms were reflected from the boundaries of the facets. From this observation they concluded that atoms approaching an atomic step from above are hindered from crossing the steps and thus become reflected. Naively this can be understood by the fact that crossing a step requires the adatoms to go through a poorly coordinated site (see Fig.2.4). In reality the microscopic behavior is more complicated and may involve

[3] Strictly speaking growing surfaces are always rough, the surface width diverges for large systems sizes $w \to \infty$ as $L \to \infty$ [37]. The average step distance may still be very large

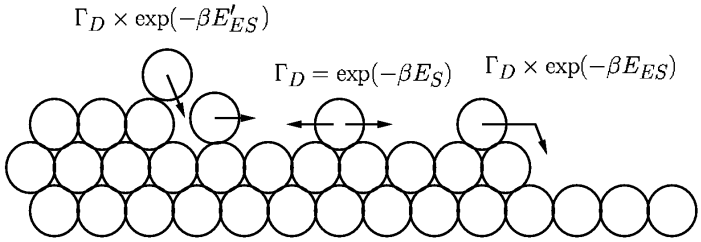

Figure 2.4: An illustration of some hopping processes on a vicinal surface. The rate of hopping depends on the activation energy ΔE. Two possibilities for interlayer transport are shown, hoping over the edge ($\Delta E = E_{ES}$) and the exchange process ($\Delta E = E'_{ES}$). Relevant mechanism is the one with lower activation energy.

consorted moves of several atoms. Often the energetically favorable mechanism is not to go over the steps but rather to move an atom sitting at the step towards the terrace and replace it with an atom lying above the step [4] [1]. Adding this knowledge to the Burton-Cabrera-Frank theory of crystal growth [10], Ehrlich and Hudda also recognized the effect this reflection form descending steps has on the growth, as the adatoms can be incorporated to the steps only from the terrace below [16].

Motivated by these experimental findings Schwoebel and Shipsey proposed shortly after a theoretical model for step motions during growth, including the asymmetry in the attachment to the step [82]. They noticed that the fluctuations in the inter step distances ℓ are either suppressed or amplified (leading to step bunching), depending on whether attachment is faster from the lower or upper terrace.

ES barriers are very difficult to observe in experiments, and the experimental determination of their strengths even more so. However, there seems to be convincing experimental [9, 45, 55] and numerical [54, 85, 87] evidence supporting the existence of ES barriers on most metal surfaces (for details see Refs. [29,71] and references therein). On semiconductor surfaces the existence or relevance of ES barriers is much more under a debate; at least the barriers seem to be weaker than on metal surfaces [46, 59, 71]. Obviously the importance of the barriers also depends on the temperature, at high temperatures the effect of ES barriers is diminished.

A one-dimensional equivalent of the ES barrier hindering mass transport between atomic layers is so called *kink-rounding barrier*, or the *kink-Ehrlich-Schwoebel barrier*, E_{kr}, which suppresses atoms diffusing along a step in going around a kink site or an island corner. The relevance of such barriers for island shapes in sub-monolayer growth

[4] This, so-called exchange mechanism, is sometimes also the preferable mechanism for terrace diffusion [1, 2]

was first discussed by Zhang and Lagally [97,98], and for the step-flow growth by Pierre-Louis *et al.* [63] and independently by Ramana Murty and Cooper [56] The existence of kink-rounding barriers is still somewhat under debate; several numerical studies support their existence [53,54] but the experimental observations are still few [11,14,35]. If present, the kink-rounding barriers have a large impact on the step-flow growth. The kink rounding barriers are discussed in detail in Sect. 4.3.1, and their influence on growth in Chapt. 5.

2.1.2 Mound formation

The stabilizing effect of the step edge barriers on the inter step distances during growth was already noticed by Schwoebel and Shipsey in 1966. The destabilizing effect on singular surfaces however remained unnoticed until some 10 years ago. In 1990 Kunkel *et al.* [44] attributed the transition from 2D layer-by-layer growth to 3D growth, on Pt(1 1 1) surfaces, to the extra energy barrier suppressing the descend of atoms landed on an island. And in 1991 Villain [94] pointed out, based on theoretical

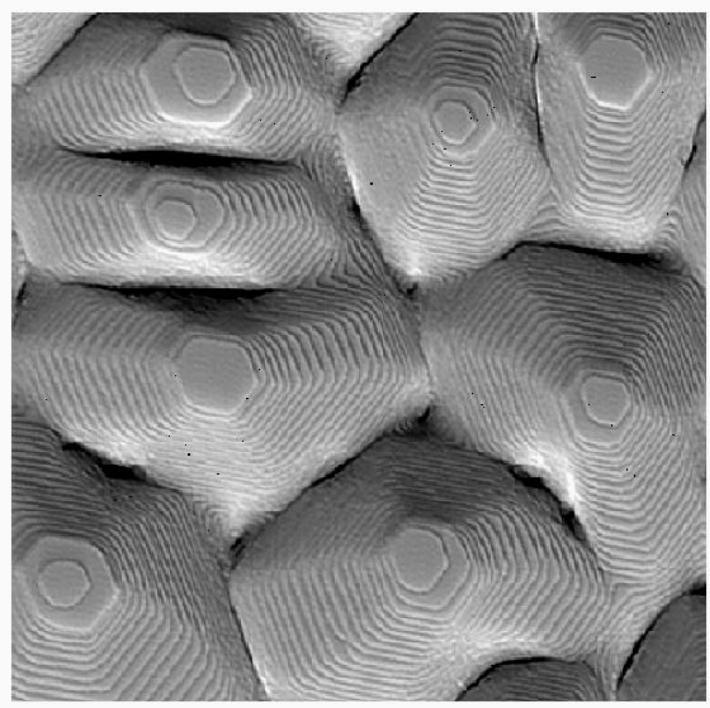

Figure 2.5: A STM topograph (230×230 nm^2) of a Pt(1 1 1) high symmetry surface, after deposition of 37.1 ML with a flux $F = 0.013$ ML/s at $T = 440$ K. Taken form Ref. [42].

considerations, that ES-barriers lead to destabilization of the layer-by-layer growth against mound formation. The mechanism causing instability is intuitively easy to understand; as the adatoms are hindered from hopping over the step edge to a lower layer, they preferably attach to an ascending step. This leads to an average adatom current on the terrace in the direction of the ascending step *i.e.* in the uphill direction. The uphill adatom current destabilizes a flat surface since small height fluctuations are amplified by the surface current. This instability, also known as "Villain instability", leads to formation of large mounds on the surface [71].

The Villain instability produces a fairly regular array of mounds on the surface, an example is shown in Fig. 2.5. The lateral distance between the islands depends on the strength of the ES-barrier. For complete barriers, which forbid interlayer mass transport totally, the mound separation is set already in the sub-monolayer regime by the island separation ℓ_D [37, 39]. For weaker barriers the initial length scale can be calculated through linear stability analysis of a flat surface (See ref. [37]). For weak ES-barriers the mound morphology evolves through *coarsening*, increasing the typical lateral length scale in the course of time [71, 73].

Since its discovery in 1991 the Villain instability has been a subject of intense theoretical and experimental research and has been observed in a number of experiments [17, 92, 99] as well as in many simulation studies [13, 84, 89]. The experimental observations of the mound morphology is one of the key indications of the existence and relevance of the ES-barriers.

2.1.3 Ripples

At first sight, the ES barrier seems to stabilize growth fluctuations on a vicinal surface; if adatoms diffusing on a terrace are reflected from a descending step, most atoms are attached to an ascending one. Thus each step advances through attachment from the terrace *in front* of it, damping the fluctuations in the inter-step spacing. However, in 1990 Bales and Zangwill noticed that the step edge barriers lead to an instability of the steps in the step direction [4]. Since steps mostly receive new material from the terrace in front of them, due to geometry, protrusions in the steps receive more adatoms per unit step length than the straight parts (See Fig. 5.1). This amplifies small perturbations on a straight step profile, leading to meandering of steps. This so-called *Bales-Zangwill instability* is one of the main topics of this thesis and will be discussed in detail in Chapter 5. The fastest growing perturbation is the one where all steps meander in phase [65, 71], which leads eventually to formation of long parallel ridges in the direction perpendicular to the steps, a good example is growth morphology of the Cu(1 1 17) surface [52] shown in Fig. 2.6.

Recently also another mechanism leading to step meandering has been proposed [56, 63]. This alternative mechanism is related dynamics of the adatoms diffusion along

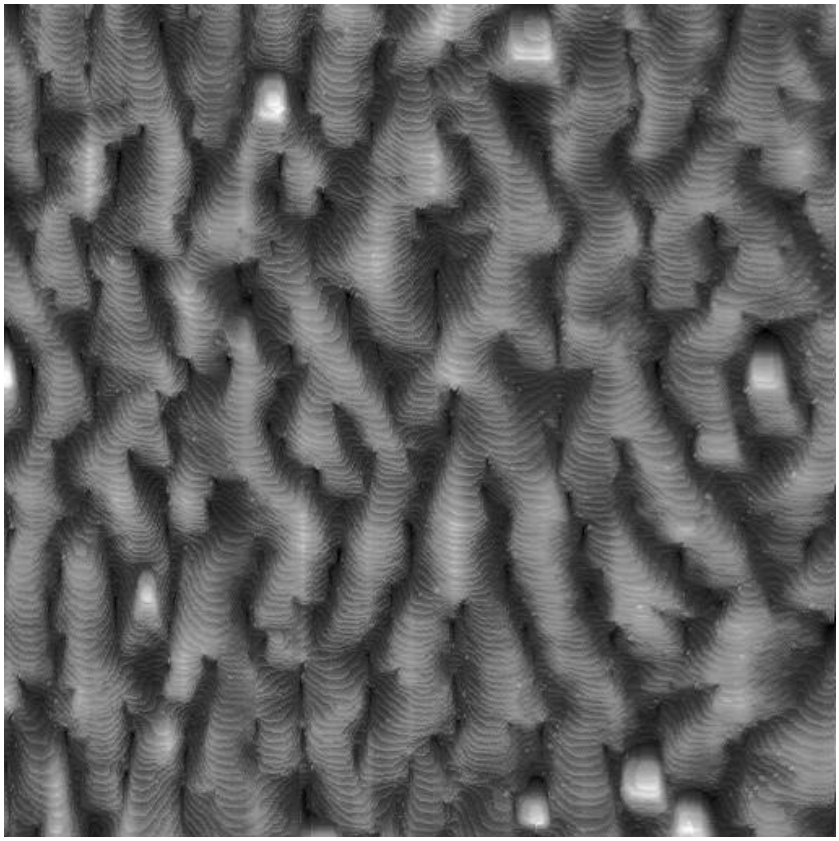

Figure 2.6: A STM topograph (230×230 nm^2) of a Cu(1 1 17) surface, vicinal to (1 0 0) high symmetry orientation (step spacing $\ell = 2.17$ nm), after deposition of 92 ML at temperature $T = 250 - 255$ K. The deposition flux was $F = 0.011$ ML/s. Courtesy of Nicolas Néel and Ludovic Douillard [58].

the steps; if step adatoms migrating along the steps are hindered from going around kink sites, a current along the step in the "up-kink" direction is created, analogous to the up-hill surface current due to the ES barrier on singular surfaces. Viewing a step as a 1D surface it is easy to see the analogy with the mounding instability [37,39]. The steps become wavy as "mounds" form on them. The mounds start growing on each step independently, creating wavy steps without any phase correlations. Eventually effective step interactions mediated through the diffusion on the terraces drive the steps in phase resulting finally in an in-phase meandering of the step train and long ripples, much like the pattern created by the Bales-Zangwill instability [34, 63].

Ripple patterns have been observed in many growth experiments on vicinal surfaces [51, 52, 59, 81] as well as in computer simulations [34, 76, 79]. Whether the ripples are due to Bales-Zangwill instability or originate from the suppression of kink-rounding

may be deduced from the wavelength dependence on parameters such as deposition flux F and temperature T. This issue will be discussed at length in Chapt. 5

2.1.4 Step bunching

An array of steps may be unstable also in the direction perpendicular to the steps. In several experiments the steps have been observed to form ***step bunches*** due to collisions of the steps. This can take place during deposition [57] or evaporation [39]. Also electromigration has been observed to cause step bunching [86]. The reason behind the bunching is again the asymmetry of the attachment/detachment dynamics at the steps, depending on whether the attachment/detachment takes place at the ascending or descending step. Step bunching will not be discussed in this thesis, an interested reader may find detailed discussion in the literature [62, 90].

Chapter 3

Theoretical models and methods

A short overview on some models commonly used to describe MBE growth will be given next. The review here is by no means exhaustive nor detailed, but rather serves as a reminder for the models relevant for the rest of this thesis. Theoretical description of the MBE method may be found in several text books [26, 49, 66] and review articles [37, 71]

During growth the dynamics takes place mostly at the surface of the crystal. The bulk dynamics, vacancy or dislocation diffusion and the like have typical time scales much longer than the motion of surface atoms and can therefore be neglected . The surface can be described in various different ways; the most obvious is to give the position of the surface over some reference plane $z = h(\mathbf{r}, t)$. The height h as well as the coordinate $\mathbf{r} = (x, y)$ in the base plane may be either discrete or, when describing the motion on a coarse grained level, continuous. A simple discrete the Solid-on-Solid (SOS) model is presented in Sect. 3.2. In SOS models the height is a single valued function of the base coordinate, excluding overhangs in the surface profile (thus the name Solid-on-Solid).

A somewhat different approach is to model the motion of the atomic steps rather than the surface itself. The steps can be viewed as 1 D surfaces. This kind of description is best suited for vicinal surfaces or submonolayer growth since it is difficult to incorporate the annihilation or creation of steps. Ideally a vicinal surface grows through propagation of a step train, keeping their number fixed. The Burton-Cabrera-Frank (BCF) model, presented in Sect. 3.3 is an example of such approach.

3.1 Central concepts

3.1.1 Surface free energy

A central quantity in any thermodynamical model is the free energy $\mathcal{F}$. The equilibrium state of a system is the one minimizing $\mathcal{F}$. Even if the free energy is an equilibrium quantity and the growth by MBE takes place far from equilibrium, it is instructive to consider first the equilibrium properties. The reason is twofold; they serve as a starting point for far from equilibrium models [37] and many properties of a system, such as surface stiffness or mobilities may be deduced from equilibrium considerations [40].

In a system with two phases and a surface dividing them the free energy reads

$$\mathcal{F} = f_A(T)\Omega_A + f_B(T)\Omega_B + \mathcal{F}_S, \tag{3.1}$$

where the $f_i(T)$'s are the free energy densities of the two phases A, B and the Ω_i's their volumes. The last term $\mathcal{F}_S$ is the free energy of the dividing surface. The surface free energy can be written as an integral over the surface area

$$\mathcal{F}_S = \int_{\partial\Omega} \mathrm{d}A\gamma(\mathbf{n}, T), \tag{3.2}$$

where $\gamma(\mathbf{n}, T)$ is the free energy per unit area and the normal vector $\mathbf{n}$ indicates the orientation of the surface. The shape of an interface separating the two phases is determined by the minimum of the surface energy. A simple example is a liquid droplet; since liquids are rotationally invariant, $\gamma(\mathbf{n}, T)$ is independent of the orientation $\mathbf{n}$ and the equilibrium shape of a droplet is simply a sphere. The surface free energy density $\gamma(\mathbf{n}, T)$ is generally dependent on the orientation, since crystals are not rotationally invariant. Knowing the form of $\gamma(\mathbf{n}, T)$ the equilibrium shape is given by the *Wulff construction*, which is the Legendre transformation of $\gamma(\mathbf{n}, T)$ [66]. The determination of the surface free energy of crystals is a complicated matter, as it depends on the microscopic interactions, surface reconstructions etc. [29].

3.1.2 Chemical potential and stiffness

In the following section the description will be limited to the 1D case to keep the notation simple; generalization to higher dimensions may be found in the literature [66]. The theory will be applied in this thesis to atomic steps, which can be considered as 1D surfaces. Choosing the coordinate system such that the average orientation of the surface is parallel to the $y = 0$ plane and denoting the surface position by $h(x)$ the surface integral (3.2) yielding free energy reads

$$\mathcal{F}_S = \int \mathrm{d}x \sqrt{1 + (h')^2}\, \gamma(\mathbf{n}, T) \equiv \int \mathrm{d}x \hat{\gamma}(h', T), \tag{3.3}$$

where $h' = \mathrm{d}h/\mathrm{d}x$ The last expression serves as a definition for the *energy per projected area* $\hat{\gamma}(h')$. Inserting a surface profile $h(x) + \delta h(x)$ leads to an expression for the first variation of the free energy

$$\delta\mathcal{F} = -\int \mathrm{d}x\, \delta h(x) \left[\frac{\mathrm{d}^2\hat{\gamma}(h')}{\mathrm{d}h'^2}\right] h''(x). \tag{3.4}$$

If the angle between the surface normal the and y-axis $\tan(\theta) = -h'$ is taken as the orientation variable rather than the slope h', the expression (3.4) can be written in a more tractable form

$$\delta\mathcal{F} = -\int \mathrm{d}x \delta h(x) \tilde{\gamma} \frac{h''(x)}{[1 + (h'(x))^2]^{3/2}} \; ; \; \tilde{\gamma} \equiv \gamma(\Theta) + \frac{\mathrm{d}^2\gamma}{\mathrm{d}\Theta^2}. \tag{3.5}$$

$\tilde{\gamma}$ is called surface *stiffness* and the term multiplying $\tilde{\gamma}$ is recognized as the surface *curvature* $\kappa(x) = \mathrm{d}\theta/\mathrm{d}s$. Thus the *chemical potential*, *i.e* the change in free energy due to addition of one atom to the surface (which means $\mathrm{d}x = a$ and $\delta h = a$) reads

$$\mu(x) = \Omega\tilde{\gamma}\kappa \; ; \; \kappa = -\frac{h''(x)}{[1 + (h'(x))^2]^{3/2}}. \tag{3.6}$$

Here $\Omega = a^2$ is the atomic area. For a two dimensional surface the stiffness is a tensor quantity, but for sufficiently isotropic surfaces the eigenvalues of the tensor $\underline{\tilde{\gamma}}$ are equal and the chemical potential may be written analogously to the 1D case as

$$\mu(x) = \Omega\tilde{\gamma}\left(\frac{1}{R_1} + \frac{1}{R_2}\right), \tag{3.7}$$

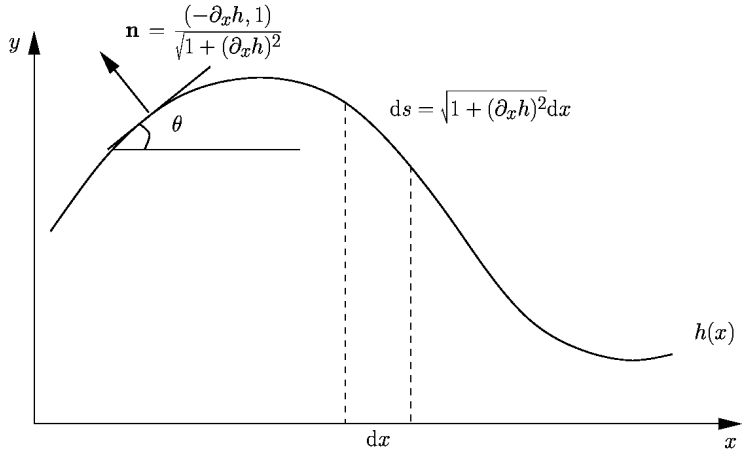

Figure 3.1: An illustration of a 1D interface geometry and the notation used in the text.

where R_1,R_2 are the principal radii of curvature of the surface and $\tilde{\gamma}$ is now the eigenvalue of the stiffness tensor [66].

3.1.3 Surfaces at equilibrium

Given the surface free energy $\hat{\gamma}(h')$, the shape of the surface is given by the Wulff construction as mentioned above [12, 66]

$$h(x,y) = \min_{h'} \left[\lambda\hat{\gamma}(h') + h'x\right], \tag{3.8}$$

where λ is a scaling factor controlling the size of the crystal. Apart from the average position also the fluctuations of the surface around its mean position are of interest. A measure for the fluctuations is given by the *surface width*, defined for a surface of linear extent L_x as

$$W^2(L_x) \equiv \frac{1}{L_x}\int_0^{L_x} \mathrm{d}x\ \langle (h(x)-\bar{h})^2\rangle\ ;\ \bar{h} = \frac{1}{L_x}\int_0^{L_x}\mathrm{d}x\ h(x), \tag{3.9}$$

The surface width can be calculated by considering small fluctuations around a flat profile $h = mx + \delta h$, where m is the average slope of the surface. Expanding the free energy (3.3) to the second order [37] gives

$$\mathcal{F}_S = \mathcal{F}_0 + \frac{1}{2}\tilde{\gamma}\int \mathrm{d}x \left(\frac{\mathrm{d}\delta h}{\mathrm{d}x}\right)^2. \tag{3.10}$$

$\mathcal{F}_0$ is the free energy of a flat surface and the first order term vanishes as the surface is in equilibrium. Inserting a Fourier decomposition $\delta h = \sum_q \hat{h}(q)\exp(-iqx)$ in Eq. (3.10) results in

$$\mathcal{F}_S = \frac{1}{2}L_x\tilde{\gamma}\sum_q |q|^2\hat{h}(q)^2 \tag{3.11}$$

and from the equipartition theorem follows immediately

$$\langle\frac{1}{2}L_x\tilde{\gamma}|q|^2\hat{h}(q)^2\rangle = \frac{1}{2\beta} \tag{3.12}$$

In terms of the Fourier components the surface width reads then

$$W^2 = \sum_{q\neq 0}|h(q)|^2 = \frac{1}{\beta L_x\tilde{\gamma}}\sum_{q\neq 0}|q|^{-2}, \tag{3.13}$$

where the summation runs over $q_n = (2\pi n)/L_x$ ($n = 1, 2, 3...$). In 1D the summation can be done exactly and the result is

$$W^2(L_x) = \frac{1}{24\beta\tilde{\gamma}}L_x \tag{3.14}$$

Thus the width diverges as the size of the system grows $L_x \to \infty$, and the surface is said to be rough. The orientation of the surface is still well defined since $\lim_{L_x\to\infty}(W/L_x) = 0$.

In higher dimensions $d \geq d_c = 2$ the surface width W remains finite even for large system sizes (at least at low temperatures) [37]. This leads to appearance of macroscopic facets the equilibrium shape with well defined orientation [66]. At some finite temperature T_R [1] there is a *roughening transition* above which the surfaces are again rough and the facets disappear [12, 66].

3.2 The Solid-on-Solid model

At low temperatures the density of vacancies, interstitials or other crystal defects is low and can be neglected altogether. The crystal surface may then be represented by an array of integer height columns. As the surface is represented at each site by a single valued function overhangs are discarded. Such models are called *Solid-on-Solid* (SOS) models. A Hamiltonian for a SOS model can be constructed by assigning an energy cost for each exposed unit surface [12, 66]

$$H = \sum_{\langle i,j\rangle} K|h_i - h_j| + H_0, \tag{3.15}$$

where h_i is the surface height at site i and the summation runs over all nearest neighbor pairs $\langle i, j\rangle$. The term H_0 is the energy of the flat surface $h_i = const$ and will be set to zero from now on. The Hamiltonian determines the energetics and thus the thermodynamics of the SOS model; knowing the Hamiltonian allows one (at least in principle) to calculate the partition function. It turns out that the SOS model has a roughening transition at a finite temperature for $d = 2$ [12], for $d = 1$ the surface is always rough and $d > 2$ always flat.

The SOS model does not have any intrinsic dynamics, so the rules for the time evolution of the system must be imposed separately. The processes to be included are migration of the surface atoms, deposition of new atoms and evaporation. The simplest way of including surface migration is to allow nearest neighbor jumps of the topmost atoms

$$(h(\mathbf{r}), h(\mathbf{r}+\mathbf{e})) \to (h(\mathbf{r}) - 1, h(\mathbf{r}+\mathbf{e}) + 1)\,, \tag{3.16}$$

where $\mathbf{e}$ is a unit vector. The hops are immediate for all height differences Δh between neighboring sites, which means that migration of atoms in the vertical direction is infinitely fast. Thus if large height differences Δh appear in the profile the dynamics are not very reasonable; in this work the surfaces are always quite flat and the dynamics

[1] The transition temperature may lie above the melting temperature

presented here are sufficient. The deposition and evaporation moves are obvious

$$h(\mathbf{r}) \to h(\mathbf{r}) \pm 1. \tag{3.17}$$

One still needs to specify the rates for each process. The deposition flux F is an experimentally controllable variable and can be set to a desired value. As the diffusion of adatoms is a thermally activated process it is common to choose the hopping rates as

$$\Gamma = \Gamma_0 \exp(-\beta \Delta E), \tag{3.18}$$

where the activation barrier ΔE depends on the local environment, $\beta = 1/k_B T$ is the inverse temperature and the diffusion pre-factor Γ_0 is a constant setting the physical time scale. For surface diffusion it is of the order of atomic vibration frequency $\nu \sim 10^{12} s^{-1}$ and will be assumed to be the same for all processes. Similarly the evaporation rate is $\Gamma_{EV} = \Gamma_0 \exp(-\beta \Delta E_{EV})$, where ΔE_{EV} is the energy barrier for evaporation.

To ensure that the model obeys the Boltzmann distribution at equilibrium it is common to require that the rates (3.18) fulfill the *detailed balance* condition [47, 93]

$$\frac{\Gamma_{i \to j}}{\Gamma_{j \to i}} = \exp\left(-\beta \Delta H\right). \tag{3.19}$$

The ratio of the transition rates from configuration $i \to j$ and its inverse process $j \to i$ depends on the energy difference between the configurations $\Delta H = H_i - H_j$. It is easy to see that for such rates the stationary state has indeed the Boltzmann distribution $P(i) \sim \exp\left(-\beta E(i)\right)$. It should be noted however that this is not the only way to choose rates that lead to the Boltzmann distribution in the stationary state. The detailed balance requirement doesn't specify the rates completely, but it leaves room for variation and the most practical choice of rates depends on the system. A commonly employed choice are the Arrhenius rates [40, 48]

$$\Delta E = n E_n, \tag{3.20}$$

where n is the number of nearest neighbors of the hopping atom in the initial state. It is easy to see that detailed balance is fulfilled if $E_n = 2K$. The main advantage of the Arrhenius rates $\Gamma_{i \to j}$ is that the rates do not depend on the final configuration j, making them analytically easier to handle. Another popular choice of rates are the *Metropolis* rates [40, 47]

$$\Gamma_{i,j} = \Gamma_0 \min\left[1, \exp(-\beta \Delta H)\right], \tag{3.21}$$

where the transition to a lower energy state is always accepted. This is in particular useful in Monte-Carlo simulations as it increases the computational efficiency [47].

In this work a combination of Arrhenius and Metropolis rates is used. The activation energy in Eq. (3.18) for a hop is [13, 36]

$$\Delta E = E_S + n_i E_n + (n_i - n_f)\Theta(n_i - n_f) E_{BB} + (m_i - m_f)\Theta(m_i - m_f) E_{ES}. \tag{3.22}$$

where E_S is the energy barrier for diffusion on a flat terrace, E_n is the contribution of a nearest neighbor bond to the hopping barrier and E_{BB} is an additional energy cost for bond breaking; n_i denotes the number of in-plane nearest neighbors before the hop and n_f after the hop and $\Theta(x)$ is the Heaviside step function, $\Theta(x) = 1$ if $x > 0$ and 0 otherwise. The last term implements an Ehrlich-Schwoebel barrier E_{ES} to the model: m_i, m_f are the number of next-nearest neighbors in the planes beneath and above before (m_i) and after (m_f) the hop. This term suppresses hops to an edge site *above* a step. Such rates can be written as a product of an Arrhenius and a Metropolis part

$$\Gamma_{i,j} = \Gamma_S \times \underbrace{\exp\left(-\beta n_i E_n\right)}_{\Gamma^{(1)}} \times \underbrace{min[1, \exp(-\beta \Delta H^{(2)})]}_{\Gamma^{(2)}}. \tag{3.23}$$

$\Gamma_S \equiv \Gamma_0 \exp\left(-\beta E_S\right)$ is the diffusion rate on a flat terrace, including also the diffusion barrier E_S. The second contribution is the common Arrhenius rate (n_i is the number of nearest neighbors at the *initial* site). The last term consists of the bond-breaking and Ehrlich-Schwoebel contribution to the rates, it differs from 1 only if the hop leads to a higher energy state. These rates fulfill the detailed balance condition with respect

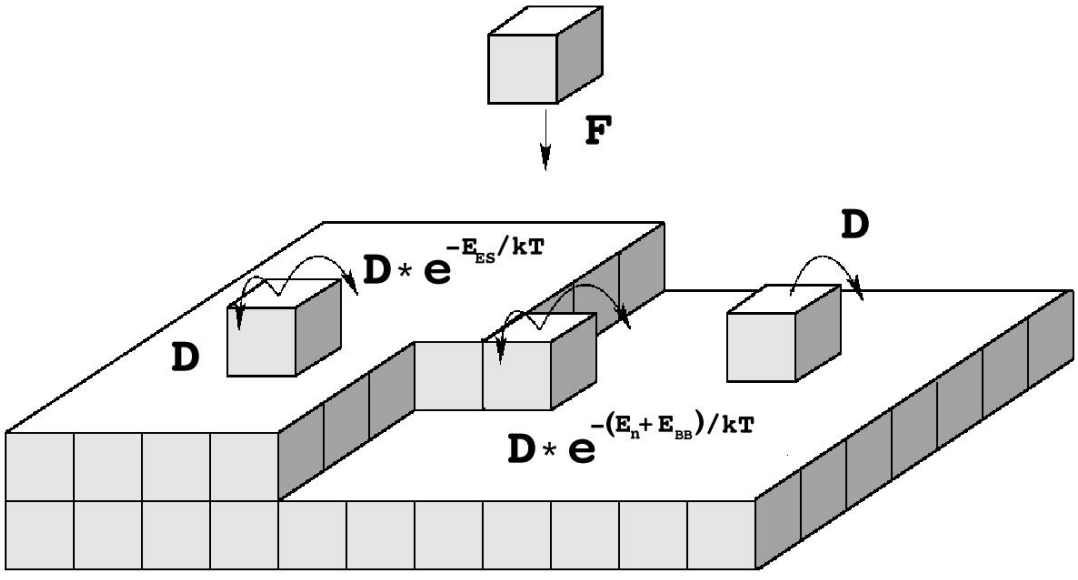

Figure 3.2: An illustration of the SOS model. Rates of various processes according to energetics in Eq. (3.22) are marked.

to a Hamiltonian [34]

$$\begin{aligned} H &= H^{(1)} + H^{(2)} \\ H^{(1)} &= \sum_{\langle \mathbf{r},\mathbf{r}' \rangle} \frac{1}{2} E_n |h_{\mathbf{r}} - h_{\mathbf{r}'}| \\ H^{(2)} &= \sum_{\langle \mathbf{r},\mathbf{r}' \rangle} \frac{1}{2} E_{BB} |h_{\mathbf{r}} - h_{\mathbf{r}'}| + E_{ES}(|h_{\mathbf{r}} - h_{\mathbf{r}'}| - 1)\Theta(|h_{\mathbf{r}} - h_{\mathbf{r}'}| - 1), \end{aligned} \tag{3.24}$$

as the part $\Gamma^{(1)}$ fulfills the condition with respect to $H^{(1)}$ and $\Gamma^{(2)}$ with respect to $H^{(2)}$. In (3.24) the energy is proportional to the exposed vertical area, each exposed unit area increases the energy by amount

$$E_k = \frac{1}{2}(E_n + E_{BB}). \tag{3.25}$$

A step of length L_s on the surface increases the energy by $L_s \times E_k$ and adding a kink into the step by E_k, therefore E_k is commonly called the *kink-energy*. The ES part of the Hamiltonian adds an extra penalty for height differences ≥ 2, thus suppressing the configurations where an atom is at a site directly above a step.

In the model defined as above, the atoms cannot leave the surface. Neglecting the desorption is justified in many cases, as the MBE conditions are commonly chosen to maximize the growth speed by minimizing the desorption [37, 71]. It is also clear that the model has a kink-rounding barrier, hindering the atoms diffusing to round corners as they diffuse along the steps (See sect. 2.1.1) [34]. Since only nearest neighbor hops are allowed, the atoms must first detach completely from the step to go around a corner site, implying a kink rounding barrier $E_{kr} = E_{BB}$.

3.3 The BCF theory

Another approach to model a surface is to consider the atomic steps as fundamental objects, rather than individual atoms [29]. Atoms move very quickly in comparison to the time scale of the growth. A remarkably successful theory of this type was presented by Burton, Cabrera and Frank in 1951 [10], named after them as the BCF theory. Instead of tracking each adatom on the surface, in the BCF description the adatom dynamics are governed by the diffusion equation on flat terraces. The atomic steps separating the terraces serve as sinks and sources for the diffusion field and appear in the model through the boundary conditions as illustrated in Fig. 3.3. The step positions are continuous functions of the coordinates, and the discreteness of the crystal is preserved only in the vertical direction; the height of the surface changes discontinuously at the steps. The BCF theory is best suited for describing the evolution of a vicinal surface, where steps are neither created nor annihilated. Since the steps

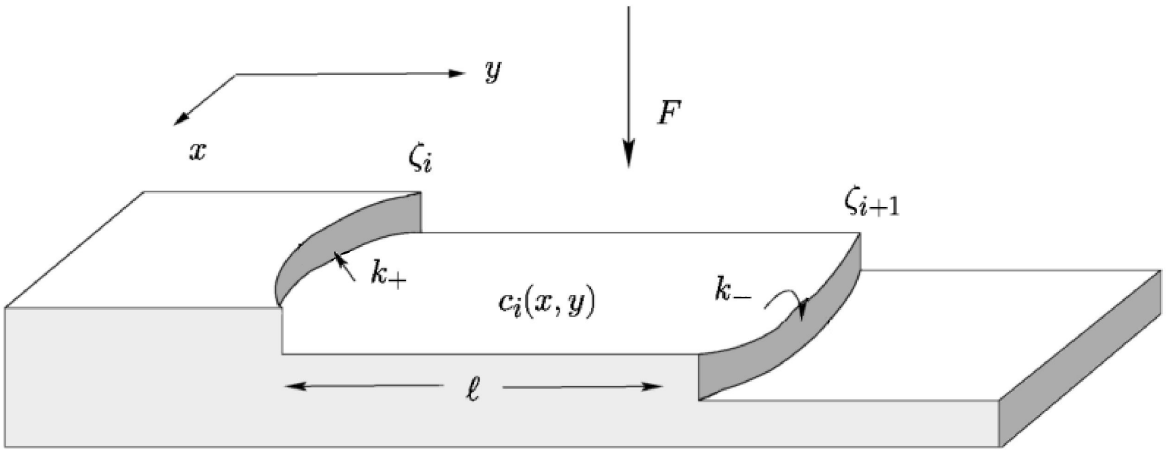

Figure 3.3: A cartoon illustrating the BCF model and the notation used in the text.

specify the boundary conditions of the diffusion field it is clear that adding/removing them leads to difficulties. From here onwards it is implicitly assumed that no islands are nucleated on the terraces, and all adatoms are captured by the existing steps.

The adatom concentration on i^{th} terrace $c_i(\mathbf{x}, t)$ follows the diffusion equation

$$\frac{\partial c_i(\mathbf{x},t)}{\partial t} = D\nabla^2 c_i(\mathbf{x},t) + F - \frac{c_i(\mathbf{x},t)}{\tau}, \tag{3.26}$$

where D is the diffusion coefficient, F the intensity of the deposition beam and τ the characteristic time an atom stays on the terrace before evaporating. Few simplifications will be made at once: as well as in the SOS model introduced in the previous section, the desorption will be neglected $\tau \to \infty$, with the same justification as in the SOS case. Further simplification is made by neglecting the time derivative of the diffusion field. This assumption is justified if the motion of the adatoms is much faster than the motion of the steps; for an adatom it takes $t_{atom} = \ell^2/D$ to diffuse over the terrace of width, this is to be compared with the time it takes for a step to move the same distance $t_{step} = v_{step}/\ell$. The upper bound for the step velocity v_{step} is obtained by assuming that all atoms arriving to the surface attach to the steps, implying that the step velocity $v_{step} \leq \Omega F \ell$. The ratio of these time scales defines the *Péclet-number*

$$\mathrm{Pe} \equiv \frac{t_{atom}}{t_{step}} \leq \frac{\Omega F \ell^2}{D}, \tag{3.27}$$

where the equal sign applies when no mass leaves the surface $\tau \to \infty$. When $\mathrm{Pe} \ll 1$ the concentration field is essentially always in a stationary state with respect to given step configuration. This does not mean that the concentration is static, the steps move

and the concentration field is adjusted to their motion. In this work the case of no desorption is considered implying $\mathrm{Pe} = \Omega F \ell^2 / D$. In step flow growth the nucleation of islands on terraces may be neglected, implying that the nucleation length ℓ_D is much larger than the terrace width $\ell_D = (D/F)^{1/6} \gg \ell$. Here dimers have been assumed to be stable $i^\star = 1$ (See Sect. 2.0.1). Thus the Péclet-number is always small in the step-flow growth $\ell \ll (D/F)^{1/6} \ll (D/F)^{1/2} \Rightarrow \mathrm{Pe} \ll 1$.

Thus we are left with an equation

$$D\nabla^2 c_i(\mathbf{x}, t) + F = 0. \tag{3.28}$$

The boundary conditions for the concentration field are determined by the dynamics at the steps $i, i+1$. The particle exchange with the steps is related to the deviation of $c_i(\mathbf{x}, t)$ from its equilibrium value [18, 28]

$$\begin{aligned} D\nabla \cdot c_i(x, \zeta_i, t) &= k_+ \left[c_i(x, \zeta_i, t) - c_{eq}\right] && (3.29) \\ -D\nabla \cdot c_i(x, \zeta_{i+1}, t) &= k_- \left[c_i(x, \zeta_{i+1}, t) - c_{eq}\right], && (3.30) \end{aligned}$$

where $\zeta_i(x)$ is the position of i^{th} step in y direction. The kinetic coefficients $k_\pm$, describing the rate at which adatoms can attach/detach to/from the steps, differ for mass exchange with an ascending $(+)$ and descending $(-)$ step (See Fig. (3.3)). The equilibrium concentration near the steps can be determined by considering the chemical potential of adatoms on the terrace and at the step [28]; steps can be viewed as a 1D interface in equilibrium with the 2 D adatom gas on the terrace. In the previous section the chemical potential of a surface was found to be proportional to the curvature (See Eq. (3.6))

$$\mu_{step} = \Omega\tilde{\gamma}\kappa_i(x) = -\Omega\tilde{\gamma}\frac{\partial_{xx}\zeta_i}{\left[1 + (\partial_x \zeta_i)^2\right]^{3/2}}. \tag{3.31}$$

If the adatom concentration at a straight step ($\mu_{step} = 0$) is c^0_{eq}, the concentration at a curved step is $c_{eq} = c^0_{eq} \exp(\beta\mu_{step})$ [28]. Expanding this to first order leads to an expression for the equilibrium concentration

$$c_{eq} = c^0_{eq}\left(1 + \Omega\beta\tilde{\gamma}\kappa_i(x)\right). \tag{3.32}$$

In front of a positively curved step ($\kappa_i > 0$) the adatom concentration is increased. The enhancement follows from the fact that on a positively curved step the atoms have on the average fewer nearest neighbors along the step and are thus more loosely bound than on a negatively curved step [5].

The description is completed by the equation of motion for the steps; each step moves due to mass exchange with adjacent terraces. The requirement of mass conservation at the steps yields an expression for the normal velocity of i^{th} step

$$v^n_i(x) = \Omega D\left[\mathbf{n}_i \cdot \nabla c_i(x, \zeta_i) - \mathbf{n}_{i-1} \cdot \nabla c_{i-1}(x, \zeta_i)\right], \tag{3.33}$$

where **n** is the unit normal vector of the step and Ω denotes the atomic area. The two terms in the parentheses on the R.H.S. are the mass currents to the step from the adjacent terraces.

3.3.1 Connection with SOS

It is useful to make a connection between the BCF model and the discrete SOS model. The parameters of the BCF equations can be expressed in terms of the energies and transition rates of the SOS model. The diffusion constant of the adatoms is the hopping rate of an atom with no lateral neighbors $D = a^2\Gamma_0 \exp(-\beta E_S)$ and the deposition flux F as well as the evaporation time τ are obviously equal in both models.

The kinetic attachment coefficients $k_\pm$ are the transition rates to a step site, *i.e.* a hop from a site with no lateral bonds to a site with lateral bonds. Usually the hop rate from the terrace below is equal to the diffusion rate D/a^2 and from above it contains the possible Ehrlich-Schwoebel barrier $k_- = D\exp(-\beta E_{ES})$. In the model with rates defined by Eqs. (3.18),(3.22), the ES-barrier suppresses hops to a site *above* an edge site instead to the edge site itself by energy E_{ES}.

In order to calculate the equilibrium concentration of adatoms on the terrace c^0_{eq} and the step stiffness $\tilde{\gamma}$ the analogy between a step and a 1D surface can be employed again. As long as the temperature is low enough so that no overhangs are formed to the steps the approximation is valid. One can then directly use the known result for the SOS surface stiffness [29, 40]

$$\tilde{\gamma} = \frac{2}{a\beta}\sinh^2\left(\frac{\beta E_k}{2}\right), \tag{3.34}$$

where E_k is the kink-energy (3.25). The adatom concentration c^0_{eq} can be obtained by considering a straight step in equilibrium with the adatom gas on the terrace. Atoms detach from the step to the terrace at rate [2] $\Gamma_{ev} = \langle\, (D/a^2)\exp[-\beta(2E_k + 2nE_k)]\,\rangle$, where the brackets denote a thermal average taken over the number of nearest neighbors of a step atom ***along*** the step $n = 0, 1, 2$. The thermal average can be calculated exactly for 1D SOS interface [40]

$$\langle \exp(-\beta 2nE_k)\rangle = \exp(-2\beta E_k). \tag{3.35}$$

Thus a macroscopically straight step evaporates to the terrace, per unit length a, with rate $\Gamma_{ev} = (D/a^2)\exp(-4\beta E_k)$. In equilibrium this must be counter balanced by the attachment rate of the atoms from the terrace to the step Dc^0_{eq}. Setting the two terms equal yields

$$c^0_{eq} = \Omega^{-1}\exp(-4\beta E_k) \tag{3.36}$$

[2] To hop from an edge site to the terrace $1 + n$ bonds must be broken, *i.e.* $2 + 2n$ new kinks are created

in agreement with the energetic argument $c_{eq}^0 = \Omega^{-1}\exp(-\beta\Delta E)$, where ΔE is the formation energy of a terrace atom from a kink site [18].

3.4 Monte-Carlo method

Monte-Carlo (MC) simulations are a commonly used tool in many areas of physics. The idea is to create a series of states of a system *randomly*, rather than following the actual time evolution, thus effectively sampling the phase space of the system [47]. The sequence of configurations $\mathcal{C}$ must be constructed in a way such that each configuration is accounted with a correct statistical weight $P(\mathcal{C})$. The sequence is created in practice by defining the transition probabilities between configurations $W(\mathcal{C} \to \mathcal{C}')$ and updating the configuration accordingly. The stationary distribution then obeys the equation

$$\sum_{\mathcal{C}'} [P_{st}(\mathcal{C})W(\mathcal{C} \to \mathcal{C}') - P_{st}(\mathcal{C}')W(\mathcal{C}' \to \mathcal{C})] = 0. \tag{3.37}$$

It is easy to see that the Boltzmann distribution $P_{st}(\mathcal{C}) = Z^{-1}\exp(-\beta H(\mathcal{C}))$ can be created by choosing $W(\mathcal{C} \to \mathcal{C}')$ that obey the detailed balance condition (3.19) introduced in the previous section, so that in Eq. (3.37) each term in the sum vanishes separately (this is however not the only way to solve (3.37)). A popular choice is the Metropolis sampling [47] $W(\mathcal{C} \to \mathcal{C}') = \min[1, \exp(-\beta\Delta H)]$, which makes the sampling computationally efficient, since the acceptance probability of a transition is as high as possible. Thermodynamical averages can then be calculated by taking an average over configurations created according to these rates. When calculating stationary averages, the evolution of the system does not have to represent any physical evolution; it suffices that the configurations are sampled with appropriate statistical weight [47].

In kinetic Monte Carlo (KMC) the interest is in the time evolution of a system and the rates must have a physical relevance [48]. Examples of such situations are studies of relaxation dynamics or evolution of driven systems. The simplest recipe for KMC simulation is as follows:

1. choose randomly a transition i and calculate the relative probability of the transition $P_i = \Gamma_i/\Gamma_{max}$, where Γ_{max} is the rate of the fastest process in the system.
2. Generate a random number ψ between $[0, 1]$ and compare with P, if $\psi \leq P$ update the configuration according to transition i and increase time by $(N\Gamma_{max})^{-1}$, where N is the number of possible processes, if $\psi > P$ increase time by $(N\Gamma_{max})^{-1}$ without update.
3. Start from the beginning.

This method is computationally very inefficient if the rates are very different as most of the trials lead to a rejection of the transition. This is the case for example in

low temperature simulations. An improvement has been presented by Bortz, Kalos and Lebowitz [8] and the method is named BKL algorithm after its inventors. In the BKL method the waste of computational time due to rejected transition trials is eliminated by always accepting the chosen move. The transitions then have to be chosen with a correct probability. The probability of transition i is $P_i = \Gamma_i / \Gamma_{TOT}$ where

$$\Gamma_{TOT}(\mathcal{C}) = \sum_n \Gamma_n \tag{3.38}$$

is the *total* activity rate of the system at state $\mathcal{C}$ and the summation runs over all transitions possible in state $\mathcal{C}$. The transition to be realized can then be chosen by generating a random number r in the interval $[0, \Gamma_{TOT}]$ and finding the first process i for which

$$\sum_{n=0}^{i} \Gamma_n \geq r \tag{3.39}$$

Choosing the process simply by applying (3.39) takes $\sim N$ operations, where N is the number of possible transitions. In practice the choice of the process can be done more efficiently by creating a binary tree where each node contains the sum of the rates

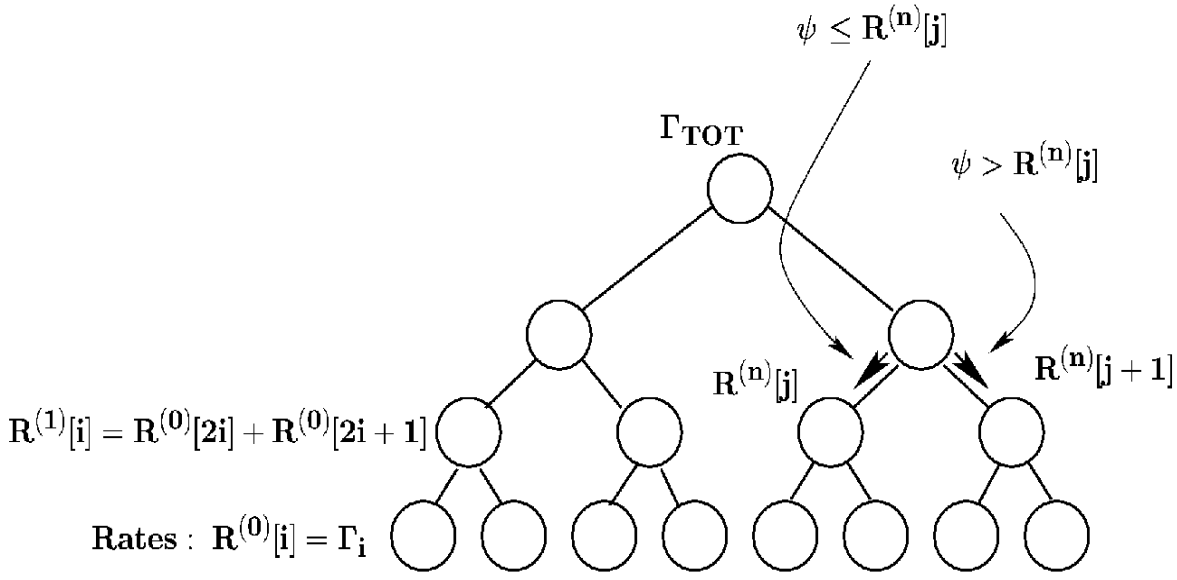

Figure 3.4: A binary tree including the transition rates at the lowest level an the cumulative rate at higher levels. The arrows indicate the direction of descend when choosing the event to be executed. The highest node contains the total activity rate of the system Γ_{TOT} (3.38).

below the node as illustrated in Fig. 3.4. If the rates are stored in an array $R^{(0)}[i]$ the next level in the tree contains $R^{(1)}[i] = R^{(0)}[2i] + R^{(0)}[2i+1]$ and quite generally

$$R^{(n)}[i] = R^{(n-1)}[2i] + R^{(n-1)}[2i+1]. \tag{3.40}$$

The size of the array $R^{(0)}[i]$ must be [3] 2^k and the top element of the tree contains $R^{(k)}[0] = \Gamma_{TOT}$. The transition can then be chosen by following the tree from the top down. This may be done in the following fashion [77]:

1. Generate a random number ψ in the interval $[0, \Gamma_{TOT}]$ and start from the top $n = k$, $i = 0$. Here k is the height of the tree, the lowest level has size 2^k.

2. Compare the number ψ with the cumulative rate in the left branch $R^{(n-1)}[2i]$

3.a If $\psi \leq R^{(n-1)}[2i]$, descend to the left branch $n \to n-1$, $i \to 2i$ and continue from 2.

3.b If $\psi > R^{(n-1)}[2i]$, update the random number $\psi \to \psi - R^{(n-1)}[2i]$ and descend to the right branch $n \to n-1$, $i \to 2i+1$. Continue from 2.

The process is illustrated in Fig. 3.4. This way the transition to be executed is always chosen with the right probability, with $\sim \log(N)$ operations. The size of the part of the tree that needs to be updated after every transition is independent of the system size since the transition rates depend only on the local environment and the transitions change the system only locally.

After each configuration update the simulation time is incremented by τ. If all processes are instantaneous (as assumed here), only one process occurs at the time and the average waiting time is $\langle\tau\rangle = \Gamma_{TOT}^{-1}$, having an exponential distribution. Thus the time increment should be chosen randomly from the distribution [48]

$$P(\tau) = \frac{1}{\langle\tau\rangle} \exp(-\tau/\langle\tau\rangle). \tag{3.41}$$

If the short time correlations are not of any interest the time may as well always be incremented by the average value $\langle\tau\rangle$.

[3] The size of the system does not have to be 2^k as the lowest level of the tree $R^{(0)}[i]$ may contain zeros.

Chapter 4

Thermodynamic fluctuations and relaxation kinetics

4.1 Relaxation kinetics

The easiest place to start studies of non-equilibrium dynamics is the relaxation kinetics. This means description of a system close to an equilibrium state and approaching it. Again the treatment is restricted to the 1D case, with the same justification as in the previous chapter. A common ansatz for the relaxation rate of a variable is to assume that it is linearly proportional to the deviation from its equilibrium value [37]

$$\frac{\partial h}{\partial t} = -\sigma_{int}\frac{\delta \mathcal{F}[h(x)]}{\delta h(x)} \tag{4.1}$$

where the constant of proportionality, σ_{int}, is called *interface mobility*. Inserting the expression for the free energy from the previous chapter (3.5), and noting that to the first order the curvature $\kappa \approx h''$, the equation reads to the leading order

$$\frac{\partial h(x,t)}{\partial t} = \sigma_{int}\tilde{\gamma}\frac{\partial^2 h(x,t)}{\partial x^2}. \tag{4.2}$$

This linear equation is valid for gently deformed surfaces $|h'| \ll 1$.

Equation (4.2) corresponds to the case where the surface can exchange mass with the gas phase, this case is commonly referred as evaporation-condensation (EC) dynamics. In the opposite case, where the mass is conserved, the surface morphology evolves through a surface current J, and the dynamics are referred to as surface diffusion (SD) dynamics. The current J is proportional to the variation of the chemical potential along the arc-length $J = -\sigma\partial_s\mu$ and the normal velocity of the surface v_n is the divergence of this current [37]

$$v_n = -\Omega\partial_s\sigma\partial_s\mu, \tag{4.3}$$

where σ is the *mobility of the atoms along the surface* [1] and Ω the atomic area. After insertion of the chemical potential (3.6), the equation of motion reads

$$\frac{\partial h(x,t)}{\partial t} = -\sigma\Omega^2\tilde{\gamma}\frac{\partial^4 h(x,t)}{\partial x^4}, \tag{4.4}$$

where the condition $|h'| \ll 1$ has again been implied.

The equation of motion acquires the form

$$\frac{\partial h(x,t)}{\partial t} = -\alpha_n \left(-\frac{\partial^2}{\partial x^2}\right)^n h(x,t) \tag{4.5}$$

to leading order in both cases. Here $n = 1$ corresponds to the EC-kinetics with $\alpha_1 \equiv \sigma_{int}\tilde{\gamma}$, and $n = 2$ refers to the SD-kinetics with $\alpha_2 \equiv \sigma\Omega^2\tilde{\gamma}$. The decay of large length scale perturbations can be examined by inserting a Fourier decomposition of the surface profile

$$h(x,t) = \sum_q \hat{h}(q,t)\exp(-iqx). \tag{4.6}$$

Since in linear equations the modes do not couple, each mode can be treated separately. Insertion into Eq. (4.5) leads to solution for each Fourier mode

$$\hat{h}(q,t) = \hat{h}(q,0)\exp(-t/\tau_n(q)), \tag{4.7}$$

where the decay time of the q^{th} mode reads

$$\tau_n(q) \equiv \frac{1}{\alpha_n|q|^{2n}}. \tag{4.8}$$

From this equation one sees that the long wavelength modes decay slowly, as might be expected, and the mass conserving dynamics are very inefficient at large length scales ($\tau_2(q) \sim q^{-4}$) when mass must be transported over long distances. It may be concluded that if mass exchange with the gas phase is possible, even at very low rate, it dominates the dynamics at long enough scales

$$\lim_{q\to 0}[\tau_1(q)] = \infty \ , \ \lim_{q\to 0}[\tau_2(q)] = \infty \ , \ \lim_{q\to 0}\left[\frac{\tau_2(q)}{\tau_1(q)}\right] = 0. \tag{4.9}$$

The even power of q^{2n} appearing in the relaxation rate is a sign of *local* relaxation dynamics [37]. Odd powers would appear in the non-local case; term $\sim |q|\hat{h}(\mathbf{q},t)$ appears in equation for diffusion limited erosion [41], and $\sim |q|^3\hat{h}(\mathbf{q},t)$ would arise from relaxation through volume diffusion [37]. By measuring the relaxation rate of long wavelength perturbations, the type of relaxation dynamics can be deduced. Furthermore, it opens a possibility for measurement of the microscopic parameters $\sigma, \gamma...$ from the relaxation rates. This fact will be used in the forthcoming section in studying the step fluctuations.

[1] Sometimes the mobility is defined through $J = \tilde{\sigma}\partial_s c$, where c is the adatom concentration and $[\tilde{\sigma}] = m^2 s^{-1}$. In this work $[\sigma] = mJ^{-1}s^{-1}$

4.2 Thermal fluctuations

Real surfaces always have thermal fluctuations. They can be included in the linear description quite easily, by adding a stochastic term in the relaxation equation. The Langevin equation, describing the surface evolution with the thermal fluctuations reads [37]

$$\frac{\partial h(x,t)}{\partial t} = -\alpha_n \left(-\frac{\partial^2}{\partial x^2}\right)^n h(x,t) + \xi(x,t), \tag{4.10}$$

where the stochastic term $\xi(x,t)$ describing thermal fluctuations is *Gaussian white noise* [93]. The Gaussian noise has zero mean $\langle \xi(x,t) \rangle = 0$ and for EC-dynamics a covariance

$$\langle \xi(x,t)\xi(x',t') \rangle = \mathcal{A}_1 \delta(t-t')\delta(x-x'). \tag{4.11}$$

In the case of SD-dynamics also the fluctuations have to obey mass conservation and can thus be written as a divergence of a fluctuating current $\xi(x,t) \sim -\partial_x j_s(x,t)$. Consequently the covariance of the stochastic process ξ reads

$$\langle \xi(x,t)\xi(x',t) \rangle = -\mathcal{A}_2 \partial_x^2 \delta(t-t')\delta(x-x'). \tag{4.12}$$

The noise term leads to roughening of the surface, and the amplitude $\mathcal{A}_n$ is fixed by the requirement that the roughness is equal to the thermal roughness (3.14), derived from the partition function in the previous chapter.

Inserting a Fourier decomposition (4.6) of $h(x,t)$ and $\xi(x,t)$ into Eq. (4.10) leads to an equation for each mode

$$\frac{\partial \hat{h}(q,t)}{\partial t} = -\frac{1}{\tau(q)}\hat{h}(q,t) + \hat{\xi}(q,t). \tag{4.13}$$

As $\hat{\xi}$ is a linear transformation of a Gaussian stochastic process, it is also Gaussian having zero mean $\langle \hat{\xi}(q,t) \rangle = 0$ and covariance

$$\langle \hat{\xi}(q,t)\hat{\xi}(q',t') \rangle = \frac{\mathcal{A}_n}{L_x} q^{2(n-1)} \delta(t-t')\delta(q+q'). \tag{4.14}$$

Here L_x is again the linear size of the surface. It was seen in the previous section that the mass conserving term in the relaxation equation is irrelevant in comparison to the non-conserving. This applies also to the fluctuation terms; at large length scales (small q) the amplitude of the conserved noise goes to zero.

$$\lim_{q \to 0} \left[\frac{\mathcal{A}_2 q^2}{\mathcal{A}_1} \right] = 0 \tag{4.15}$$

The equation of motion for each Fourier mode is that of a randomly driven harmonic oscillator and the general solution reads [37]

$$\hat{h}(q,t) = e^{-t/\tau_n(q)}\hat{h}(q,0) + \int_0^t \mathrm{d}t' \exp\left[-(t-t')/\tau_n(q)\right]\hat{\xi}(q,t'). \tag{4.16}$$

Multiplying with $\hat{h}(q',t')$ and averaging over the noise according to Eq. (4.14) leads to

$$\begin{aligned} \langle\hat{h}(q,t)\hat{h}(q',t)\rangle &= e^{-(t+t')/\tau_n}\hat{h}(q,0)\hat{h}(q',0) && (4.17)\\ &+ \frac{\mathcal{A}_n\tau_n(q)}{2L_x}q^{2n-2}\left(e^{-|t-t'|/\tau_n} - e^{-(t+t')/\tau_n}\right)\delta(q+q'), && (4.18)\end{aligned}$$

where $n = 1$ applies again for EC-dynamics and $n = 2$ for SD-dynamics. In the stationary state $t, t' \to \infty$ the dependence on the initial condition vanishes and the expression reduces to

$$\langle\hat{h}(q,t)\hat{h}(q',t)\rangle = \frac{\mathcal{A}_n\tau_n(q)}{2L_x}q^{2n-2}e^{-|t-t'|/\tau_n}\delta(q+q'). \tag{4.19}$$

The Langevin equations should yield the same result as the thermodynamical treatment in Chapter 3. Requiring consistency between the theories fixes the amplitude of the fluctuations $\mathcal{A}_n$. Comparing (4.19) with the result (3.12) in Chapter 3, following from the equipartition theorem, yields

$$\mathcal{A}_n = \frac{2}{\tilde{\beta}\gamma\tau_n(q)q^{2n}} \tag{4.20}$$

Application of the results (4.17) and (4.20) allow the determination of the general two-point correlation function

$$g(\mathbf{x},\mathbf{x}',t,t') \equiv \langle[h(\mathbf{x},t) - h(\mathbf{x}',t')]^2\rangle, \tag{4.21}$$

which will be applied in the following section to the time dependent step fluctuations.

4.3 Step fluctuations

Of special importance for this work are the fluctuations and relaxation kinetics of steps of mono atomic height. Such a step can be considered as a 1-D interface, in contact with the adatom gas on the terraces. The steps differ from the 1-D surface case in the perspective that often many steps are present on a surface, and their interactions with each other must be taken into account [29].

The simplest approximation is to assume only a hard core repulsion between the steps, *i.e.* the steps cannot cross each other due to very high energy cost for creating

an overhang. With this assumption a step may be treated approximately as a freely fluctuating object bounded between hard walls, separated by 2ℓ , where ℓ is the mean terrace width [29]. Using the result of the previous section the spatial two point correlation function (4.21) of a 1D surface can be calculated, yielding for a step of length L_x with periodic boundary conditions in the stationary state $t \to \infty$

$$G(x) \equiv g(x,0,t,t) = \frac{2}{L_x \beta\tilde{\gamma}} \sum_{q\neq 0} \frac{1-\cos(qx)}{q^2} = \frac{1}{\beta\tilde{\gamma}}|x|\left(1-\frac{|x|}{L_x}\right). \tag{4.22}$$

This result is directly applicable to a single isolated step. By setting $\sqrt{G(L_C)} \sim 2\ell$, it is seen that the step collides with its neighbors on the average once in an interval $L_C = 4\ell^2\beta\tilde{\gamma}$. The length L_C is called *collision length*.

Similarly to the spatial correlations, also the temporal correlation function of a step may be deduced from Eq. (4.21), yielding for stationary fluctuations $t, t' \to \infty$

$$C(t) \equiv g(x,x,t,t') = \frac{2}{L_x\beta\tilde{\gamma}} \sum_{q\neq 0} \frac{1}{q^2}\left(1-e^{-|t-t'|/\tau_n}\right) = \frac{2}{\pi\beta\tilde{\gamma}}\Gamma(1-1/2n)(\alpha_n|t-t'|)^{1/2n}, \tag{4.23}$$

where the last form is obtained in the limit $L_x \to \infty$ by replacing the sum with an integral. Again the mean collision time of neighboring steps may be estimated by $\sqrt{C(t_C)} \sim 2\ell$. One space scales smaller than L_C and time scales shorter than t_C, the steps can be regarded essentially as independent objects, simplifying the treatment. Note that for large terraces and low temperatures L_C and t_C may well be macroscopic scales. With this restriction the results of a Langevin theory of a single step can be directly applied.

The step correlation functions are very useful in experimental determination of the activation energies, as they relate directly measurable mesoscopic quantities to the microscopic parameters. An example of the application of the correlation function is the determination of the kink energy from the spatial correlation function. Correlation function $G(x)$ obtained from STM measurements [27, 29] show, that it is indeed a linear function of the displacement x. From the slope of $G(x)$ the kink energy E_k can be deduced; the slope depends on the step stiffness, which in turn depends on the kink-energy through Eq. (3.34).

Also the time correlation functions can be used to extract microscopic parameters. In an elegant experiment Giesen *et al.* [20, 22, 23] have measured the time correlations by running the STM tip along same line repeatedly, obtaining this way a time series of the step position. The experimental findings were consistent with mass conserving dynamics ($C(t) \sim t^{1/4}$), indicating that at the temperature used in the experiment adatoms were bound to the steps and the only means of mass transport was migration along the step. [2] Applying the Langevin theory from the previous section to this case

[2] In long time- and space scales detachment from the steps dominates the dynamics and the

yields the correlation function in the stationary state as

$$C(t) \equiv \langle [\zeta(x,t) - \zeta(x,0)]^2 \rangle = \frac{2\Gamma(3/4)}{\pi} \frac{\sqrt{\Omega}}{\beta\tilde{\gamma}} (\sigma\tilde{\gamma}t)^{1/4}, \tag{4.24}$$

where $\zeta(x,t)$ denotes the step position in y-direction, $\Gamma(3/4) \approx 1.2254...$, and σ denotes again the adatom mobility along the step edge, defined through Eq. (4.3).

To make use of the expression (4.24), the parameters have to be written in terms of the rates of the elementary processes. The stiffness is $\tilde{\gamma}$ was already presented in Eq. (3.34). The mobility σ can be calculated exactly if the step is considered as a 1D SOS surface with Arrhenius kinetics (see. Sect.3.2); *i.e.* the activation energies for hopping are proportional to the number of lateral bonds in the *initial* state only. The exact result for the mobility for the Arrhenius case reads [40]

$$\sigma = \frac{a\Gamma_0\beta}{2} \exp(-\beta E_{det}), \tag{4.25}$$

where E_{det} denotes the activation energy for detachment of a step atom from a kink site, illustrated in the cartoon 4.1, and Γ_0 is the attempt frequency, which is assumed to be the same for all processes. Since the detachment of a kink atom creates two new kinks, in the Arrhenius model the detachment barrier is simply $E_{det} = E_{st} + 2E_K$, where E_{st} is the energy barrier for diffusion along a straight step and E_K is the kink energy encountered in Sect. 3.2. The relation $\sigma \sim e^{-\beta E_{det}}$ is intuitively clear, since the detachment from a kink is the rate limiting processes for migration along a kinked step. This relation has also been derived within a Kubo formalism [67, 95].

The correlation function (4.24) can be written as

$$C(t)/\Omega = g \times \left(\frac{t}{\tau_{st}}\right)^{1/4} \tag{4.26}$$

where g is a numerical constant of order unity, $\Omega = a^2$ the atomic area and

$$\tau_{st} = \tilde{\gamma}^3/\sigma \tag{4.27}$$

is the characteristic time it takes for the step to move one lattice constant in the direction perpendicular to the step due to the thermal fluctuations. At low temperatures, $\beta E_k \gg 1$, the step stiffness depends on the temperature as $\tilde{\gamma} \sim \exp(\beta E_k)$ (see Eq. (3.34)) and consequently the characteristic time as

$$\tau_{st} \sim \exp[\beta(E_{det} + 3E_k)]. \tag{4.28}$$

The activation energies can now be determined from experimental data by using equations (4.26) and (4.28). For example, provided that the kink energy is known from other experiments (spatial correlation function [27] or equilibrium island shapes [21]), the detachment barrier E_{det} can be deduced by calculating the characteristic time τ_{st} from the time correlation function [33].

correlation function scales as $C(t) \sim t^{1/2}$ [19]

4.3.1 Kink-rounding barriers

The kink rounding barriers that hinder adatoms from hopping around kink sites are of central importance for the growth, discussed in the following chapters. The cartoon presented in Fig. 4.1 illustrates the meaning of kink barriers. Such barriers also influence the time correlation function (4.24) through the mobility σ. Implementing kink rounding barriers on a 1D SOS model unavoidably breaks the Arrhenius character of the hopping rates and the analytical result (4.25) cannot be directly applied. At the kink site the hopping rate depends on the direction of the hop and therefore knowledge about the final state after the transition must be included in the rates.

The mobility can however be derived from scaling arguments. To this end it is instructive to re-derive the characteristic time τ_{st} for the Arrhenius model [33]. The elementary process behind step fluctuations is the transport of one adatom from one kink to a neighboring one, causing the kinks to diffuse along the step. Adatoms are detached from a kink site with a rate $\Gamma_{det} = \Gamma_0 \exp(-\beta E_{det})$. The probability of reaching the neighboring kink, without being recaptured at the initial position, can be calculated from random walk theory, and reads [31]

$$P_{att}(\ell) \approx \frac{a}{L}, \tag{4.29}$$

where L is the distance to the next kink and a the lattice constant in the step direction. The mean kink separation is $L_k = (1/2)ae^{\beta E_k}$ and the kink diffusion rate $\Gamma_{det} P_{att}(L_k)$. In order to move the step one lattice constant in the perpendicular direction, a kink must diffuse over a distance L_k. Putting everything together gives the characteristic

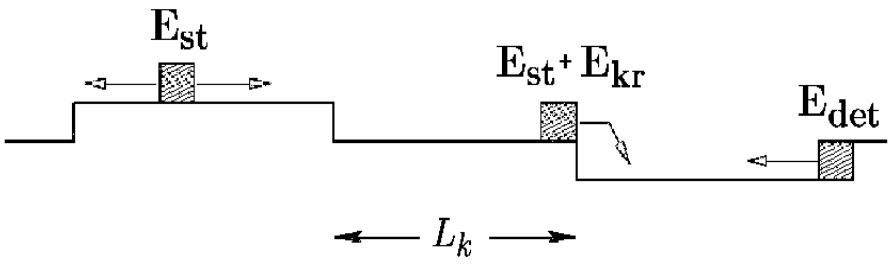

Figure 4.1: A schematic picture of a monoatomic step with the activation energies of the elementary processes.

time of step fluctuations as

$$\tau_{st} \sim L_k^2/(\Gamma_{det} P_{att}(L_k)) \sim \exp[\beta(3E_k + E_{det})], \tag{4.30}$$

in agreement with expression (4.28)

When hopping around a kink site is suppressed by an additional barrier E_{kr}, the probability of reaching the neighboring step $P_{att}(L)$ has to be modified [33]. Again the result can be obtained from the random walk theory as [31]

$$P_{att}(L) \approx \left(\frac{L}{a} + \frac{1}{p_{kr}}\right)^{-1}, \tag{4.31}$$

where $p_{kr} \approx \exp(-\beta E_{kr})$ is the probability for going around a kink (see Fig. 4.1), instead of being reflected. The kink rounding barriers are obviously relevant if $E_{kr} > E_k$. Inserting (4.31) into Eq.(4.30) yields

$$\tau_{st} \sim \exp\left[\beta(2E_k + E_{det} + E_{kr})\right], \tag{4.32}$$

for strong kink rounding barriers $E_{kr} \gg E_k$. As shown in the previous section, the characteristic time is generally a combination of the step adatom mobility and the step stiffness, $\tau_{st} \sim \tilde{\gamma}^3/\sigma$. Since the step stiffness is a static quantity, depending only on the energetics but not on the dynamics of the atoms along the steps, it may be concluded that the mobility is reduced by the kink barriers to

$$\sigma \sim \exp(-\beta(E_{det} + E_{kr} - E_k)). \tag{4.33}$$

An interpolation formula

$$\sigma = \frac{a\Gamma_0\beta}{2} \frac{e^{-\beta E_{det}}}{1 + e^{\beta(E_{kr} - E_k)}} \tag{4.34}$$

recovers both of the expressions (4.25) and (4.33) at the limits $E_{kr} \ll E_k$ and $E_{kr} \gg E_k$ respectively.

4.3.2 Monte Carlo simulations of step fluctuations

Monte Carlo simulations can be used to check the results obtained from the scaling arguments. Since the interest here is on the dynamics of adatoms along the step with no detachment from the steps, a simple one dimensional SOS model can be used as a model for the step (see Sect. 3.2 for discussion of SOS model). The position of the step at site i is ζ_i and the atoms may hop along the step to neighboring sites ($i \to i \pm 1$) with hopping rates

$$\Gamma_{i,i\pm1} = \Gamma_0 \exp(-\beta E_{i,i\pm1}). \tag{4.35}$$

The activation energy depends on the local configuration through

$$E_{i,i\pm1} = E_{st} + 2E_k n_i + [1 - \delta(\zeta_i - \zeta_{i\pm1} - 1)]\, E_{kr}, \tag{4.36}$$

where $n_i = 0, 1, 2$ is the number of lateral nearest neighbors at initial site i. E_{kr} is an extra barrier suppressing kink rounding; whenever the hop from $i \to i \pm 1$ is *not* along a flat step *i.e.* $\zeta_i - \zeta_{i\pm1} \neq 1$, the extra barrier E_{kr} is added.

The simulations were conducted on a lattice of size $L_x = 131072$, using a flat step $\zeta_i(0) \equiv 0$ as initial condition. The diffusion rate along the flat step $\Gamma_0 \exp[-\beta E_{st}]$ sets the time scale and was set to unity in the simulations. For the kink energy a value $E_k = 0.1$ eV was used and the kink-rounding barrier E_{kr} was varied between 0 and 0.24 eV. The temperature range used was $\beta E_k = 1.25 - 3.5$, which corresponds to interval $T = 331 - 928$ K for the chosen value of E_k.

In the simulations it is more convenient to measure the step width W instead of the correlation function. Starting with a flat initial condition $\zeta_i \equiv 0$ one finds for the step width an expression

$$W^2(t) \equiv \frac{1}{L_x} \sum_{i=1}^{L_x} \zeta_i(t)^2 = 2^{-3/4} C(t), \tag{4.37}$$

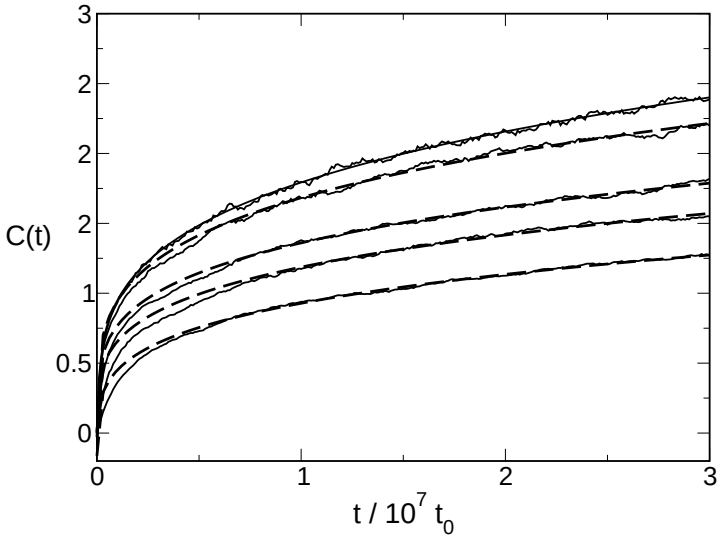

Figure 4.2: The time correlation function (Eq. (4.37)) for $\beta E_k = 2.5$ and $E_{kr}/E_k = 0.0/0.4/1.2/1.6/2.0$ (from top to bottom). The dashed line is the best fit $At^{1/4} + B$. Time is measured in units of the inverse diffusion rate along a flat step, $t_0 \equiv 1/(\Gamma_0 \exp[-\beta E_{st}])$

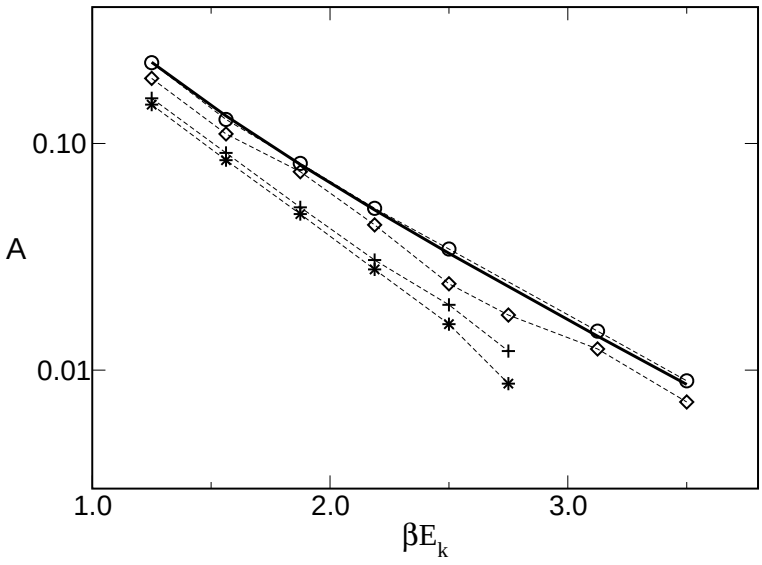

Figure 4.3: The pre-factor of the correlation function (Eq. (4.37)) obtained from the fits in Fig. 4.2. $E_k = 0.1$ eV and kink rounding barrier $E_{kr}/E_k = 0.0(\bigcirc), 1.2(\diamond), 1.6(+), 2.4(*)$. The full line is the exact result for the Arrhenius model $E_{kr} = 0$

where $C(t)$ is the time-correlation function (4.23). The step width measured form the simulations for various values of kink rounding barrier E_{kr} are presented in Fig. 4.2. The correlation function is seen to have a clear $\sim t^{1/4}$ time dependence. Fitting the simulation data with $C(t) = At^{1/4}+B$ in the long time limit allows the determination of the characteristic time through (4.26). The pre-factor A obtained from the best fits are shown in Fig. 4.3. The curves do not have a pure exponential temperature dependence since the step stiffness depends on the temperature as $\tilde{\gamma} \sim \beta^{-1} \sinh^2(\beta E_k/2)$, and are seen to be curved in Fig. 4.3 for high temperatures $\beta E_k \lesssim 2$. The stiffness $\tilde{\gamma}$ is a quantity describing the stationary properties of the step and thus depends only on the energetics of the model, but not on the dynamics. This means that it is independent of the kink-rounding barrier E_{kr} and can be removed from the pre-factor A.

After removal of the step stiffness from the pre-factor $A' = A \times (\beta\tilde{\gamma})^{3/4}$, it depends only on the mobility $A' \sim (\sigma/\beta)^{1/4} \sim \exp(-\beta E_\sigma/4)$ (see Eqs. (3.34) and (4.34)), where E_σ is the activation energy for the mobility σ. The simulation results for the mobility for different values of E_{kr} are shown in Fig. 4.4. The Langevin theory is strictly speaking valid only when the atomistic effects in the dynamics can be neglected, meaning that the step width W should be larger than one $W^2 > 1$. Unfortunately it takes a long time to reach this regime in the simulations, in particular for low temperatures $\beta E_k \gtrsim 2$ and large kink-rounding barriers. Thus the fits in the form $C(t) = At^{1/4} + B$ for large

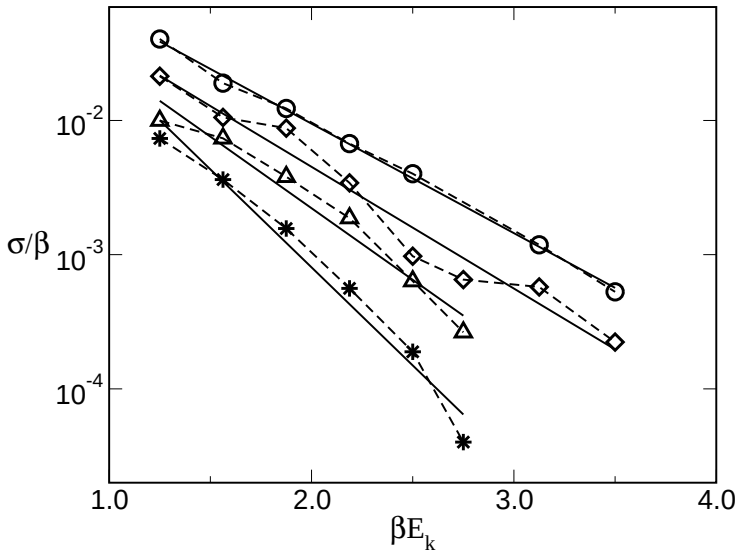

Figure 4.4: The adatom mobility along the step edge obtained from the pre-factor of the correlation function in Fig. 4.2, with $E_k = 0.1$ eV and kink rounding barrier $E_{kr}/E_k = 0.0(\bigcirc), 1.2(\diamond), 1.6(\triangle), 2.4(*)$. The full lines are best fits to an Arrhenius form.

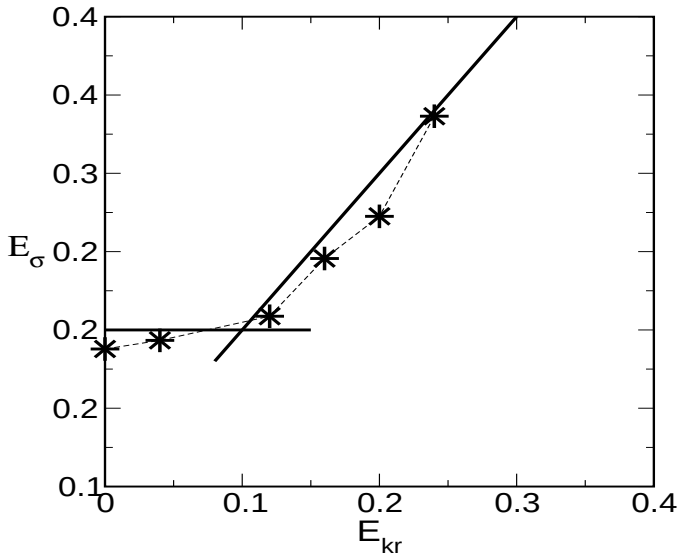

Figure 4.5: The activation energy for the adatom mobility obtained from the fits in Fig 4.4. A clear cross-over in the behavior is seen at $E_{kr} \approx E_{kr} = 0.1$. The full lines are the theoretical predictions Eqs. (4.25) and (4.33).

kink-rounding barrier E_{kr} are done partially in regime $W < 1$, which leads to uncertainty in the fitting parameters and scattering of the simulation results.

From the Arrhenius plots in Fig. 4.4 one obtains the activation energies for the adatom mobility, Eqs. (4.25) and (4.33). The simulation result for the activation energy, plotted in Fig. 4.5, are seen to be in good agreement with the theoretical results. The mobility has a clear cross-over in the behavior, as the kink rounding barrier increases, taking place around $E_{kr} \approx E_k$ as expected on the basis of the scaling arguments presented in the previous section. Thus the simulation results confirm the validity of the scaling arguments.

Chapter 5

The step meandering instabilities

The central theme of this thesis are the step meandering instabilities. When the meander of the steps has the same phase over multiple steps long ripples appear on the surface. The meandering of steps may have different underlying microscopic mechanisms. Two different mechanisms known to produce ripples are presented and compared in this chapter. In many growth experiments the atomic steps are found to form an in-phase meander pattern. To which of the two instabilities presented here they can be related is still an open question. The instabilities look qualitatively the same, but differ in their characteristic length scales. Quantitative measurements are thus needed in order to recognize the instabilities.

5.1 The Bales-Zangwill instability

The first step instability was theoretically predicted by Bales and Zangwill in 1990 [4]. They based their theory on the BCF model of the step-flow growth and showed through linear stability analysis that a straight steps are linearly unstable against long wavelength perturbations. In the original work of Bales and Zangwill only an in-phase step train was considered, but soon afterward their results were generalized to arbitrary phase differences [65].

5.1.1 Heuristic derivation

The reason behind the instability is the Ehrlich-Schwoebel barrier suppressing the inter-layer mass transport. As discussed in the Chapter 2, such barriers cause mound formation on a growing singular surface [71,94] and they stabilize the inter-step distance in step-flow growth [39]. However, as the vicinal surface is stabilized in the direction perpendicular to the steps, it is destabilized in the step direction. The reason of the step meandering is intuitively as follows: due to the ES-barrier the atoms landing on a

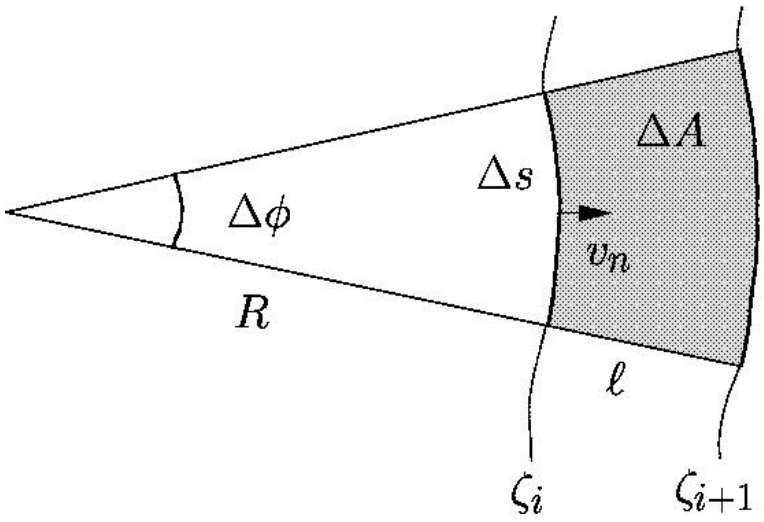

Figure 5.1: An illustration of the Bales-Zangwill instability. The instability has a geometrical origin; positively curved steps receive more adatoms from the terrace in front of then per unit step length.

terrace preferably attach to an *ascending* step. Thus the rate at which mass arrives to a step, and consequently the velocity of the step, depend on the terrace area per unit step length in front of the step. The cartoon in Fig. (5.1) clarifies the situation. The step normal velocity is $v_n = \Omega F \Delta A/\Delta s$, where ΔA is the terrace area in front of the step and $\Delta s = R\Delta\phi$ the arc-length (See fig. 5.1), R denotes the radius of curvature of the step. The terrace area ΔA can be calculated by approximating it locally as a segment of a circle

$$\Delta A = \frac{1}{2}\left(R+\ell\right)\Delta\phi\left(R+\ell\right) - \frac{1}{2}R\Delta\phi R = \frac{1}{2}\Delta\phi\left(2R\ell+\ell^2\right). \tag{5.1}$$

Inserting the radius of the curvature $R^{-1} = \kappa \approx -\partial_{xx}\zeta$, the velocity of the step reads

$$v_n = \Omega F \ell - \frac{\Omega F \ell^2}{2}\partial_{xx}\zeta. \tag{5.2}$$

Here it has been assumed that the ES-barrier is complete; *all* atoms arriving on the terrace go to an ascending step. It is also assumed that $1/R \ll 1$, *i.e.* the step deformation is small.

One yet has to take into account the relaxation of the step morphology as described in the previous chapter. Since there is no desorption to the gas phase, the relaxation takes place via mass current along the step or through terrace diffusion. Because of the complete ES-barrier, all adatoms that detach from the step, must re-attach to it later.

Thus also the mass transfer through terrace diffusion also obeys mass conservation and can be written as an effective current along the step. The effective mobility for the relaxation via terrace diffusion reads $\sigma_{eff} = \ell\beta D c_{eq}$ [38, 68], where D is the terrace diffusion constant and c_{eq} adatom concentration on the terrace. The mobility depends on the terrace width ℓ, since the number of adatoms on the terrace n, contributing to the relaxation current, depends on the terrace width $n \sim \ell$. In the language of Ref. [68]: the terrace width ℓ is the width of the channel of mass transport. The relaxational part of the equation of motion to linear order may now be written exactly as in Eq. (4.4) in Sect. 4.1

$$\frac{\partial \zeta}{\partial t} = -\Omega \frac{\partial}{\partial x} \left(\sigma + \ell\beta D c_{eq}\right) \frac{\partial \mu_{st}}{\partial s}. \tag{5.3}$$

Here σ is the usual mobility of adatoms along the step, corresponding to the relaxation through step edge diffusion and the second term derives from the relaxation through terrace diffusion. The driving force for both of these currents is the gradient in the step chemical potential μ_{st}.

Inserting the expression for the chemical potential (again to the linear order) $\mu_{st} = \Omega\tilde{\gamma}\partial_{xx}\zeta$, the equation of motion for the steps follows

$$\frac{\partial \zeta}{\partial t} = \Omega F \ell - \frac{\Omega F \ell^2}{2} \frac{\partial^2 \zeta}{\partial x^2} - \Omega^2 \left(\sigma + \ell\beta D c_{eq}\right) \tilde{\gamma} \frac{\partial^4 \zeta}{\partial x^4}, \tag{5.4}$$

to leading order. Inserting a profile with small amplitude modulations and a wavelength $2\pi/q$, $\zeta \sim f(t)\sin(qx)$ shows that straight steps are unstable against long wavelength perturbations

$$\zeta \sim e^{\omega t}\sin(qx)\ ,\ \omega = \frac{\Omega F \ell^2}{2} q^2 - \Omega^2 \tilde{\gamma} \left(\sigma + \ell\beta D c_{eq}\right) q^4. \tag{5.5}$$

From this form it is clear that modes with a wavenumber smaller than

$$q_c = \sqrt{\frac{F\ell^2}{2\Omega\tilde{\gamma}\left(\sigma + \ell\beta D c_{eq}\right)}} \tag{5.6}$$

grow exponentially, destabilizing the step train.

5.1.2 Linear stability analysis

The results derived heuristically in the previous section can be confirmed by a more controlled calculation, namely the linear stability analysis of the BCF equations

$$\begin{aligned} D\nabla^2 c_i(\mathbf{x},t) + F &= 0 \\ D\nabla \cdot c_i(x,\zeta_i) &= k_+ \left[c(\mathbf{x},t) - c_{eq}\right] \\ -D\nabla \cdot c_i(x,\zeta_{i+1}) &= k_- \left[c(\mathbf{x},t) - c_{eq}\right] \\ v_i^n(x) = \Omega D \left[\mathbf{n}_i \cdot \nabla c_i(x,\zeta_i) - \mathbf{n}_{i-1} \cdot \nabla c_{i-1}(x,\zeta_i)\right] &- \sigma\Omega^2\tilde{\gamma}\partial_s^2\kappa_i(x), \end{aligned} \tag{5.7}$$

where the last term in the equation for the step velocity describes the line diffusion along the step edge (see Eq.(4.4)). The linear stability analysis proceeds by insertion of a Fourier decomposition of the concentration field and the step profiles to Eqs. (5.7)

$$\hat{\zeta}(q,\omega,\phi) = \sum_{j=-\infty}^{\infty}\int_{\infty}^{\infty} \mathrm{d}x\mathrm{d}t\ \zeta_j(x,t)e^{\omega t - i(qx+\phi j)} \tag{5.8}$$

$$\hat{c}(q,y,\omega,\phi) = \sum_{j=-\infty}^{\infty}\int_{\infty}^{\infty} \mathrm{d}x\mathrm{d}t\ c_j(x,y,t)e^{\omega t - i(qx+\phi j)} \tag{5.9}$$

$$\tag{5.10}$$

and dropping all but the linear terms. For a linear system different Fourier modes do not couple and can be treated separately.

The growth rate ω is a complex function of the wave number q and phase shift ϕ. After some amount of algebra the real part follows as [24, 65]

$$\begin{aligned}\mathcal{R}e[\omega] &= \Omega F \frac{q}{\mathcal{G}(q)}\left(\frac{\ell_+ + \ell_-}{\ell + \ell_- + \ell_+}\right) \\ &\times \left\{(\ell_+ + \ell_-)\Big[q\ell\sinh(q\ell) - \cosh(q\ell) + \cos(\phi)\Big] + (q\ell^2/2)\sinh(q\ell)\right\} \\ &- \tilde{\gamma}\Omega^2 q^2\left\{D\beta c^0_{eq}\frac{q}{\mathcal{G}(q)}\Big[2\cosh(q\ell) - 2\cos(\phi) + q(\ell_+ + \ell_-)\sinh(q\ell)\Big] + \sigma q^2\right\},\end{aligned} \tag{5.11}$$

with the length scales $\ell_\pm \equiv D/k_\pm$ and

$$\mathcal{G}(q) = (\ell_+ + \ell_-)q\cosh(q\ell) + (\ell_+\ell_- q^2 + 1)\sinh(q\ell) \tag{5.12}$$

The imaginary part results as [24]

$$\mathcal{I}m[\omega] = \Omega F \sin(\phi)\frac{q}{\mathcal{G}(q)}(\ell + \ell_+ + \ell_-) \tag{5.13}$$

The imaginary part $\mathcal{I}m[\omega]$ describes the propagation of the perturbation and the real part $\mathcal{R}e[\omega]$ the decay/growth of the amplitude. To see the meaning of the imaginary part, it is instructive to consider the two possible types of phase shifts, illustrated in Fig. 5.2. The phase shift can describe the modulation of the perturbation amplitude [1] $\zeta^{(1)}_m(x,t) \sim e^{\omega t}\cos(qx)\cos(\phi m)$ or the shift of the minima and maxima in the perturbation in the step direction $\zeta^{(2)}_m(x,t) \sim e^{\omega t}\cos(qx - \phi m)$, as illustrated in Fig. 5.2. Both of these perturbations can be written in terms of the Fourier modes

[1] This type of perturbation describes for $q = 0$ *step bunching*

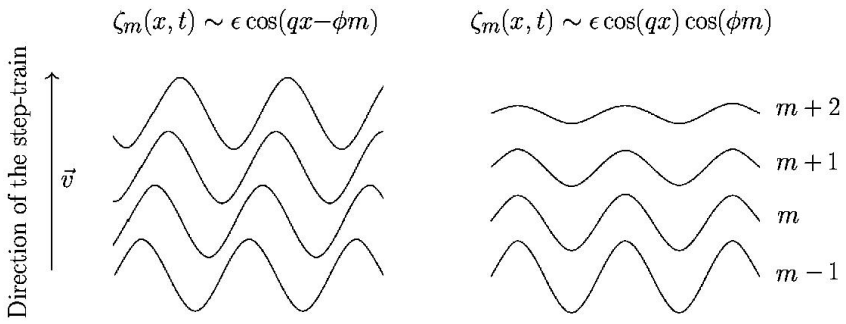

Figure 5.2: An illustration of the two possible types of phase shifts ϕ.

$\zeta_m(x,t) \sim e^{\omega t - i(qx+\phi m)}$. It is easy to see that for both perturbations the real part $\mathcal{R}e[\omega]$ is equal. A simple calculation leads to time evolution of the perturbations as

$$\begin{aligned} \zeta_m^{(1)}(x,t) &\sim e^{\mathcal{R}e[\omega]t}\cos(qx)\cos\left(\phi m + \mathcal{I}m[\omega]t\right) \\ \zeta_m^{(2)}(x,t) &\sim e^{\mathcal{R}e[\omega]t}\cos\left(qx - \phi m - \mathcal{I}m[\omega]t\right). \end{aligned} \tag{5.14}$$

Thus the modulation in the perturbation amplitude is advected backwards in the coordinate frame moving with the step train with a velocity $v_{adv} \sim \mathcal{I}m[\omega]$ [24]. For the other type of phase shifts $\zeta_m^{(2)}(x,t)$, the imaginary part $\mathcal{I}m[\omega]$ describes the motion of the maxima and minima in the step direction, with a velocity $\mathcal{I}m[\omega]$. For complete ES barrier, the time evolution of a step depends only on the position of the step in front of it since new mass can arrive to it only from the terrace in front. The imaginary part thus expresses the tendency of a step to follow the step in front of it. It is then intuitively clear that for random phase-shifts between neighboring steps, as each step follows the preceding one, the step train organizes in to an in-phase mode and the typical time scale of the ordering is given by $t_\phi = (\mathcal{I}m[\omega])^{-1}$.

The real part of $\omega(q,\phi)$ is the growth rate of the corresponding Fourier mode. Positive real part is a sign of an instability, the amplitude of such modes grows exponentially with rate $\mathcal{R}e[\omega]$. The messy expression (5.11) is simplified by noting that the fastest growing modes, and thus relevant, are the ones in-phase $\phi = 0$ [2] and taking the long wavelength limit $q\ell \ll 1$

$$\mathcal{R}e[\omega] = \frac{\Omega F \ell^2}{2}\left(\frac{\ell_- - \ell_+}{\ell_+ + \ell_- + \ell}\right) q^2 - \Omega^2 \tilde{\gamma} q^4 \left(D\beta c_{eq}^0 \ell + \sigma\right). \tag{5.15}$$

This expression confirms the result (5.5), derived heuristically in previous section in the relevant limit $\ell_- \to \infty$.

[2]The step train also evolves naturally into an in-phase mode in time scale $t_\phi \ll (\mathcal{R}e[\omega])^{-1}$. This point is discussed later in the text.

Thus it is seen that a step-train is unstable against long wavelength meandering. The instability arises from the geometry; deposited material is distributed unevenly along the steps, deriving form the asymmetric attachment kinetics at the step edges, as explained in Sect. 5.1.1. For the symmetric attachment kinetics $\ell_- = \ell_+$ the instability disappears ($\mathcal{R}e(\omega) \leq 0$ for every q). The fastest growing mode is the in-phase mode with a wavelength.

$$\lambda_{BZ} = 4\pi\sqrt{\frac{\Omega\tilde{\gamma}\left(\sigma + \ell\beta D c_{eq}^0\right)}{F\ell^2 f_s}}, \tag{5.16}$$

where the strength of the ES-barrier appears in factor $f_s = (\ell_- - \ell_+)/(\ell_+ + \ell_- + \ell)$. λ_{BZ} is commonly referred as the Bales-Zangwill wavelength. This is the mode that will dominate the spectrum after initial growth and thus the characteristic length of the Bales-Zangwill instability. As the steps meander in-phase, they form long ripples on the surface, like the ones shown in Fig. 2.6.

5.2 Nonlinear evolution equation

The question that remains is what happens after the linear regime? Obviously the linear approximation will break down after the initial growth. The most unstable mode grows with a rate $\omega_{BZ} \equiv \mathcal{R}e[\omega(q_{BZ})]$ and after a time of the order of ω_{BZ}^{-1} the linear approximation ceases to be valid. An effective step evolution equation for the non-linear regime has been derived by Pierre-Louis *et al.* [24, 64]. They employed a multi-scale analysis of the BCF equations, which had been already successfully applied to the growth problem where desorption is present [7, 71].

5.2.1 Derivation

The analysis begins by identification of relevant space- and time scales. Obviously the relevant scale in the step direction is the meander wavelength λ_{BZ} and the time scale the inverse growth rate ω_{BZ}^{-1}. In the long wavelength regime one can identify a small parameter [24]

$$\epsilon \equiv 2q_{BZ}\ell = \sqrt{\frac{F\ell^4}{\Omega\tilde{\gamma}\left(\sigma + \ell\beta D c_{eq}^0\right)}} \ll 1. \tag{5.17}$$

In the original work the expansion was done in powers of the Péclet number Pe (3.27) introduced in Sect. 3.3 [64]. In later work by the authors a somewhat different expansion parameter $\varepsilon = \epsilon^2$ was chosen [24]. For both of these choices the expansion must be done in non-integer powers of the parameter $(\mathrm{Pe})^{n/2}$ or $\varepsilon^{n/2}$. Here a different expansion parameter is chosen merely for convenience, so that the expansion is in integer powers.

With the definition above, the relevant scales are seen to depend on the small parameter as $\lambda_{BZ} \sim \epsilon^{-1}$ and $\omega_{BZ} \sim \epsilon^4$. The strategy is now to write the BCF equations in a form such that the dependence of each term on ϵ is explicit and then expand the concentration c_i and step position ζ_i in powers of ϵ [24, 64]. It was shown in the previous section that the out-of-phase modes grow slower than the in-phase modes and that the meanders tend to order into the in-phase mode on a time scale $t_\phi = (\mathcal{I}m[\omega])^{-1} \sim \epsilon^{-2}$. For the step motion the relevant time scale is the growth rate $t_{BZ} = \omega_{BZ}^{-1} \sim \epsilon^{-4}$. Thus the step-train order into the in-phase mode on the time scale of the growth extremely rapidly $t_\phi / t_{BZ} \sim \epsilon^2$. Therefore is is justified to assume that all steps are in phase, and the whole profile is described by a single function $\zeta_i(x,t) \equiv \zeta(x,t)$, and of course also $c_i(x,y,t) = c(x,y,t)$, for all i.

To proceed one needs to know the leading order dependence of $c(x,y,t)$ and $\zeta(x,t)$ on the small parameter ϵ. A detailed analysis of the BCF equations, presented in Ref. [24], leads to scaling $\zeta \sim \epsilon^{-1}$ for the meander amplitude and $(c - c_{eq}^0) \sim \epsilon^1$ for the normalized concentration field. At first sight the relation $\zeta \sim \epsilon^{-1}$ seems pathological, as the amplitude diverges at the point around which the expansion is made $\epsilon \to 0$. However, due to translational invariance, the equations cannot depend directly on ζ but only on its derivatives. Since the relevant length in the step direction also scales as $x \sim \lambda_{BZ} \sim \epsilon^{-1}$ the derivatives have at most $(\partial_x^n \zeta)^m \sim \epsilon^0$ dependence [24].

Now scaled space and time variables can be defined as [3] $X = \epsilon x$ and $T = \epsilon^4 t$. Writing the BCF equations in terms of X and T and inserting the expansions

$$\begin{aligned} \zeta &= \epsilon^{-1} \left[H^{(0)} + \epsilon H^{(1)} + \epsilon^2 H^{(2)} ... \right] \\ c &= \epsilon \left[U^{(0)} + \epsilon U^{(1)} + \epsilon^2 U^{(2)} ... \right] \end{aligned} \tag{5.18}$$

the equations (5.7) may be expanded in powers of ϵ [24, 64]. Solving the equations subsequently for different powers ϵ^n, leads to a consistency condition for the ϵ^3 equation. From the consistency requirement the effective equation for the step train results to the first order as

$$\begin{aligned} \frac{\partial \zeta}{\partial t} &= -\partial_x \left\{ \frac{\Omega F \ell^2}{2} \frac{\partial_x \zeta}{1 + (\partial_x \zeta)^2} \right. \\ &+ \left. \left(\frac{\Omega \beta D \ell c_{eq}^0}{\sqrt{1 + (\partial_x \zeta)^2}} + \sigma \Omega \right) \frac{1}{\sqrt{1 + (\partial_x \zeta)^2}} \partial_x \left[\frac{\Omega \tilde{\gamma} \partial_{xx} \zeta}{(1 + (\partial_x \zeta)^2)^{3/2}} \right] \right\}. \end{aligned} \tag{5.19}$$

This equation corresponds to the case of a complete Ehrlich-Schwoebel barrier $\ell_- = \infty$, a finite ES barrier leads to an analogous expression. The explicit derivation of Eq. (5.19) is presented in the Appendix A.

The evolution equation (5.19) has a form of a conservation law, the time derivative of the step profile is a divergence of a current J. The equation must be mass conserving;

[3] Note that only the x-direction is scaled and y-direction left unscaled

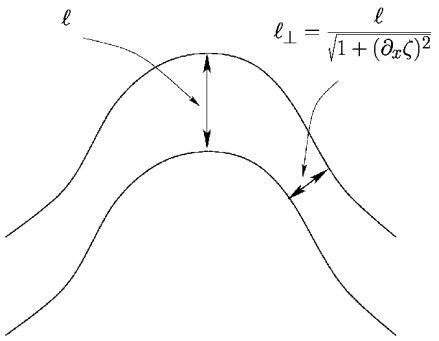

Figure 5.3: An illustration of the inter-step distance. The shortest distance between consecutive steps depends on the slope of the steps.

as there is no desorption and the complete ES barrier prohibits mass exchange between steps, implying that the mass of each step is conserved. In fact, the requirement of complete ES barrier may be relaxed without the loss of the mass conserving form of the evolution equation. If also the in-phase constraint is relaxed, the step dynamics are no longer mass conserving.

The terms present in the step equation (5.19) can be interpreted intuitively. The last term is clearly proportional to the variation of the step chemical potential μ

$$J \sim \partial_s \Omega \tilde{\gamma} \kappa \ , \ \partial_s = \frac{1}{\sqrt{1+(\partial_x\zeta)^2}} \partial_x \tag{5.20}$$

and thus describes step relaxation. The two coefficients in parenthesis in front of the $\partial_s \mu$ term are then effective mobilities. As already discussed in the previous section 5.1 the relaxation may take place either through current along the steps, having a mobility σ, or through diffusion via terraces, having an effective mobility $\Omega\beta D c_{eq}^0 \ell$. The term $[1+(\partial_x\zeta)^2]^{-1/2}$ appears in the mobility for the following reason: as mentioned in the previous section 5.1 the effective current over the terraces is proportional to the width of the terrace ℓ. Here the width is now the *actual* perpendicular distance between the steps. From the geometry it follows that the distance is [38]

$$\ell_\perp = \frac{\ell}{\sqrt{1+(\partial_x\zeta)^2}}, \tag{5.21}$$

as illustrated in Fig. 5.3

The first term in Eq. (5.19) is proportional to the deposition flux $\sim F$ and is then obviously of non-equilibrium origin. The reason for this term is the uneven distribution

of deposited mass along the steps, as discussed in Sect. 5.1.1. The form may be deduced from a geometrical construction [24], similar to the one presented to explain the origin of the Bales-Zangwill instability in Sect. 5.1.1.

5.2.2 Asymptotic step profiles

The evolution equation (5.19) obviously reproduces the results of the linear stability analysis when the slopes are small $\partial_x\zeta \ll 1$, which it has to as the linear analysis was the starting point of the derivation of the equation. The interest here is on the solutions of the whole equation. In the following the two relaxation mechanism will be considered separately. Then the Eq. (5.19) reads

$$\begin{aligned} \partial_t\zeta &= -\partial_x\left[J(\partial_x\zeta)\right] \\ J &= \frac{P\partial_x\zeta}{1+(\partial_x\zeta)^2} + \frac{Q_n}{\left[1+(\partial_x\zeta)^2\right]^n}\partial_x\left[\frac{\partial_{xx}\zeta}{(1+\partial_x\zeta)^2)^{3/2}}\right], \end{aligned} \tag{5.22}$$

where P and Q_n are constants. $n=1$ corresponds to the terrace diffusion $P=\Omega F\ell^2/2$, $Q_1=\Omega^2\beta\tilde{\gamma}D\ell c_{eq}^0$ and $n=1/2$ to step diffusion $Q_{1/2}=\Omega^2\sigma\tilde{\gamma}$. Two types of analytical results can be found to step equation (5.22): *stationary* solutions, which are obtained by setting the current to zero $J\equiv 0$, and *separable* solution of the form

$$\zeta(x,t) = F(t)g(x). \tag{5.23}$$

Since the equations (5.22) differ only by the exponent n, they may be treated on equal footing. The stationary profile can be solved by employing a transformation of variable

$$M(x) \equiv \frac{\partial_x\zeta}{\sqrt{1+(\partial_x\zeta)^2}}, \tag{5.24}$$

after which the current has an expression

$$J = Q_n\partial_{xx}M + PM\left(1-M^2\right)^{1/2-n}. \tag{5.25}$$

Setting $J=0$ the equation takes the form of a Newton's equation describing a particle with coordinate M and mass Q_n in a potential $U(M)$ and the variable x plays the role of time

$$Q_n\frac{\mathrm{d}^2M}{\mathrm{d}x^2} = -\frac{\mathrm{d}U(M)}{\mathrm{d}M}\ ,\ U(M)\equiv -P\frac{(1-M^2)^{3/2-n}}{3-2n} \tag{5.26}$$

Now, using the "energy conservation" it follows immediately that

$$\frac{\mathrm{d}M}{\mathrm{d}x} = \sqrt{\frac{2}{Q_n}}\left[U(M_0)+P\frac{(1-m^2)^{3/2-n}}{3-2n}\right]^{1/2}, \tag{5.27}$$

where M_0 is the maximum value of M, corresponding to the maximum slope in the profile $\zeta(x)$

$$M_0 = \frac{S}{\sqrt{1+S^2}} \ , \ S \equiv \max_x[\partial_x \zeta], \tag{5.28}$$

for $S \to \infty$ we have $M_0 \to 1$. The resulting one-parameter family of profiles are most conveniently parametrized using M_0. The stationary profile may be solved using this result; the profile cannot be written in a closed form for general n, but it follows from integrals

$$\begin{aligned} \zeta &= \sqrt{\frac{2Q_n(3-2n)}{P}} \int_0^{M'} \frac{\mathrm{d}M \ M}{\left\{(1-M^2)\left[(1-M^2)^{3/2-n} - (1-M_0^2)^{3/2-n}\right]\right\}^{1/2}} \\ x &= \sqrt{\frac{8Q_n(3-2n)}{P}} \int_0^{M'} \mathrm{d}M \left[(1-M^2)^{3/2-n} - (1-M_0^2)^{3/2-n}\right]^{-1/2} \end{aligned} \tag{5.29}$$

by eliminating M' from the equations. In particular, the amplitude and the wavelength of the stationary profile are obtained if the integration limit is set to $M' = M_0$ (actually one quarter of the wavelength $\Lambda/4$ and one half of the amplitude $\mathcal{A}/2$ follow from the integrals extended from 0 to M_0).

For the edge diffusion case $n = 1/2$ the potential $U(M)$ is harmonic and the wavelength (period of the oscillations in the language of Newton's mechanics) is independent of the maximal value M_0. Thus all stationary profiles have the wavelength $\Lambda(M_0)$ of the first unstable mode (5.6) $\Lambda(0) = \lambda_c$. This mode can be considered as stationary since it has a growth rate $\mathcal{R}e(\omega) = 0$. The amplitude $\mathcal{A}(M_0)$ of the profile is an increasing function of the maximum slope M_0 and it varies between $\mathcal{A}(0) = 0$ and $\mathcal{A}(1) = \infty$. For terrace diffusion $n = 1$ the potential is steeper than harmonic and the wavelength is therefore a decreasing function of M_0 (for Newton's equation: the period of oscillations decreases as the amplitude M_0 increases). Again for zero slope $M_0 = 0$ the wavelength $\Lambda(M_0 = 0) = \lambda_c$ and the upper limit follows from integral (5.29) $\Lambda(1) = \sqrt{2\pi Q_1/P}\,\Gamma(3/4)\Gamma(5/4) \approx 0.5395327\lambda_c$; the amplitude is also finite, having a limiting value $\mathcal{A}(1) = \sqrt{8Q_1/P}$.

In addition to the stationary solutions, separable solutions to Eq. (5.22), with a fixed wavelength λ_s, can be found. Inserting a separable ansatz

$$\zeta(x,t) = K(t)g(x) \tag{5.30}$$

it is seen that the relaxation terms vanishes as K^{-3} compared to the first term [64]. Thus in the long time limit, if $K \to \infty$ as $t \to \infty$, the second term is negligible if the slope differs from zero $g'(x) \neq 0$. Dropping the relaxation term, the step equation (5.22) reduces to

$$K\frac{\mathrm{d}K}{\mathrm{d}t} = P\frac{\mathrm{d}^2 g}{\mathrm{d}x^2}\left[g\left(\frac{\mathrm{d}g}{\mathrm{d}x}\right)^2\right]^{-1} = \mathcal{C}, \tag{5.31}$$

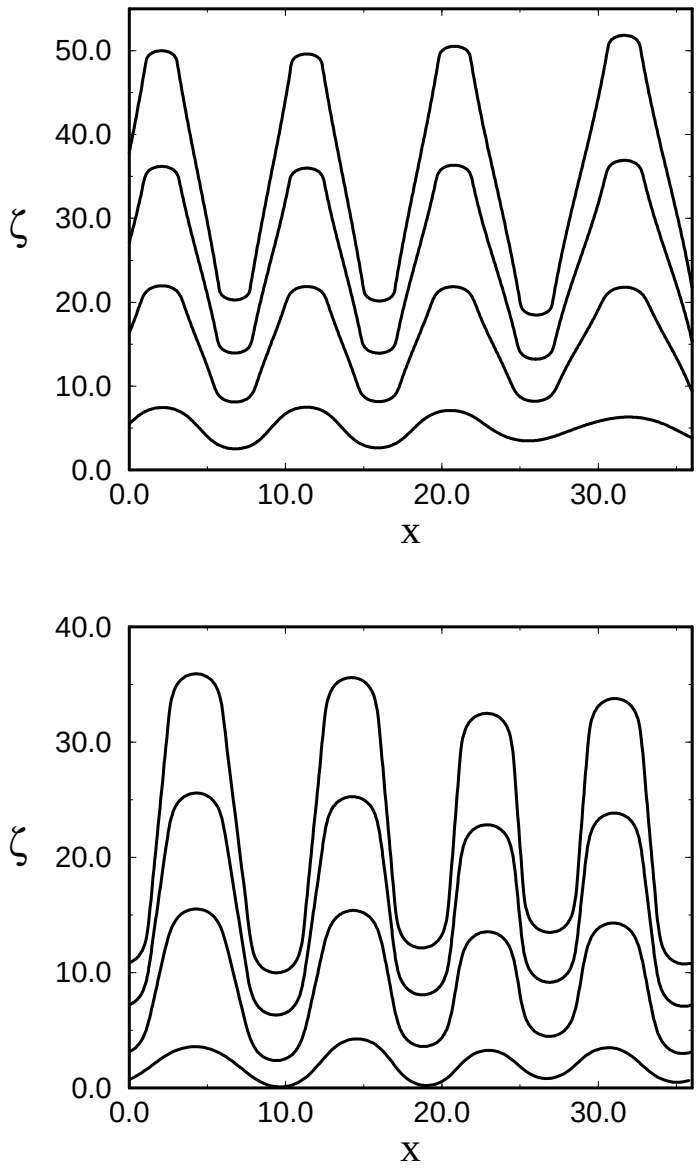

Figure 5.4: The evolution of the step profile starting from a flat initial condition with small random fluctuations. The upper figure shows the case of attachment-detachment kinetics (Eq.(5.19)) at times $t = 36, 64, 110, 183$, the lower figure the case of edge diffusion (Eq.(5.22) with $n = 1/2$) at times $t = 20, 60, 112, 200$. Subsequent profiles have been shifted in the ζ-direction. In all figures spatial variable x has been scaled by $\lambda_c/2\pi = \sqrt{Q_n/P}$ and time by Q_n/P^2.

where $\mathcal{C}$ is a constant. This equation is of course identical for both relaxation mechanisms since the relaxation term is irrelevant. The obvious solution for the temporal part is $K = \sqrt{\mathcal{C}t}$. The equation for the spatial part has been solved already in the context of mound growth on a singular surface [37] and the solution reads $g = \lambda_s/(2\sqrt{\pi})\mathrm{erf}^{-1}(4x/\lambda_s - 1)$. Here $\mathrm{erf}^{-1}(x)$ denotes the inverse of the Gaussian error function

$$\mathrm{erf}(x) = (2/\sqrt{\pi}) \int_0^x dy\, e^{-y^2}. \tag{5.32}$$

The whole separable solution, exact at $t \to \infty$, $K \to \infty$, reads

$$\zeta(x,t) = 2\sqrt{Pt}\, \mathrm{erf}^{-1}(1 - 4|x|/\lambda_s)\ ,\ -\frac{\lambda_s}{2} < x < \frac{\lambda_s}{2}, \tag{5.33}$$

where the wavelength λ_s is arbitrary. At the maxima and minima $x_0 = 0, \pm\lambda_s/2$ the profile diverges as $\zeta \sim \pm\sqrt{\ln(1/|x - x_0|)}$

As it turns out, neither of the analytic solutions presented here is the whole solution to the problem. To gain more insight the step equation must be integrated numerically. To ensure the stability of the integration a fully implicit Euler scheme was employed [75]. The integration time step was continuously adjusted during the calculation to

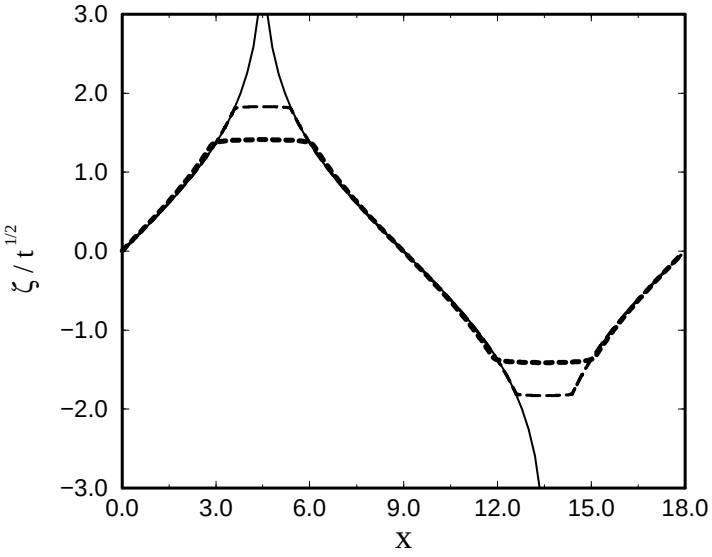

Figure 5.5: The asymptotic form of the scaled profile $\zeta/\sqrt{t}$ for Eq.(5.19) (long dashes) and Eq.(5.22) with $n = 1/2$ (short dashes). Full line is the separable solution (5.31) with λ_s equal to the total meander wavelength $\lambda_s = 18\sqrt{Q_n/P} \approx 2\lambda_u$.

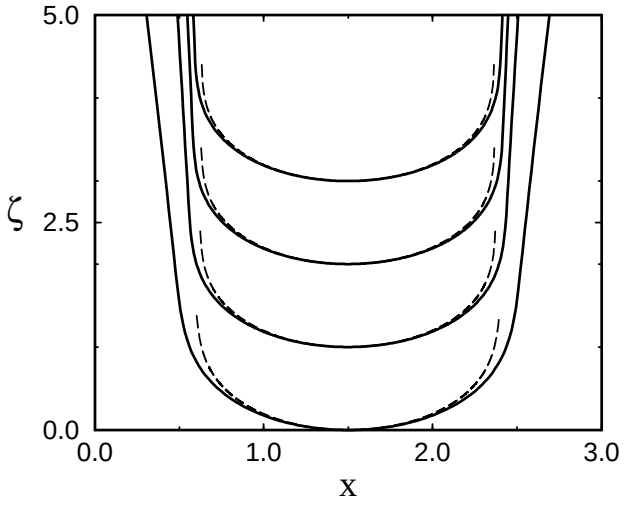

Figure 5.6: The shape of the extremal region in the step profile resulting from Eq.(5.19) at $t = 500, 1500, 2500, 3400$. The dashed lines are the stationary solutions corresponding to the maximum slope in the profile.

improve numerical efficiency, without loss in the accuracy. Moreover, the scheme was implemented on an adaptive spatial grid to ensure sufficient spatial resolution of the profile.

The profiles for both cases $n = 1$ and $n = 1/2$ obtained from the numerical integration are shown in Fig. 5.4. The initial configuration was a flat profile with small random perturbations. At the beginning the profile develops a wave pattern with a wavelength $\lambda_{BZ} = 2\pi\sqrt{Q_n/P}$, as anticipated on the basis of linear analysis of Eq. (5.19).

Further evolution of the profile leaves this wavelength unchanged and only the shape and the amplitude of the profile change, as seen in Figs. 5.4. The amplitude grows like $\sim \sqrt{t}$, as predicted by the separable solution (5.33). Also the shape of the scaled profile $\zeta/\sqrt{t}$ agrees with the separable solution at the sides of the wave pattern, as seen in Fig.5.5, showing the scaled profile. Near the maxima and minima however, the shape of the profile deviates from the separable solution. This is reasonable since the curvature of the separable profile would diverge at the extremal values, and the relaxation term in Eq. (5.19) is definitely not negligible at these points.

The shape near extremal points is that of the stationary profile (5.29). This is not so surprising if one notes that the current in the parts of the profile described by the separable ansatz behaves as $J \sim (\partial_x \zeta)^{-1}$. Thus asymptotically as $\partial_x \zeta \to \infty$ also the current in the separable solution goes to zero and it can be matched to the station-

ary solution [24]. Since the slope of the separable profile diverges asymptotically, the maximal slope in the stationary solution, which can be joined to it also diverges, corresponding to parameter value $M_0 = 1$. This also sets the wavelength of the stationary profile *i.e.* the width of the extremal region. It may be concluded that the profile approaches a shape, where in the vicinity of extremal values $-\Lambda(1)/2 < x < \Lambda(1)/2$ the form is that of the stationary solution, forming "caps" to the profile. Outside the interval the profile acquires the shape of the separable solution. The profile should approach this limiting shape as $t^{-1/2}$ [32], since the slope of the separable solution at the junction grows as $\partial_x \zeta \sim t^{1/2}$. Fig. 5.6 shows a comparison of the numerically integrated profile and the stationary solution. Since the amplitude of the separable solution grows slower than $\sim t^{1/2}$ it appears flat in the scaled profile.

5.2.3 Persistence of the initial wavelength

The final point to be clarified is the question of the persistence of an initially chosen wavelength. It was seen in previous section the the profile spontaneously chooses the linearly most unstable mode λ_{BZ}. It is imaginable that also some other external mechanism would set the initial length scale. Indeed, in the case of step flow growth starting with atomistically flat steps, the initial scale should be set by the ***nucleation length*** L_D, *i.e.* the average distance between dimers that are nucleated at the beginning along the step edge as the deposition starts.

Based on their experimental findings, Maroutian *et al.* [51, 52] suggested that the wavelength seen in the experiments is actually the nucleation length. They observed that on a Cu surface, vicinal to Cu(100), the meandering instability occurred, but the wavelength was much larger than $\lambda = \lambda_{BZ}$. Moreover, the wavelength showed dependence on the temperature that deviated from the BZ-theory [51, 52].

To study the persistence of the initially set wavelength, the step equation (5.19) was integrated numerically, starting with a sinusoidal profile. Whenever $\lambda_{init} > \lambda_c = 2\pi\sqrt{(Q_n/P)}$, the profile is unstable and grows in amplitude. Also an asymptotic solution, consisting of joined pieces of the separable and stationary profile can be constructed for arbitrary wavelengths λ. However, it turns out that if the initial wavelength exceeds the critical value by a factor of 3, $\lambda_{init} > 3\lambda_c$, so that an additional meander fits between the subsequent minima and maxima, an extra meander is spontaneously created and the wavelength decreases [32], as shown in Fig. 5.7. Thus only a band of width $\lambda_c \leq \lambda \leq 3\lambda_c$ of wave profiles are allowed by the evolution equation (5.19). This result must be interpreted with caution; obviously changing the wavelength is a process involving multiple steps. In the description presented here it is implicitly assumed that all steps are in phase. Creating new meanders coherently on many steps simultaneously may well be much more difficult than suggested by the analysis presented here.

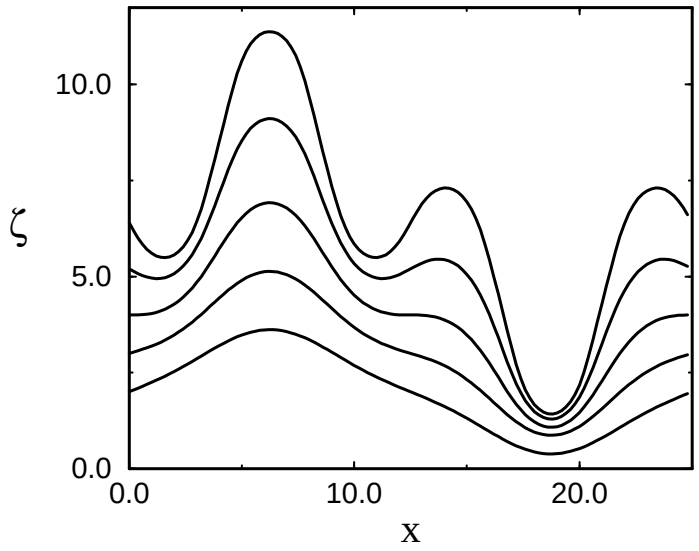

Figure 5.7: Spontaneous creation of an extra meander period for the case of step-edge diffusion ($n = 1/2$). The initial wavelength of the profile is $\lambda_i = 25\sqrt{Q_n/P} > 3\lambda_c$. Again the spatial variable x has been scaled by $\lambda_c/2\pi = \sqrt{Q_n/P}$ and time by Q_n/P^2.

5.2.4 Generalized step equation

It was seen in the previous section that the equations describing step motion with relaxation through step diffusion or mass transport over terraces can be treated equally. These results are easily generalized for equations of the form Eq. (5.22) with an arbitrary n. The separable solution (5.31) is exact when the relaxation term is neglected. Hence it is asymptotically valid when $n > -1/2$, for $n \leq -1/2$ the relaxation term may never be neglected. The stationary solution has qualitatively different features for different values of n.

In the interval $1/2 < n < 3/2$ the behavior is analogous to the case $n = 1$; the wavelength $\Lambda(M_0)$, *i.e* the size of the cap at the maxima and minima, is a decreasing function of the parameter M_0 (corresponding to the maximal slope) and the limiting value $S = \max_x[\partial_x \zeta] \to \infty$, *i.e.* $M_0 \to 1$ is [32]

$$\Lambda(1) = \sqrt{2\pi(3-2n)(Q_n/P)}\frac{\Gamma[(2n+1)/4]}{\Gamma[(2n+3)/4]}. \tag{5.34}$$

Also the amplitude $\mathcal{A}(M_0)$ remains finite, limiting value being

$$\mathcal{A}(1) = \sqrt{\frac{Q_n}{P}}\frac{\sqrt{8(3-2n)}}{2n-1}. \tag{5.35}$$

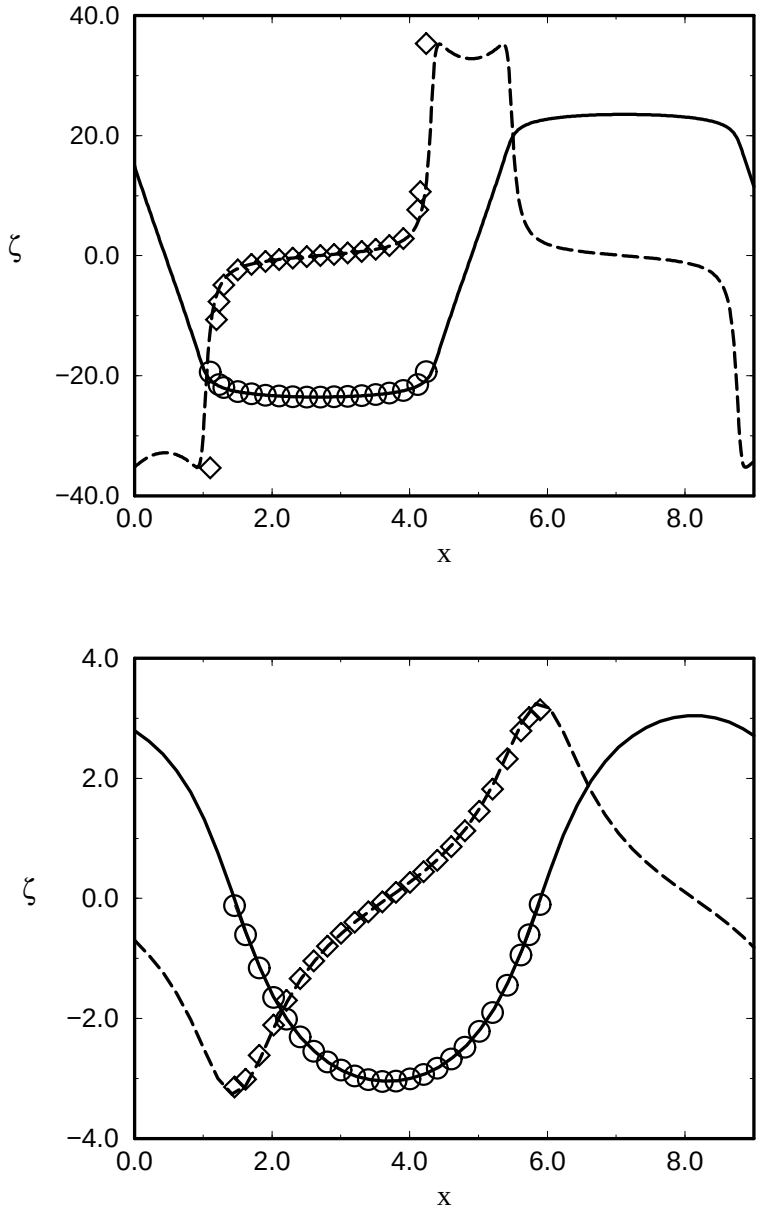

Figure 5.8: Asymptotic form of the step profile for $n = 1/2$ (upper) and $n = 0$ (lower). Full line is the profile and dashed line the slope ζ_x. Circles represent the stationary solution and diamonds the corresponding slope. The separable solution, still present in the sloped regions of the profile for $n = 1/2$, has vanished for $n = 0$.

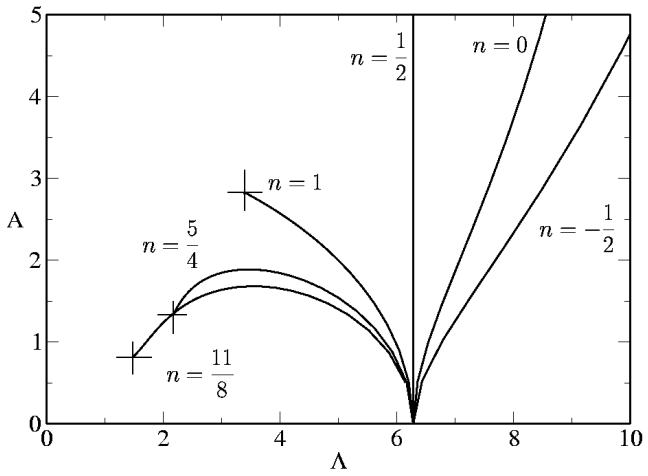

Figure 5.9: The amplitude of the stationary profile versus the wavelength. As the maximal slope S in the profile, set by the slope of the separable solution (5.33), increases the amplitude and the wavelength follow the curves, starting from point $\Lambda = \lambda_c, \mathcal{A} = 0$. The amplitude diverges as $S \to \infty$ ($M_0 \to 1$) for $n \leq 1/2$, and the maximal wavelength remains finite for $-1/2 < n < 3/2$. The limiting values of $\mathcal{A}$ and Λ, marked with + in the figure, follow from Eqs. (5.35) and (5.34). For $n \geq 3/2$ the curve ends at point $\Lambda = 0, \mathcal{A} = 0$. The wavelength has been scaled by $\lambda_c/2\pi$ and the amplitude is left unscaled.

The correspondence between the amplitude $\mathcal{A}$ and the wavelength Λ for different values of M_0 is plotted in Fig. 5.9. The evolution of the profile is then similar to the profile of $n = 1$ case; the regions in the step profile far from the maxima and minima evolve according to the separable solution (5.33) and the slope grows as $\sim \sqrt{t}$. Consequently also the maximal slope in the stationary solution, which is set by the slope in the separable solution, grows and the wavelength and the amplitude of the of the stationary solution change. The dependence of the amplitude on the wavelength for all values of M_0 is plotted in Fig. 5.9. As M_0 increases (*i.e* S increases) the amplitude and the wavelength follow the curves in Fig. 5.9, starting from the point $\Lambda = \lambda_c, \mathcal{A} = 0$, which corresponds to $M_0 = 0$. Asymptotically $M_0 \to 1$ ($S \to \infty$) and the limiting values $\mathcal{A}(1)$ and $\Lambda(1)$ are finite and decreasing with increasing n.

As $n \to 3/2$ the limiting value of the cap length goes to zero, as well as the limiting amplitude. Therefore for $n > 3/2$ true spike singularities are expected to develop at the extremal points of the profile. Since the maximal slope of the separable solution, which selects the relevant stationary solution, diverges as $S \sim \sqrt{t}$, the curvature at the

maxima and minima goes as $\sim t^{(2n-3)/4}$.

As already noted before, for $n = 1/2$ the cap length $\Lambda/2$ is independent of the parameter M_0 and thus the plot $\mathcal{A}$ vs. Λ is a vertical line. From (5.29) one finds that the amplitude diverges as $\mathcal{A}(M_0 \to 1) \sim -\ln(1 - M_0)$, which in terms of the slope translates to $\mathcal{A}(S) \sim \ln(S)$ as $S \to \infty$. The separable profile scales in time as $\zeta \sim t^{1/2}$ and $\mathcal{A} \sim \ln(t)$. This indicates that the caps appear as flat pieces in the scaled profile $\zeta/\sqrt{t}$. In the parameter regime $-1/2 < n < 1/2$ it is found from (5.29) that the amplitude behaves like $\mathcal{A} \sim S^{1/2-n} \sim t^{1/4-n/2}$ and thus in the scaled profile $\zeta/\sqrt{t}$ the caps are still flat facets. The lateral cap size $\Lambda/2$ remains finite for all M_0 when $n \geq -1/2$.

A quantitative change occurs when $n = n_c \approx 0.2283$, as the maximal wavelength of the stationary profile Λ exceeds the linearly most unstable wavelength. For $n < n_c$ the asymptotic solution is totally described by the stationary solution and the separable profile becomes irrelevant, as illustrated in Fig.5.8. When $-1/2 < n < n_c$ the asymptotic wavelength $\Lambda(1)$ (5.34) is still finite and the profile evolves toward this finite value. Finally at $n = -1/2$ the stationary wavelength diverges as $M_0 \to 1$ and the profile coarsens indefinitely, similarly as described for one dimensional surfaces in Ref. [73].

5.3 Kink Ehrlich-Schwoebel effect (KESE)

The step meandering during step flow growth can also result from a very different origin. It was noted independently by Pierre-Louis *et al.* [63] and Ramana-Murty *et al.* [56], that an additional barrier experienced by adatoms diffusing along the steps when rounding corners (See Fig. 4.1), as discussed in previous Chapter 4.3.1, leads to meandering of steps. This is easy to understand as an analogy to the mounding instability on singular surfaces, where the Ehrlich-Schwoebel effect causes an up-hill surface current destabilizing the surface. The kink-rounding barrier induces a non-equilibrium current J_{step} along the steps in the up-kink direction, just as the Ehrlich-Schwoebel barrier causes an up-hill current, causing mounds to from on the steps, thus the name kink-Ehrlich-Schwoebel effect (KESE) [63]. Since the mounds are created on each step independently, the steps start to meander without any phase correlation. The effective step repulsion, meditated over the diffusion field, drives the meander to the in-phase mode during further growth.

5.3.1 Relevant length scales

To keep the notation transparent, all lengths relevant to the step edge dynamics are noted with capital L and the terrace lengths with ℓ. The origin of the KESE instability lies in the dynamics of the adatoms along the step edges, so it is necessary

to consider the dynamics in detail on a microscopic level. The atoms deposited on the terraces eventually arrive to the step edges, along which they migrate until they meet a kink site, where they are incorporated, or meet an another atom diffusing along the edge (here dimers will be assumed to stable objects which do not break up on the time scale of the growth).

Assuming dimers stable, the mean distance between two nucleation centers along the step edge can be calculated by following the argumentation of Politi and Villain [69], adapted to the edge diffusion. To this end one calculates the mean number of nucleation events on a straight step segment of length L, limited by kink sites at both ends. For simplicity the dynamics at the kinks will be here assumed independent of the kink type (up- or down- kink). If the arrival rate of new adatoms per unit length [4] to the step is denoted with Φ, then the rate of arrival of new atoms to a step segment of length L is $(L/a)\Phi$. The rate of nucleation of dimers on the step segment is given by the product of $(L/a)\Phi$, the size of the area covered by the random walk conducted by the atom at the step L_{RW} and and the mean concentration of atoms at the step $\langle c \rangle$. The mean number of nucleation events $\bar{N}$ on a segment of length L in time interval Δt is then

$$\bar{N}(L) = \Phi(L/a) L_{RW} \langle c \rangle \Delta t. \tag{5.36}$$

The mean concentration $\langle c \rangle$ can be calculated from 1D BCF theory. The mean distance follows from (5.36) by arguing that on a segment of the size of the nucleation length L_D, one nucleation event occurs $\bar{N}(L_D) \approx 1$, during the time it takes to move the step one lattice constant forwards [5], *i.e.* the time it takes for the kinks to move distance L_D.

If the adatoms are attached to the steps irreversibly (again in the time scale relevant for the growth) the situation is completely analogous to the sub-monolayer growth on singular 1D surfaces and the results may be directly taken over [69]. The flux to the step is $\Phi = aF\ell$, where F is the deposition flux and ℓ the step distance. The area covered by diffusing step atoms is the kink distance $L_{RW} \sim L_D$. The concentration of step atoms follows from the 1D BCF theory as $\langle c \rangle = F\ell L^2/(12 D_s)$, where D_s is the diffusion coefficient on a flat step and $\Delta t = (aF\ell)^{-1}$. Putting everything together leads to the expression for the nucleation length

$$L_D = \left(\frac{12 D_s a}{F\ell} \right)^{1/4} \tag{5.37}$$

At higher temperatures the adatoms may also detach from the steps. In analogy with the 1D surfaces this would imply that the desorption plays an important role. For step edge nucleation the situation is bit more complicated, since there is no real

[4] *i.e.* the "deposition flux" on a 1D surface

[5] In the analogy with 1D surfaces this translates to deposition of one monolayer [69]

desorption from the surface, but the atoms only return to the terrace and are attached to the steps later at some other site. This effect enhances the effective flux to the steps. The effective flux can be determined by comparing the step velocity imposed by the requirement of no desorption from the surface as a whole and the velocity of kinks along the steps. The absence of desorption sets the step velocity to value $v_{st} = \Omega F \ell$. If adatoms diffuse along the steps on the average a distance x_s before being detached again, the kinks receive atoms from area of size x_s around them, implying a kink velocity $v_{kink} = \Phi x_s$. In order to move the step one lattice constant forwards the kinks must move a distance L_D. Now we have two expressions for the time Δt needed to move the step one lattice constant

$$\begin{aligned} \Delta t &= \frac{a}{v_{st}} = \frac{L_D}{\Phi x_s} \\ \Longrightarrow \Phi &= \frac{L_D}{a x_s} \Omega \ell F \ > a F \ell \ \text{ if } \ L_D > x_s. \end{aligned} \tag{5.38}$$

Now the area covered by atoms diffusing along the steps is $L_{RW} = x_s$ and, assuming that the detachment from the steps dominates over the capture of atoms by the kinks $x_s \ll L_D$, the average concentration follows from balancing the mass current to the step Φ and detachment from the step $\langle c \rangle / \tau$, where $\tau = x_s^2 / D_s$ is the average time an atom diffuses along the step before detachment. Inserting this into Eq. (5.36) and requiring $\bar{N}(L_D) = 1$ results to an expression for the nucleation length as

$$L_D = a \left(\frac{D_s}{F \ell x_s \Omega} \right)^{1/3}. \tag{5.39}$$

The crossover takes place when both expressions are equal, yielding a crossover value for the detachment length x_s

$$x_s^{co} \equiv \frac{1}{12^{3/4}} \left(\frac{D_s}{F \ell a} \right)^{1/4}. \tag{5.40}$$

A simple formula interpolating between the results and yielding correct expressions on both limits $x_s \gg x_s^{co}$ and $x_s \ll x_s^{co}$ is easily obtained as

$$L_D = \left(\frac{12 D_s a}{F \ell} \right)^{1/4} \left[1 + \left(\frac{x_s^{co}}{x_s} \right)^{1/3} \right]. \tag{5.41}$$

Along flat steps the mean kink separation is of the order of L_D. This is to be compared with the other kink distances, namely the thermal kink distance and the separation imposed by the large scale orientation of the step. The steps are one dimensional objects and therefore rough in all finite temperatures. The thermal kink distance

follows a Boltzmann distribution and the length scale is $L_K = (a/2)\exp(\beta E_K)$, where E_K is again the energy cost of creating a kink (See sect. 3.2). The orientation of the step implies that the mean kink separation is $L_{or} = a(\tan(\Theta))^{-1}$, where Θ is the angle between the mean step orientation and the nearest high symmetry orientation. When either of the length scales L_k or L_{or} is smaller than the nucleation length L_D, most step adatoms are incorporated to the crystal at these kinks and nucleation events are irrelevant. However, on high symmetry oriented steps at low temperatures $L_D < L_K$ the step motion is analogous to the layer-by-layer growth of singular surfaces, subjected to mounding instability just as the singular surfaces [71].

5.3.2 Non-equilibrium step current

To see how deposition flux destabilizes high-symmetry oriented steps one must calculate the mass current along the steps [6]. To calculate the adatom current along the steps the analogy between 1D surfaces and steps may be employed again. The BCF equations (see Sect. 3.3) for step adatoms read [7]

$$\begin{aligned} D_s\partial_x^2 c(x) &+ \frac{\Phi}{a} - c/\tau = 0 \\ D_s\partial_x c(0) &= k_-\left[c(0) - c_{eq}\right] \\ D_s\partial_x c(L) &= -k_+\left[c(L) - c_{eq}\right], \end{aligned} \tag{5.42}$$

where $c(x)$ is the adatom concentration on the flat step segment limited by two kinks at $x = 0$and $x = L$. D_s is the step diffusion coefficient, τ the average time an adatom diffuses along the step before detachment and $k_\pm$ are the attachment rates to the kinks at $x = 0, L$, depending on the type of the kinks. The situation is clarified in Fig. 5.10. Since there is no desorption from the terraces adatoms that are detached from the steps must re-attach later. This adds up to the deposition of new adatoms from the beam $\Phi/a = F\ell + c_{eq}/\tau$, where ℓ is the width of the terrace; the deposition rate to the step due to the deposition beam is $aF\ell$. c_{eq}/τ is the arrival rate of adatoms due to non-zero equilibrium adatom concentration on the terrace, counter balancing the detachment from steps when the deposition beam is turned of.

From equations (5.42) one can calculate the average current of adatoms along the step segment

$$J(L) = \frac{1}{L}\int_0^L j(x)\mathrm{d}x = \frac{1}{L}\int_0^L \left[-D_s\partial_x c(x)\right]\mathrm{d}x \tag{5.43}$$

[6] For simplicity the description here is limited to simple cubic crystals, and the surface has a four-fold symmetry. Flat steps then mean [100] oriented segments.

[7] Here Φ is the deposition *rate* $[\Phi] = s^{-1}$ instead of flux. The deposition flux $F = \Phi/a$.

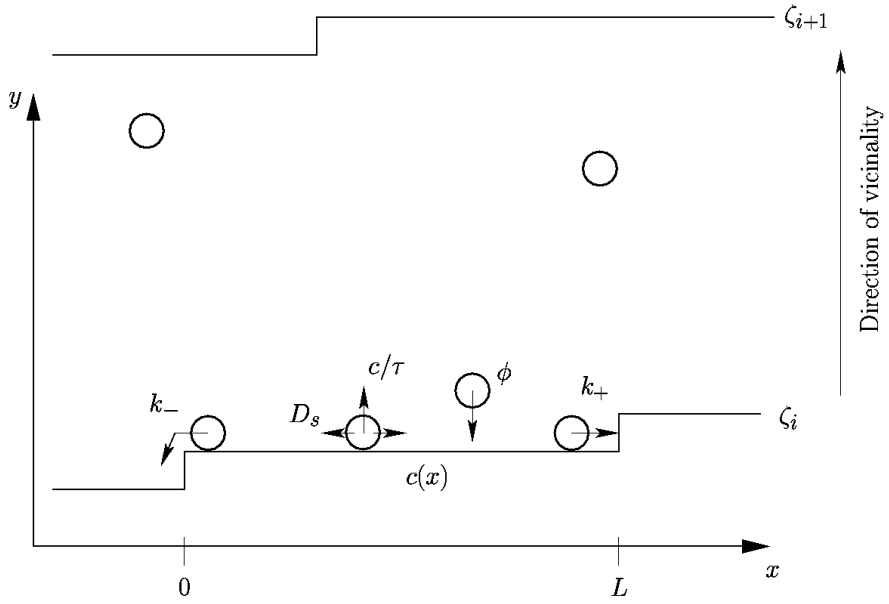

Figure 5.10: The 1D BCF theory can be applied to atomic steps. The geometry and notation used in the text is illustrated here.

yielding an expression

$$J(L) = \frac{D_s x_s[(\Phi/a)\tau - c_{eq}]}{L} \frac{(L_- - L_+)[\cosh(L/x_s) - 1]}{x_s \cosh(L/x_s)(L_+ + L_-) + \sinh(L/x_s)(L_+ L_- + x_s^2)}, \tag{5.44}$$

where $x_s = \sqrt{D_s \tau}$ and $L_\pm = D_s/k_\pm$ are length scales introduced by the attachment coefficients. From Eq. (5.44) one sees immediately that the current vanishes if the attachment kinetics at the kinks are equally fast $L_+ = L_-$. Thus a current can only arise if the kinks are of different types and there is an additional barrier E_{kr} for attaching to a kink from above *i.e.* going around a kink, as discussed in Sect. 4.3.1. Let us now assume that both of the kinks are positive, as in Fig. 5.10, and that attachment to a kink from below occurs with a rate D_s/a ($L_+ = a$), and from above $(D_s/a)\exp(-\beta E_{kr})$ ($L_- = a\exp(\beta E_{kr})$). The expression (5.44) simplifies in the limit of no detachment from the step $x_s \gg L$ to form

$$J(L) = \frac{F\ell L}{2} \frac{L_{kes}}{L_{kes} + L + 2a}, \tag{5.45}$$

where the *Kink Ehrlich-Schwoebel length* [8] $L_{kes} \equiv L_- - a$ has been introduced. In the

[8] The advantage of this definition is that $L_{kes} \to 0$ as $E_{kr} \to 0$. Sometimes a definition $L_{kes} \equiv L_-$ is used.

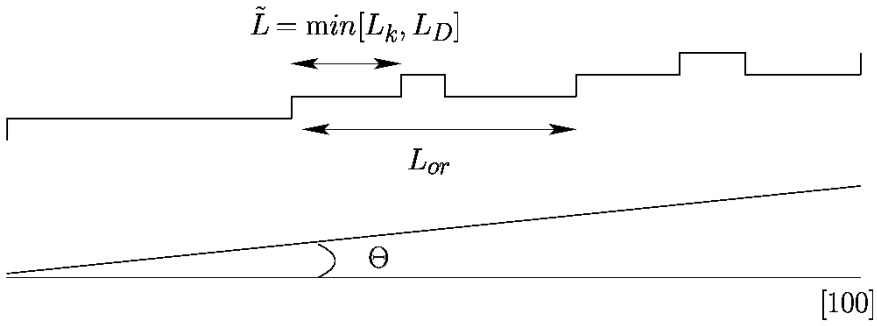

Figure 5.11: Geometry of a step oriented near [100] direction. In addition to array of kinks due to the orientation (L_{or}), kinks originate also from thermal fluctuations (L_k) and nucleation on the step during deposition (L_D). Relevant kink distance is the smallest of L_D, L_k, L_{or}.

opposite limit, fast detachment $x_s \ll L$ the current reads

$$J(L) = \frac{F\ell x_s^3}{L} \frac{L_{kes}}{L_{kes}(x_s + a) + (x_s + a)^2}, \tag{5.46}$$

When applying the expression for the step current, it should be noted that arbitrarily long flat segments cannot occur. There will be either thermally exited kinks at interval L_k or kinks due to nucleation with a mean separation L_D. A step with a mean orientation Θ will then have kinks at distance

$$\tilde{L} = \min[L_k, L_D, L_{or}], \tag{5.47}$$

where $L_{or} = a \tan^{-1}(\Theta)$ is the kink distance imposed by the orientation. Clearly kinks created thermally or by nucleation do not contribute to the current $J(L)$ since they do not have preferred sign; only the excess of kinks of the same sign, imposed by the average orientation contribute to the average current [37]

$$J_{st} = J(\tilde{L}) \left(\frac{\tilde{L}}{L_{or}} \right). \tag{5.48}$$

To study the stability of high symmetry oriented steps it is useful to write down an equation of motion for the step profile. Choosing the [100] orientation as the $y = 0$ axis the step position in y-direction is described by the function $\zeta(x, t)$. The kink distance

due to step orientation is $L_{or} = a(\partial_x \zeta)^{-1}$. Thus the non-equilibrium current for step orientations near to [100] , $L_{or} \gg L_k, L_D$ reads

$$J_{st}(x) = J(\tilde{L}) \frac{\tilde{L}}{a} (\partial_x \zeta). \tag{5.49}$$

The current is in the up-hill direction and thus has destabilizing character [37].

It should be noted that the expression (5.44) is not applicable for all step directions. To justify the use of the BCF theory the kink distance L must be larger than the lattice constant $L \gg a$. Otherwise a microscopic description of the adatom dynamics along the steps is needed. Indeed, it is clear that the current should vanish for the [110] orientation, where the kink distance due to orientation is $L_{or} = a$ by symmetry. Here it is implicitly assumed that the orientation is near the [100] direction so that the kink distance is large and multiple height kinks may be neglected. The main interest in this work is on the stability of high symmetry steps and this assumption is justified. Phenomenological expressions for the current with zeros at [110] (*i.e.* $\partial_x \zeta = 1$) have also been proposed [71]. Also expressions for the step current for steps with arbitrary orientation may be found in the literature [63].

5.3.3 Wavelength of the KESE instability

According to the reasoning in the previous section, deposition induces a current along the steps in the up-kink direction. This leads to destabilization of flat steps oriented along the high symmetry direction, just as the ES barrier destabilizes singular surfaces against mound formation. To study the evolution of such steps it is informative to write down an equation of motion including the step current. A good starting point is the step equation derived in sect. 5.2. The equation is of the form

$$\partial_t \zeta = -\Omega \partial_x \left(J_{terr} + J_{st} \right) + \mathcal{G}(\zeta), \tag{5.50}$$

where J_{terr} is the term from the step equation (5.19), arising from the non-homogeneous distribution of deposited atoms along the step, as discussed in Sect. 5.1.1

$$J_{terr} = \frac{F\ell^2}{2} \frac{\partial_x \zeta}{1 + (\partial_x \zeta)^2}, \tag{5.51}$$

J_{st} is the current due to adatom dynamics along the step, from the previous section and the last term $\mathcal{G}(\zeta)$ describes the relaxation of the steps.

The relaxation term deserves a closer inspection. It has contributions from the mass transport along the step and via terrace diffusion due to spatially varying chemical potential, just as discussed in Sect. 5.2

$$\mathcal{G}(\zeta) \sim -\Omega \, \partial_x \left(\frac{\beta D \ell c_{eq}}{\sqrt{1 + (\partial_x \zeta)^2}} + \sigma \right) \partial_s \left(\Omega \tilde{\gamma} \kappa \right) \tag{5.52}$$

where $\Omega\tilde{\gamma}\kappa$ is the step chemical potential composed of step stiffness and curvature, and σ is the adatom mobility along the steps (4.34). D is the terrace diffusion coefficient, c_{eq}^0 the equilibrium adatom concentration on terraces and Ω the atomic area.

Politi and Villain [74] have proposed an additional term, arising from the random nature of nucleation on flat step segments. In studies of growth on singular 1D surfaces they noticed, that there is a wavelength selection at the beginning of ES instability, even in the absence of a relaxation current [74]. A finite wavelength arises from competition between the destabilizing ES current and some relaxation mechanism. Based on dimensional analysis of the problem they proposed a relaxation term due to the random nature of nucleation on terraces, having the form $\sim K\partial_x^4\zeta$ in the linear regime $\partial_x\zeta \ll 1$ [71, 74], where $K \sim \Phi\ell_D^4$. Here ℓ_D is the nucleation length on a 1D singular surface. This relaxation term obviously plays a role only if the average kink distance is larger than the nucleation length, otherwise the nucleation does not take place on the surface.

Putting everything together the evolution equation for a step in the linear regime, $\partial_x\zeta \ll 1$, reads

$$\partial_t\zeta = -\underbrace{\left(\frac{\Omega F\ell^2}{2} + \Omega J(\tilde{L})\frac{\tilde{L}}{a}\right)}_{\equiv\nu}\partial_x^2\zeta - \underbrace{\left[\Omega^2\tilde{\gamma}\left(D\ell c_{eq}^0\beta + \sigma\right) + \alpha\Phi L_D^4\right]}_{\equiv K}\partial_x^4\zeta, \tag{5.53}$$

where α is a numerical constant, which is evaluated later. Inserting a Fourier decomposition of the profile $\zeta(x,t)$ into Eq. (5.53), one finds that modes with a wavelength

$$\lambda > \lambda_c \equiv 2\pi\sqrt{\frac{K}{\nu}} \tag{5.54}$$

grow exponentially and the fastest growing mode is $\lambda_u = \sqrt{2}\lambda_c$. To make more sense out of this result it is necessary to consider various limits. This opens up a possibility of numerous expressions for the most unstable wavelength, depending on the ordering of the lengths L_k, L_D, x_s, L_{kes}.

To make predictions about the shape of the step profile and evolution beyond the initial stage a non-linear step equation, similar to (5.19), would be needed. However deriving such an equation is difficult as the relaxation mechanism due to random nucleation along the steps is not known. Therefore there is no knowledge how this term appears in a non-linear equation [61]. Further discussion about non-linear terms in such an equation may be found in recent articles [63, 78]

No step edge diffusion

Let us first study the limit of no step diffusion. Absence of adatom diffusion along the steps implies $\sigma, D_s \equiv 0$ and consequently $L_D = 0$. The wavelength of the instability

follows in this limit as

$$\lambda_u = 4\pi \left(\frac{\Omega \beta D c_{eq}^0 \tilde{\gamma}}{F\ell} \right)^{1/2} \tag{5.55}$$

In this case the destabilizing effect is the non-uniform distribution of deposited atoms on the steps and the relaxation takes place via terrace diffusion, *i.e.* this is the Bales-Zangwill instability. This scenario was already discussed extensively earlier in this chapter.

No detachment from the steps

Taking the limit $x_s \to \infty$ implies the condition of no detachment from the steps. The coefficients then acquire the form

$$\nu = \frac{F\ell}{2} \left(\Omega\ell + \frac{a\tilde{L}^2 L_{kes}}{\tilde{L} + L_{kes} + 2a} \right) \ , \ K = \Omega^2 \sigma \tilde{\gamma} + \alpha \Phi L_D^4, \tag{5.56}$$

where the arrival rate is now $\Phi = \Omega F \ell$. If there is no extra barrier for going around the kinks, The kink-Ehrlich-Schwoebel length is $L_{kes} = 0$ and the Bales-Zangwill instability is discovered again, only with a different relaxation term. When kink rounding is suppressed and $L_{kes}\tilde{L} \gg a\ell$ the first term in the coefficient ν in (5.56) may be neglected. The wavelength now depends on the ratio of the lengths $\tilde{L}/L_{kes}$.

The case of strong kink rounding barrier $L_{kes} \gg \tilde{L}$ is clear cut. In this case the relaxation via step diffusion is also irrelevant [9]. Now the relevant wavelength reads

$$\lambda_u = 4\pi \frac{L_D^2}{\tilde{L}} \sqrt{\alpha}. \tag{5.57}$$

On thermally flat steps, meaning that the thermal kink distance is long, $L_D < L_k$, and in the absence of mass transport around kinks, the only possibility for the meander length is the nucleation length L_D [37, 71]. For Eq. (5.57) thermally flat steps imply that the typical kink distance is the nucleation length $\tilde{L} = L_D$ and consequently $\lambda_u = 4\pi\sqrt{\alpha} L_D$. Now consistency requires $\alpha = (4\pi)^{-2}$. This supports the existence of the relaxation mechanism due to stochastic dimer nucleation; it may be argued that since in the case of no mass transport around kinks the wavelength has to be the nucleation length, for consistency, there should be a relaxation term of the form $\alpha\Phi L_D^4$ in the step equation [38]. However, it is not obvious that the evolution of an atomistically flat step can be described with a simple equation of the from (5.53), and this result should be interpreted with care.

[9] As was seen in Sect. 4.3.1, Eq. (4.34), the adatom mobility goes to zero $\sigma \to 0$ for strong kink rounding barriers.

In the other limit $\tilde{L} \gg L_{kes}$ (still assuming $L_{kes}\tilde{L} \gg \ell$), the expression for the instability wavelength reduces to

$$\lambda_u = 4\pi \left(\frac{\alpha \Phi L_D^4 + \Omega^2 \sigma \tilde{\gamma}}{F \ell a \tilde{L} L_{kes}} \right)^{1/2} . \tag{5.58}$$

In order to find out the dependence of the wavelength on the experimental parameters, such as deposition flux F and temperature T, one needs also to know which of the lengths L_k and L_D is smaller.

Fast detachment from the steps

In this limit $x_s \ll \tilde{L}$, meaning that only adatoms landing on the step within a distance x_s from the kink reach the kink before detachment. The coefficients now reduce to

$$\nu = F\ell \left(\frac{\Omega \ell}{2} + \frac{a x_s^3 L_{kes}}{L_{kes}(x_s + a) + (x_s + a)^2} \right) \ , \ K = \Omega^2 D \ell c_{eq}^0 \beta \tilde{\gamma} + \alpha \Phi L_D^4, \tag{5.59}$$

and the arrival rate is given by $\Phi = (L_D/x_s) a F \ell$. The relaxation term due to the step edge diffusion is neglected as it is assumed to be irrelevant against the terrace diffusion.

The expressions can be simplified further by considering limits of strong $L_{kes} \gg x_s$ and weak $L_{kes} \ll x_s$ kink rounding barriers. For strong kink barrier the wavelength reads

$$\lambda_u = 4\pi \left(\frac{\alpha \Phi L_D^4 + \Omega^2 D \ell c_{eq}^0 \beta \tilde{\gamma}}{F \ell (\Omega \ell + 2 a x_s^2)} \right)^{1/2} . \tag{5.60}$$

And the opposite case $L_{kes} \ll x_s$ leads to the expression

$$\lambda_u = 4\pi \left(\frac{\alpha \Phi L_D^4 + \Omega^2 D \ell c_{eq}^0 \beta \tilde{\gamma}}{F \ell (\Omega \ell + 2 a x_s L_{kes})} \right)^{1/2} . \tag{5.61}$$

Further reduction of these formulae is not easy since it is not clear which of the relaxation terms is dominating. The relaxation term arising from the random nucleation should be treated very cautiously as the mechanism is not well understood and thus it is easy to draw false conclusions.

5.3.4 Possibility of stable step-flow

It is well known that the ES barriers stabilize the step-flow growth in the direction of the vicinality [82]. This owes to the fact that fluctuations in the inter step-distance are damped. Intuitively the mechanism is clear; due to the ES barrier the velocity of the step depends primarily on the width of the terrace *in front* of it. Therefore a step

that is lagging behind its average position will have a larger terrace in front and will speed up. For advancing steps the opposite it true. The same scenario also applies to the kinks on a step. A step that is not oriented along the [100] axis, but close to it, is analogous to a 1D vicinal surface.

Let us now assume that a step has a mean kink distance due to its orientation that is smaller than the kink- or nucleation lengths, $L_{or} < L_k, L_D$. Taking again the [100] direction as the x-axis the step position is $\zeta(x,t) = mx + \epsilon(x,t)$, where m is the average slope of the step relative to the x-axis and is related to the kink distance by $m = a/L_{or}$. Here $\epsilon(x,t)$ describes the deformation of the step around its mean position. To study stability of the step morphology, it is sufficient to determine the properties of ϵ. The condition $L_{or} < L_k, L_D$ implies that most kinks have the same sign. Consequently the step current now has expressions (5.45) and (5.46) instead of the linear dependence on the slope ($\partial_x \zeta$) of Eq. (5.48), which results for small slopes (relative to the [100] direction).

Inserting the expression $L/a = (m + \partial_x \epsilon)^{-1}$ into the current (5.45) and expanding the expression to the first order in $\partial_x \epsilon$ gives

$$J(m) \approx \frac{F\ell a}{2} \left[\frac{L_{kes}}{L_{kes} m + a} - \left(\frac{L_{kes}}{L_{kes} m + a} \right)^2 \partial_x \epsilon \right]. \tag{5.62}$$

The destabilizing effect due to the BZ mechanism is independent of the average orientation of the step and thus reads simply

$$J_{terr} = \frac{F\ell^2}{2} \frac{\partial_x \epsilon}{1 + (\partial_x \epsilon)^2}. \tag{5.63}$$

Putting these two terms together, the linearized equation for $\epsilon(x,t)$ has the same form as Eq. (5.53). The coefficient in front of the second order term reads

$$\nu = \frac{\Omega F \ell^2}{2} - \frac{\Omega F \ell a}{2} \left(\frac{L_{kes}}{L_{kes} m + 1} \right)^2. \tag{5.64}$$

The coefficient changes sign at $m_0 = \sqrt{a/\ell} - a/L_{kes}$ indicating that for $m \leq m_0$ the steps are ***stable*** against meandering. This is of course a consequence of the stabilization of the kink separation due to kink rounding barriers, equivalent to the stabilization of the step distance on the vicinal surfaces. The requirement $m \leq m_0$ implies

$$L_{or} \geq \frac{L_{kes} \sqrt{a\ell}}{L_{kes} - \sqrt{a\ell}} \tag{5.65}$$

for the orientational kink distance. At the same time we still must have $L_{or} \ll L_k, L_D$, so that the use of Eq. (5.45) is justified. A criterion for the stable step-flow has been derived also in Ref. [63].

When the detachment from the steps is relevant $x_s \ll L$ the expression (5.46) should be used. In this case the coefficient ν remains always positive, signalizing an instability. However, it is clear that when the average slope $m = L^{-1}$ is increased, the regime $x_s \gg L$ is eventually reached. This conclusion of stable steps flow is to be interpreted with caution; it has been shown that on vicinal 1D surfaces step-flow is only *metastable* and eventually a nucleation event on a terrace destabilizes the step flow growth against mound formation [43].

A more detailed study of step currents for arbitrary orientation has been done by Politi and Krug [72]. They found out that steps can be stabilized against meandering due to the step edge current for some orientations. They also noted that for [110] oriented steps the current due to kink-rounding barriers has a stabilizing effect. Also Pierre-Louis *et al.* have derived an expression for the step current [63], valid also for large slopes m, where multiple height kinks become relevant. They also concluded that [100] oriented steps are destabilized where as for [110] steps the stability depend on the strength of the kink rounding barriers L_{kes}.

5.4 Monte Carlo simulations of meandering instability

Monte Carlo simulations of the SOS model provide a possibility of studying the meandering instabilities in a discrete model. This way the predictions of the theories can be tested in a well controlled environment. The model employed here is the one presented earlier, in Sect. 3.2 the lattice a simple cubic one. The processes included are the deposition of new atoms with rate F, adatoms at the surface are allowed to hop to nearest neighbor sites and desorption is neglected. The rate of hopping is dependent on the local environment through

$$\Gamma = \Gamma_0 \exp(-\beta \Delta E), \tag{5.66}$$

where the activation energy is

$$\Delta E = E_S + n_i E_n + (n_i - n_f)\Theta(n_i - n_f)E_{BB} + (m_i - m_f)\Theta(m_i - m_f)E_{ES}. \tag{5.67}$$

Here E_S is the diffusion barrier on a flat terrace and $n_i E_n$ is the additional barrier when the atom has n_i nearest neighbors at the initial site. This makes the diffusion along the steps *slower* than on the terraces. The energy E_{BB} is added when bonds are broken, n_i, n_f are the number of nearest neighbors in the initial and final state, respectively. The Ehrlich-Schwoebel barrier E_{ES} is implemented by the last term; m_i, m_f are the numbers of next-nearest neighbors in the layers above and below in the initial and final state. This term adds an extra barrier when an adatoms tries to hop to a site above the step. The energy landscape is illustrated in Fig. 5.12. As discussed in sect. 3.2 these rates fulfill the detailed balance condition with respect to the Hamiltonian

$$H = \sum_{\langle \mathbf{r}, \mathbf{r}' \rangle} \left[E_K |h_{\mathbf{r}} - h_{\mathbf{r}'}| + E_{ES}(|h_{\mathbf{r}} - h_{\mathbf{r}'}| - 1)\Theta(|h_{\mathbf{r}} - h_{\mathbf{r}'}| - 1) \right], \tag{5.68}$$

where the kink energy $E_K = (1/2)(E_n + E_{BB})$.

To employ the results of the theory developed earlier in this chapter the parameters must be written in terms of the activation energies of the SOS model. The diffusion coefficients on the terrace and along the steps are obviously $D = \Gamma_0 \exp(-\beta E_S)$ and $D_s = \Gamma_0 \exp[-\beta(E_S + E_n)]$ respectively. The adatom concentration on terraces and the step stiffness were already introduced in sect. 3.3.1

$$c_{eq}^0 = \Omega^{-1} \exp(-4\beta E_K) \quad , \quad \beta\tilde{\gamma} = \frac{2}{a} \sinh^2 \left(\frac{\beta E_K}{2} \right). \tag{5.69}$$

To calculate the adatom mobility along the steps (4.34) one needs to know the barrier for detachment from a kink site to the step edge $E_{det} = E_S + 2E_n + E_{BB}$, resulting in the expression for the mobility

$$\sigma = \frac{a\beta\Gamma_0}{2} \left\{ \frac{\exp\left[-\beta(E_S + 2E_n + E_{BB})\right]}{1 + \exp\left[(\beta/2)(E_{BB} - E_n)\right]} \right\}. \tag{5.70}$$

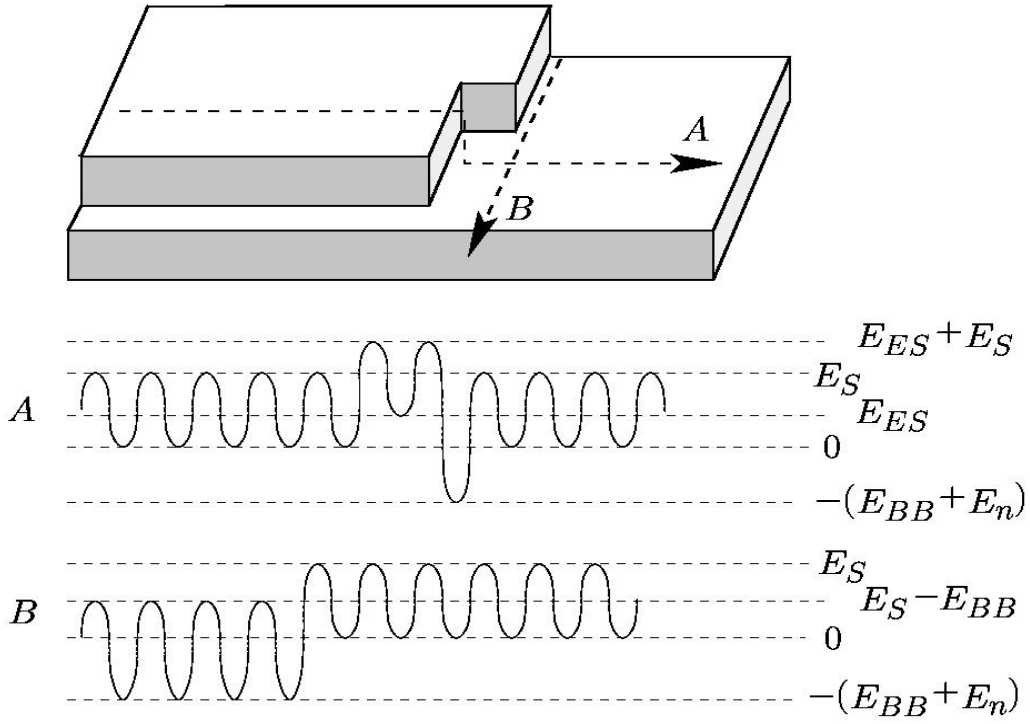

Figure 5.12: The energy landscape of the SOS model. The potentials plotted along lines A,B follow from the Hamiltonian (5.68).

The detachment time of adatoms from an edge site to the terrace reads

$$\tau = \Gamma_0^{-1} \exp[\beta(E_S + E_n + E_{BB})], \tag{5.71}$$

and consequently the length of the step segment covered by a diffusing adatom along the step is $x_s = \sqrt{D_s \tau} = a \exp[(\beta/2) E_{BB}]$.

5.4.1 Meander mechanisms

To study the wavelength of the instabilities two different sets of parameters were used. In the first set (called hereafter set A) the bond-breaking barrier was set to zero $E_{BB} \equiv 0$. Now the hopping rate depends only on the number of nearest neighbor in the initial state n_i, but not on the the final state n_f. Thus the hopping rate along the step is equal to the detachment rate from the edge and the line diffusion along the edges is irrelevant compared to the terrace diffusion. Other activation energies were set to values $E_S = 0.35$eV, $E_n = 0.21$eV and $E_{ES} = 0.15$eV. The temperature had value $T = 375$K, the hopping pre-factor $\Gamma_0 = 2 \times 10^{11} \mathrm{s}^{-1}$ and the deposition flux was varied between $F = 0.025..1\,\mathrm{ML/s}$. System sizes were $1000 \times 30\, a^2$ with 5 steps, with a step distance $\ell = 6a$. In the second set (set B) employed, the bond braking barrier was set to $E_{BB} = E_n = 0.21$eV. The hopping pre-factor was $\Gamma_0 = 4 \times 10^{12} \mathrm{s}^{-1}$ and the flux was varied between $F = 0.005..0.5$ML/s, other parameters had identical values with set A. The difference in the pre-factor Γ_0 is only due to computational convenience so that simulations could be done in the same temperature and flux regime, and has no physical significance. In this regime the ratio of diffusion and deposition rates $D/(F\Omega^2) \sim 10^6..10^9$, resulting in a very low adatom concentration on the terraces. Thus the nucleation on the terraces is absent and the concentration field relaxes very rapidly on the time scale of the step motion, making the quasi-static approximation in the BCF-theory (See Eq.(3.28)) justified.

In both cases, starting with a profile with straight steps, they develop an in-phase meandering pattern as the steps propagate, as seen in snap-shots in Figs. 5.13 and 5.14. Starting the simulation with straight steps implies $L_k = \infty$ and thus comparing with theoretical results the length scale $\tilde{L} = L_D$ always. As mentioned for the parameter set A there is no step diffusion and no kink-rounding barrier, $E_{kr} = 0$, leaving the Bales-Zangwill instability as the only possible mechanism for meandering. To compare with the theory several values for the deposition flux were used and the wavelength λ of the instability was measured directly from the step profiles, by measuring the distance between subsequent minima in the step profile. The estimate for the statistical error was obtained from the variation of the wavelength in a single profile. Each simulation was run until λ was clearly visible. The results shown in Fig. 5.15 are in excellent agreement with the theoretical result Eq. (5.16). The observed value of the wavelength agrees also quantitatively with the theoretical and no parameter fitting is required.

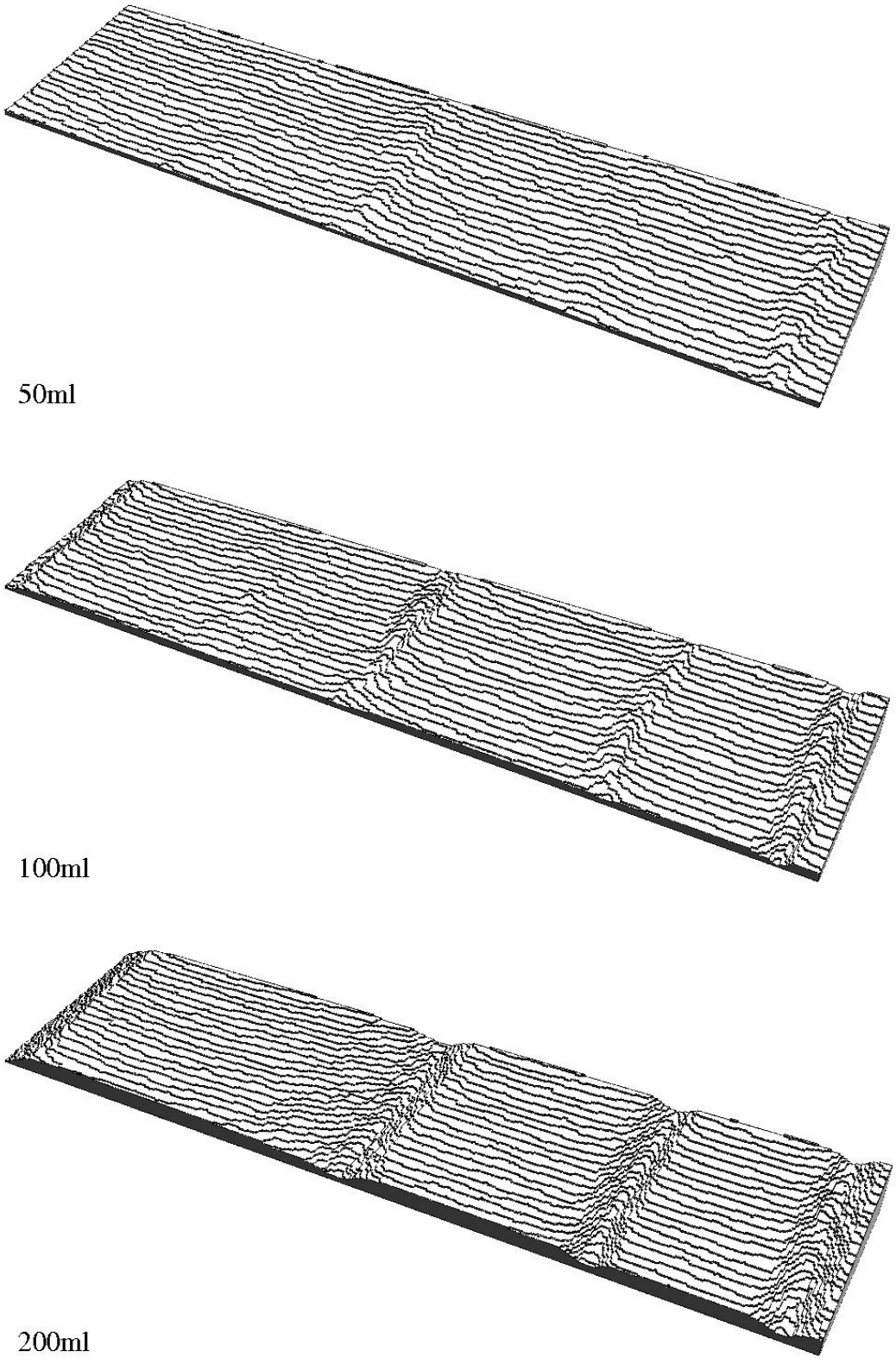

Figure 5.13: The evolution of the SOS model with the parameter set A, deposition flux used was $F = 0.2$ML/s. Size of the system was $120 \times 1000a^2$ sites with 20 steps; a piece of size $120 \times 500a^2$ is shown in the snapshots. At initial state all steps were straight.

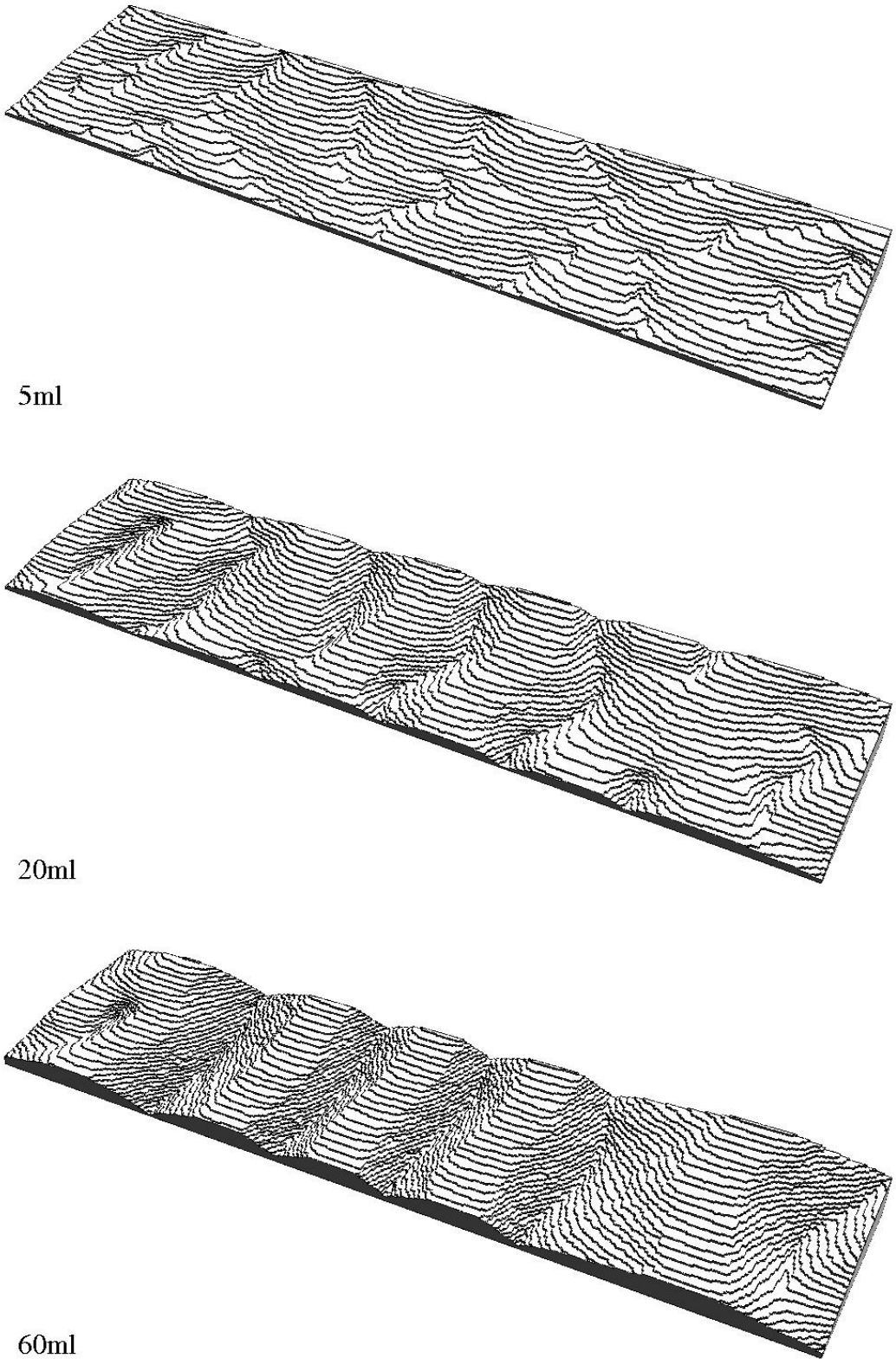

Figure 5.14: The evolution with parameter set B and deposition flux $F = 0.01$ML/s. Again snapshots show a $120 \times 500a^2$ piece from a lattice of size $120 \times 800a^2$, with 20 steps.

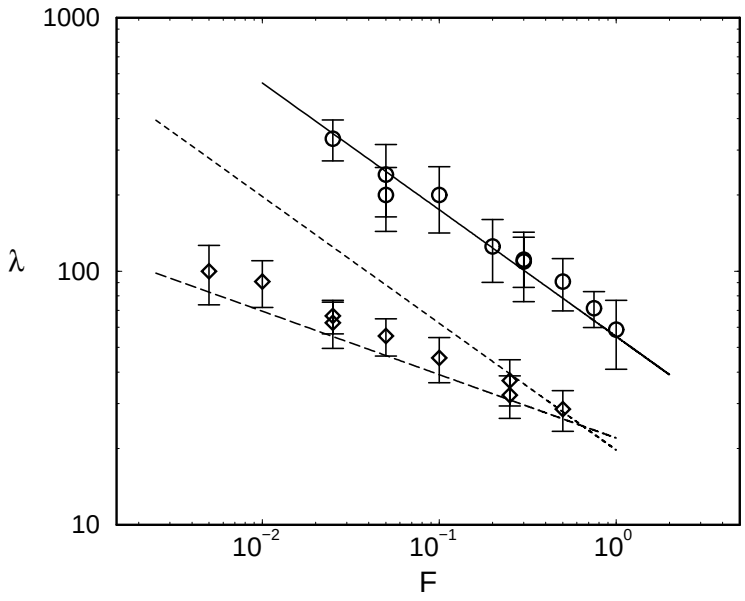

Figure 5.15: Meander wavelength as a function of flux for model I (circles) and model II (diamonds). Each symbol represents a single run on a lattice of size $1000 \times 30a^2$ with 5 steps. The error bars refer to the variation of the wavelength within the configuration. For some fluxes results for a lattice of size $30 \times 1200a^2$ have been included also. The simulations were run until the meander wavelength was clearly visible. The BZ-length (5.16) is plotted as a full line for model I and a short-dashed line for model II. The long-dashed line is the nucleation length (5.37) for model II.

A convincing evidence for the BZ instability is the flux dependence of the wavelength $\lambda \sim F^{-1/2}$, which is inconsistent with the nucleation length $L_D \sim F^{-1/3}$, valid for the case of fast detachment from the steps (See Eq. (5.39)).

A note about the relaxation term $\alpha\Phi L_D^4$ is in order. For the parameters used in the simulations this would actually be the dominating relaxation mechanism, and the other two terms are completely negligible $\alpha\Phi L_D^4 \gg \Omega\tilde{\gamma}(\sigma + \ell\beta D c_{eq}^0)$. Thus if the relaxation due to random nucleation of dimers on the steps is present and of the form $\alpha\Phi L_D^4$, the meandering wavelength should be

$$\lambda = 4\pi\sqrt{\frac{\alpha\Phi L_D^4}{F\ell^2}} = \frac{L_D^{5/2}}{\sqrt{\ell}}. \tag{5.72}$$

For the parameter set A: $\Phi = (L_D/x_s)\ell F$, $x_s = 1$ and $L_D \sim F^{-1/3}$, according to formula (5.39). Equation (5.72) would give a meandering wavelength that is 2 orders of magnitude larger than observed in the simulations. The expression (5.72) also scales as $F^{-5/6}$ in the deposition flux, which clearly disagrees with the $\lambda \sim F^{-1/2}$ dependence

found in the simulations.Thus the relaxation due to nucleation does not seem to play any role and will be neglected for the rest of this thesis.

In simulations with the parameter set B, the detachment from the steps has an extra barrier E_{BB}, meaning that the line diffusion along the step is significant. This implies also a strong kink rounding barrier $E_{kr} = E_{BB}$, since in order to round a kink, an adatom has to first detach from the step as only nearest neighbor hops are allowed in the model. The wavelength of the developed meander pattern was determined as in the previous case, the results are shown again in Fig. 5.15. For this set of parameters the detachment from the steps is negligible since $x_s \gg L_D$, and L_D is the maximal kink distance appearing in the step profiles. The kink rounding barrier is very strong $L_{kes} \gg L_D$ and consequently the wavelength of the KESE instability is given by the nucleation length (5.37). The simulation results are again in good quantitative agreement with the theoretical expression. The wavelength has clearly a $\lambda \sim F^{-1/4}$ flux dependence, inconsistent with the BZ-instability. The wavelength of the BZ-instability calculated from parameters B is also plotted in Fig. 5.15, showing that the observed wavelength is *smaller* than the BZ length. Moreover, the linear stability analysis (sect. 5.1.2) showed that the interval $\lambda = [\lambda_{BZ}/\sqrt{2}, \infty]$ of wavelengths is unstable; the measured meander wavelength is *smaller* than that of the first unstable mode of the BZ theory $\lambda_{BZ}/\sqrt{2}$. Thus it can be concluded that the mechanism behind the meander for parameter set B is not the BZ instability, but the KESE instability.

5.4.2 Cross-over between instabilities

Both of the meandering instabilities occur in the SOS model, which one is the dominant, depends on the significance of the edge diffusion and the strength of the kink rounding barrier. Both of these are controlled in the model presented here by the bond-breaking barrier E_{BB} ($x_s = \sqrt{\exp(\beta E_{BB})}$, $L_{kes} = \exp(\beta E_{BB})$). To determine which effect dominates one should compare the two terms contributing to the destabilization in Eq. (5.53). For the parameters used in the simulations the cross-over should occur at $E_{BB} \approx 0.105$ eV, where the two terms contributing to the destabilizing term, ν, are equal. In the simulations the crossover was studied by varying the bond-breaking barrier in the interval $E_{BB} = 0.01..0.3$ eV. The parameter set B was used, apart from the step distance which was set to the value $\ell = 10a$. The deposition rate was set to $F = 0.25\,\mathrm{ML/s}$. The wavelength was again measured directly from the mean distance between subsequent minima; values plotted in Fig. 5.16 are averages over 5 independent runs and the error-bars are the standard deviation. The cross-over in the wavelength is seen to occur around $E_{BB} \approx 0.10$ eV, in good agreement with the theoretical prediction.

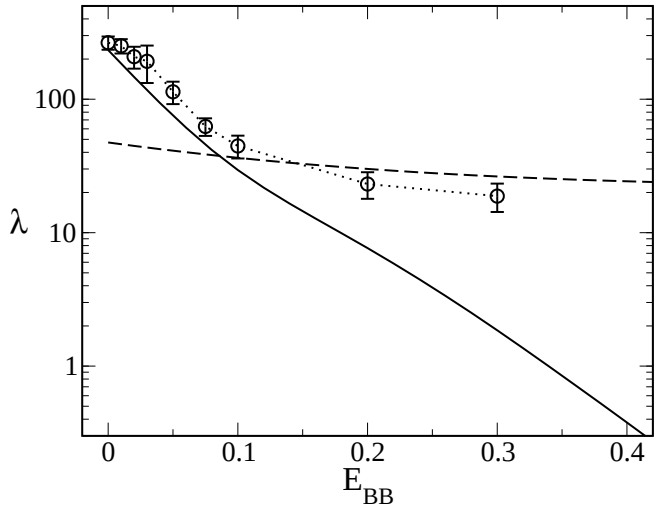

Figure 5.16: The observed wavelengths (circles) for various values of the bond breaking barrier $E_{\mathrm{B}B}$. The full line is the BZ- length (5.16) and the dashed line the nucleation length (5.41). The crossover between the two meander mechanisms occurs around $E_{\mathrm{B}B} \approx 0.1$ eV. Each point is an average over 5 independent runs on a $250..1500 \times 30a^2$ lattice with 3 steps (step spacing $l = 10a$).

5.4.3 Temporal evolution

The two instabilities also differ in their time evolution, already in the initial phase the difference is clear. From Figs. 5.13 and 5.14 one sees that whereas for the BZ-instability the step meanders are all in-phase from the onset, whereas for the KESE instability the steps start to meander with random phase shifts between the steps and is driven to an in-phase mode only later due to the effective step-step interaction. This is in accordance with the theory; the linear stability analysis implied that the in-phase mode is the fastest growing one for BZ mechanism. The KESE instability starts by nucleation of dimers along the steps, which naturally takes place on each step independently of the others.

Also the asymptotic step profiles have quite different shapes. The shape of a step train for both cases is shown in Fig. 5.17. The profiles obtained for the BZ instability (parameter set A) can be compared with the step profile resulting from the step equation (5.19). The simulations of the SOS model produce step profiles with broad and flat maxima and extremely narrow minima. This is a striking contradict with the up-down symmetric profile following from the step equation (see Fig.5.5). The up-down symmetry of the equation (5.19) is an artifact of the truncation of the

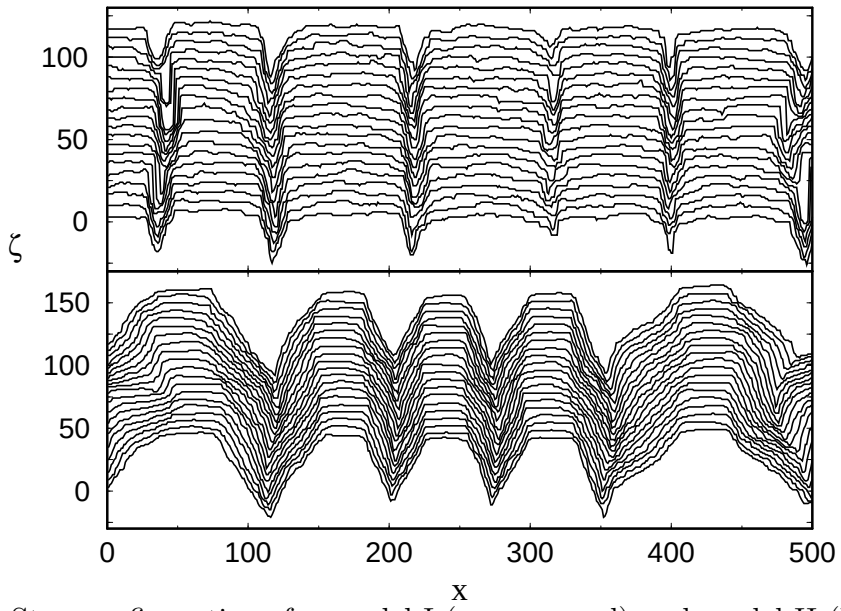

Figure 5.17: Step configurations for model I (upper panel) and model II (lower panel) after deposition of 75 ML at a deposition flux $F = 0.5$ML/s (model I) and $F = 0.01$ML/s (model II). The figures show part of a $800 \times 120a^2$ lattice with 20 steps.

perturbation series and the symmetry is broken if higher order terms are included [24].

The two mechanisms also differ in their asymptotic evolution of the step profiles. To measure the growth rate of the meander amplitude, the step width, defined as

$$w \equiv \frac{1}{L_x} \sum_{x=1}^{L_x} \left[\zeta(x) - \bar{\zeta}\right]^2 \ , \ \bar{\zeta} = \frac{1}{L_x} \sum_{x=1}^{L_x} \zeta(x) \tag{5.73}$$

was calculated during growth. Here L_x is the length of the steps. Results from simulations are plotted in Fig. 5.18 for both meandering mechanisms. The meander amplitude grows for the KESE instability (parameter set B) rapidly at the initial phase, but saturates to a finite value asymptotically. The asymptotic amplitude seems to grow as the meander wavelength grows, suggesting that there could be *slope selection* at the large slope regions between the flat maxima and sharp minima (see lower panel of Fig. 5.17). It has been shown that for large slopes the KESE current arising form the kink rounding barriers has a stabilizing character [63, 71], which could lead to stabilization of the step orientation.

The BZ instability shows quite different temporal evolution. The meander amplitude starts growing slowly, but keeps increasing *linearly* in the asymptotic regime, as indicated in Fig. 5.18. This observation contradicts the earlier results of the amplitude growth of the BZ instability. As was shown in Sect. 5.2.2 the non-linear step equation

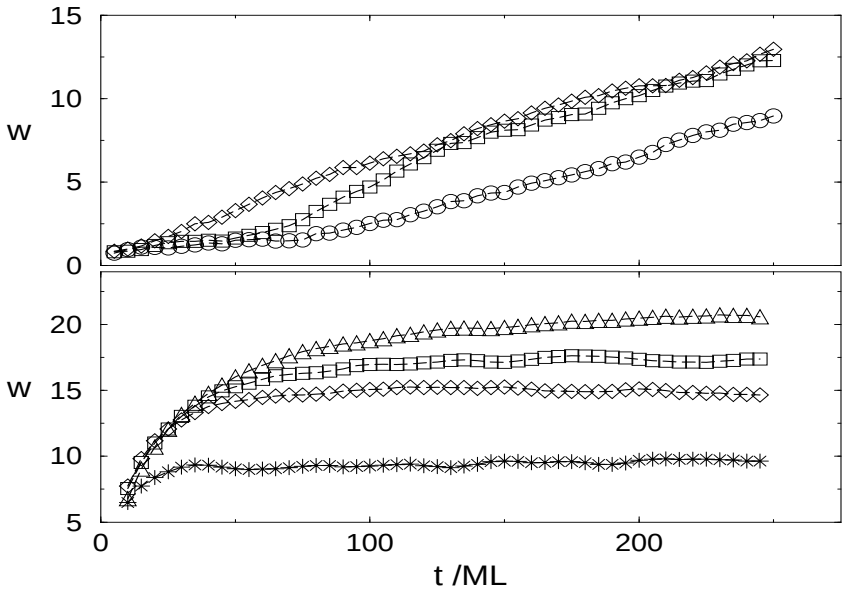

Figure 5.18: Average step width w as a function of time for model I (upper panel, $F = 0.1(\bigcirc), 0.4(\square), 0.8(\diamond)$ ML/s) and model II (lower panel, $F = 0.05(\star), 0.2(\diamond), 0.4(\square), 0.8(\triangle)$ ML/s), from single runs on a lattice of size $500 \times 30a^2$ with 5 steps.

(5.19) predicts that the meander amplitude should grow as $w \sim \sqrt{t}$ [24, 32, 64]. The linear amplitude growth is also at variance with the Monte Carlo simulations conducted earlier [64], where it was found that the step width has a $w \sim \sqrt{t}$ time dependence in the long time regime, in accordance with the step equation. A direct comparison between the model used in Ref. [64] and the model presented here is not possible due to quite different choice of parameterization. Some major differences that could lie behind the discrepancy can be named; in the earlier work the steps were described by single valued functions, thus completely suppressing the occurrence of step overhangs and voids. Secondly, the nucleation on the terraces was prohibited in the simulations of Ref. [64]. The simulations were also done in a very different parameter regime. In the earlier simulation the value of the adatom concentration was set to a value $c^0_{eq} = 0.119$, which is several orders of magnitude higher than the value calculated from the model parameters for the simulations presented here. Indeed, in such a high adatom concentration step flow growth is hardly possible due to frequent island nucleation on terraces, when it is allowed. In the simulation results in Ref. [64] also the wavelength of the meander differed from the theoretical prediction.

The linear amplitude growth of the BZ-instability may be intuitively connected with the strongly asymmetric shape of the step profile (see upper panel of Fig. 5.17).

For the diffusing adatoms it is very hard to reach the narrow fjords between the broad maxima. Thus the minima receive fever adatoms and consequently the minima move with a smaller velocity than the maxima, causing the linear amplitude growth. It should be noted that even addition of higher order terms in the step equation (5.19), breaking the up-down symmetry, does not alter the $A \sim \sqrt{t}$ time dependence of the meander amplitude [24]. This discrepancy between the SOS simulations and the step equation remains to be clarified.

5.4.4 Variation of the ES barrier

So far the Ehrlich-Schwoebel barrier was set to value $E_{ES} = 0.15$ eV in all simulations, which for the temperature T and terrace width ℓ used in the simulations implies a complete ES effect. The effect of the ES barrier appears in the wavelength λ_{BZ}, Eq.(5.16), through the factor

$$f_s = \frac{\ell_{ES}}{\ell + \ell_{ES} + 2a}, \tag{5.74}$$

where $\ell_{ES} \equiv \ell_- - a = a\exp(\beta E_{ES}) - a$ (note that for the SOS model $\ell_+ = a$). The value $E_{ES} = 0.15$ eV implies $f_s \approx 1$ for all parameters used so far.

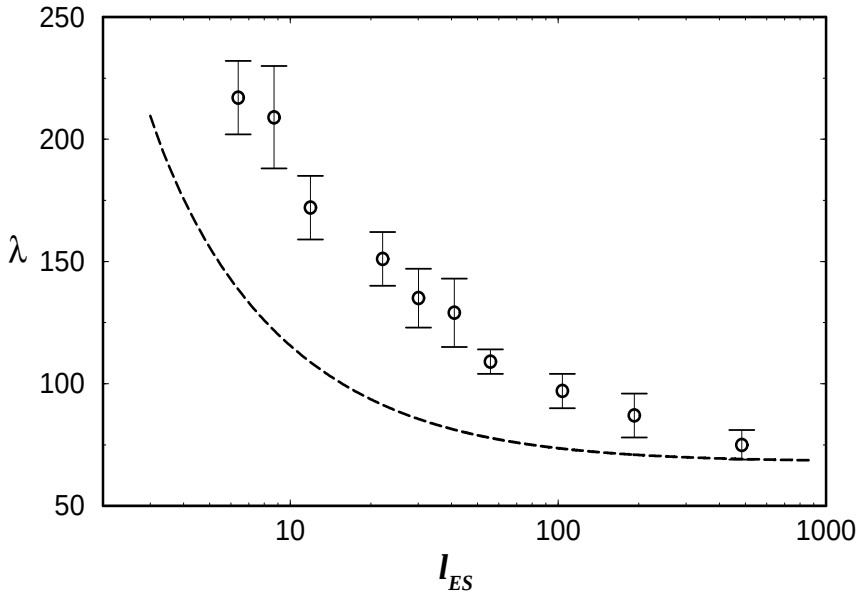

Figure 5.19: Meander wavelength as a function of the ES length $\ell_{ES} = D/k_- - a$ for model I at $F = 0.25$ML/s. Each symbol is an average over 5 runs on a lattice of size $1250 \times 15a^2$ containing a single step (step spacing $\ell = 15a$). The dashed line shows the BZ prediction (5.16).

In order to study the effect of a finite ES barrier simulations using the parameter set A, with a deposition flux $F = 0.25$ML/s and step spacing $\ell = 15a$ were conducted for various values of ES barrier $E_{ES} = 0.06 - 0.20$ eV. For the Schwoebel length this means the interval $\ell_{ES} = 5 - 486\,a$. To determine the wavelength, 5 independent runs with a system size $1250 \times 15a^2$, with a single step on the surface were conducted. Having only a single step in the system and using periodic boundary conditions implies that the steps are perfectly in-phase . The wavelength was measured again directly from the profile and averaged over the runs. The results obtained are shown in Fig. 5.19. The simulation result is seen to be in qualitative agreement with the theoretical prediction, but with a quantitative discrepancy. The simulation data could be fitted by reducing the Schwoebel length ℓ_{ES} by a factor 1/4. However, there is no justified reason in doing so. It may be argued that also the step roughness affects the Schwoebel length since it is an average hopping rate over the step edge, and the local ES barrier depends on the step morphology. This cannot be the reason in the simulations here; with the implementation of the ES barrier employed here the interlayer hopping rate is *slower* over a kinked step compared to the straight step. This would rather increase the Schwoebel length ℓ_{ES} than reduce it. This issue remains unsolved for the time being.

5.5 Step meandering in experiments

The step meandering instabilities have received much less experimental attention than the mound formation on singular surfaces, which has been studied in various materials and surface orientations (see [71] and references therein). Qualitative observations of meandering have been reported in growth experiment on GaAs(1 1 0) surface [91], on Cu(1 1 17) surface [81] and on a surface vicinal to Pt(1 1 1). In the earlier works the instability was assigned to the Bales-Zangwill mechanism.

The first quantitative measurements on the meander wavelength were reported recently by Maroutian *et al.* [50–52]. They measured the wavelength from STM images taken from Cu(1 1 17) and Cu(0 1 12) surfaces after deposition of multiple adlayers. The two surface orientations are both vicinal to the (1 0 0) singular surface and have the same average step distance $\ell = 2.17$ nm. The surfaces differ by their step orientation; the steps on Cu(1 1 17) surface run in the close packed $\langle 110 \rangle$ direction and on Cu(0 1 12) surface the steps run in $\langle 100 \rangle$ direction, having an open structure. The experiments were not consistent with the BZ mechanism neither in the flux dependence nor in the temperature dependence.

The results on the Cu(1 1 17) surface with close packed steps can be explained by the KESE instability; the adatom diffusion along the close packed steps is very fast. The case would qualitatively correspond to the parameter set B of the simulation presented here. The measured dependence on the deposition flux $\lambda \sim F^{-0.21 \pm 0.08}$ is in

fair agreement with the theoretical prediction $\lambda \sim F^{-1/4}$. Also the activation energy of the wavelength $E_a = 0.092$ eV corresponding to energy barrier $E_s = 4E_a = 0.35$ eV for the edge diffusion agrees reasonably well with the result $E_s = 0.45 \pm 0.08$ eV obtained from time dependent equilibrium step fluctuations [20]. The evidence of a strong kink-rounding barrier for $\langle 110 \rangle$ steps, necessary for the KESE instability, is still missing. Re-interpretation [34] of the experimental measurements on the time dependent step fluctuations [20], in the light of the results for step mobility presented in Sect.4.3.1 would suggest a barrier $E_{kr} \approx 0.41$ eV, which would indicate a strong kink-rounding barrier. Also kinetic Monte Carlo simulations of a more detailed model for Cu surfaces, having the correct symmetry and energy barriers taken from EAM calculations, shows a meandering instability due to KESE [79].

A meandering instability was observed also on the Cu(0 1 12) surfaces. In this case the steps run in the $\langle 100 \rangle$ direction and are fully kinked. Presumably diffusion along such steps is much slower. Also the nucleation at the initial stage of growth is not well described by the one-dimensional nucleation theory presented earlier, but should be replaced with a more microscopic description. Thus the only candidate for

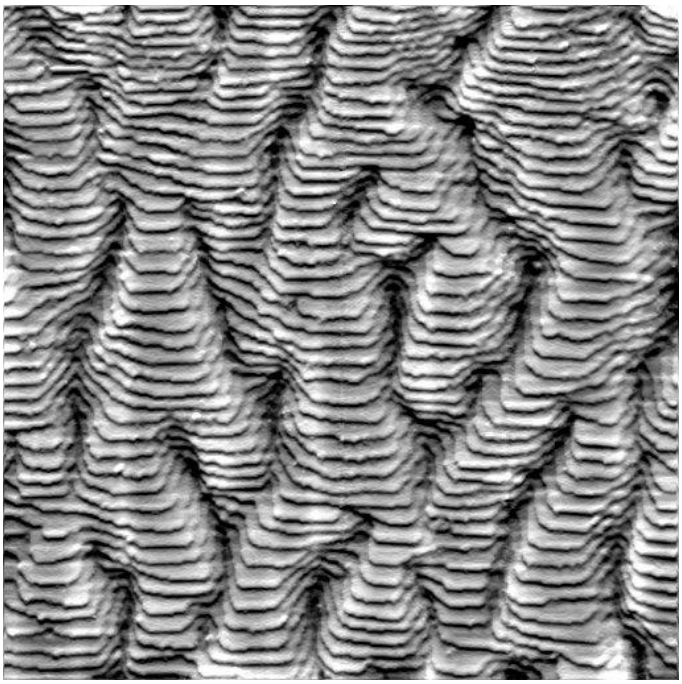

Figure 5.20: A STM $100 \times 100\,\mathrm{nm}^2$ mage of Cu(1 1 17) surface after deposition of 18 ML at flux $F = 0.003$ML/s in temperature $T = 280$ K The steps run in the close packed $\langle 110 \rangle$ direction and the meandering is due to the KESE instability. The morphology is quite similar to the simulation profiles shown in Fig. 5.14. Courtesy of H-. J. Ernst

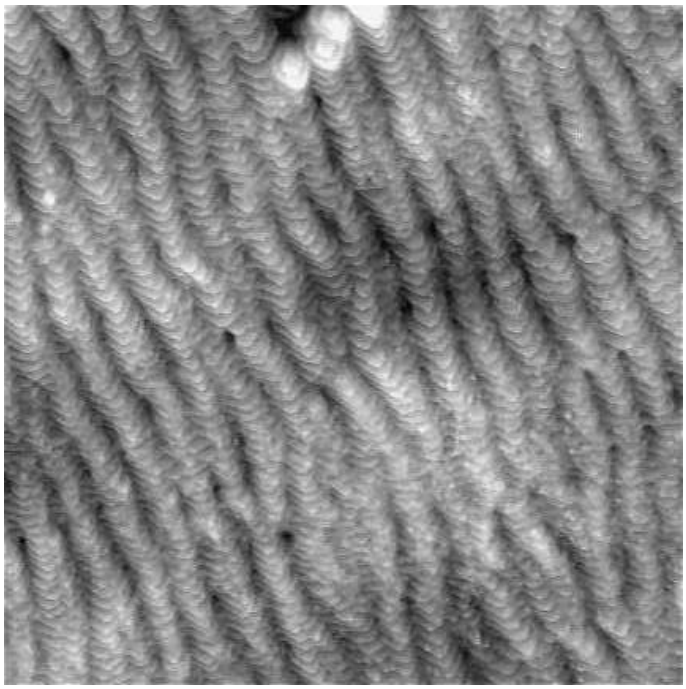

Figure 5.21: A $130 \times 130\text{mn}^2$ STM image of Cu(0 1 12) surface after deposition of 20 ML at flux $F = 0.003$ ML/s at temperature $T = 250$ K. The step has a sawtooth formed profile, presumably reflecting the symmetry of open $\langle 100 \rangle$ steps. The origin of the meandering of open steps is still an open question. Taken from Ref. [52]

the meandering mechanism is the BZ-instability. The experimental result for the flux dependence of the wavelength $\lambda \sim F^{-0.17}$ disagrees with the theoretical prediction $\lambda \sim F^{-1/2}$. In the MC simulations of open steps, done by Rusanen *et al.* [79], the $\langle 100 \rangle$ oriented steps were found to be stable. In the simulations of Ref. [79] the employed activation energies were taken from EAM calculations of close packed steps and as a diffusion barrier along the open $\langle 100 \rangle$ steps the kink-rounding barrier of the $\langle 110 \rangle$ steps. The dynamics of atoms along the open steps might however differ from the fully kinked $\langle 110 \rangle$ steps, as the open steps are not so rough as fully kinked $\langle 110 \rangle$ due to atomic relaxation of the steps. Also theoretical considerations of the KESE instability state that for $\langle 100 \rangle$ steps the KESE effect should be stabilizing [73]. Presently the meandering on Cu(0 1 12) surface remains a mystery.

Chapter 6

Breakdown of the step-flow growth

The step-flow growth on a vicinal surface has been seen in experiments [50,91] and in simulations [34,76] to be only a *meta-stable* growth mode. Even if the nucleation of islands on terraces is very rare, $\ell_D \ll \ell$, sometimes nucleation occurs and the growth may be destabilized against mound formation, since up-hill surface current $J(\ell)$ tends to enhance fluctuations in the vicinal profile if the current is an increasing function of the inter-step distance $J'(\ell) > 0$ [37,39].

Another mechanism that may destroy the morphology of a step train, where only steps of one sign appear, is obviously formation of vacancy islands. It is imaginable that a strong meander can lead to the formation of a closed loop in the step profile and thus to breakdown of the step-flow mode. Depending on the growth conditions the step-flow may last over deposition of hundreds of monolayers, though.

6.1 Island nucleation on the terraces

The intuitively clearest way of destabilizing the step-flow growth is the nucleation of islands on the terraces. In the analysis so far nucleation has been neglected altogether, but it is of course always present on a real surfaces, even if it is very rare. Once an island is nucleated on a terrace it serves as a nucleus for a mound to be grown there, exactly as on a singular surface. The island nucleation is however severely suppressed on a vicinal surface, since the steps absorb adatoms and thus their density is significantly lower than on a singular surface. In particular so if the step density is high, meaning that the slope is large.

6.1.1 Nucleation length ℓ_D

It is rather obvious that the mean distance between the island nucleation centers ℓ_D is different on a vicinal than on the singular surfaces. On a singular surface the

nucleation length ℓ_D can be calculated using the argumentation employed in Sect. 5.3 to calculate the nucleation length along the steps [71]. The number of nucleation events $N(l, \Delta t)$ in a region of linear size l in a time interval Δt is given by the product of the number of atoms arriving on the surface $F\Omega l^2 \Delta t$ and the probability of meeting another adatom. The probability of meeting another atom is a product of the number of distinct visited sites $\approx l^2$ and the average adatom concentration $\langle c \rangle$, which can be obtained from the BCF theory. The nucleation length is then given by the relation $N(\ell_D, (F\Omega)^{-1}) = 1$ and the result is [71]

$$\ell_D \approx a \left(\frac{D}{\Omega^2 F} \right)^{1/6} . \tag{6.1}$$

This expression remains valid also for vicinal surfaces, as long as the island separation is much smaller than the step spacing $\ell_D \ll \ell$.

In the opposite limit the effect of the steps must be taken into account. Following the same argumentation that led to Eq. (6.1) the expression in the vicinal case may be derived. On a terrace segment of length $\ell_{||}$ in the step direction, the number of new atoms arriving on the segment is $F\Omega\ell_{||}\ell\Delta t$ (ℓ is the terrace width). After its arrival, an adatom diffuses on the terrace before being captured by the step. In the direction perpendicular to the steps it diffuses a distance $\sim \ell$ and, since the diffusion is isotropic, in the step direction also a distance $\sim \ell$, covering thus an area $\sim \ell^2$ before being incorporated to the step. The probability to encounter a terrace adatom is then $\sim \ell^2 \langle c \rangle$. The average concentration can be solved form the BCF equation on a terrace (see Sect. 3.3). Assuming straight steps, the problem is essentially one dimensional and the relevant equations read

$$D\partial_{yy} c + F = 0 \ , \ c(0) = c(\ell) = 0 \tag{6.2}$$

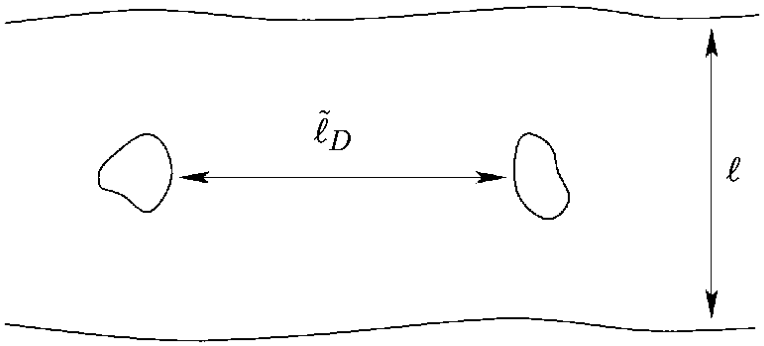

Figure 6.1: The mean island separation in the step direction. In the direction perpendicular to the steps the typical distance between the islands is the terrace width ℓ.

where the Ehrlich-Schwoebel effect has been for simplicity neglected and the attachment to the steps is irreversible, implying $c^0_{eq} = 0$. The resulting average density reads $\langle c \rangle \approx (F/D)\ell^2$. Putting everything together, the number of nucleation events on a terrace segment reads

$$\bar{N}(\ell_{||}, \Delta t) = F\ell_{||}\ell\,\ell^2\,\langle c\rangle\Delta t = F\ell_{||}\ell^5(F/D)\Delta t. \tag{6.3}$$

Now the nucleation length follows again from the relation $\bar{N}(\tilde{\ell}_D, (F\Omega)^{-1}) = 1$, yielding

$$\tilde{\ell}_D = \frac{D}{F\ell^5} \tag{6.4}$$

for the nucleation length. Here $\tilde{\ell}_D$ is the average distance between islands in the step direction, in the perpendicular direction the average distance is naturally the terrace width ℓ.

The crossover between the two cases occurs approximately when $\tilde{\ell}_D = \ell_D$, which leads to the cross-over value for the flux $F_X = D/\ell^6$. Re-scaling the deposition flux with the crossover value leads to expression for the nucleation length

$$\ell_D \sim \ell \begin{cases} f^{-1} & \text{for } f < 1 \\ f^{-1/6} & \text{for } f > 1 \end{cases}, \; f \equiv F/F_X = (F/D)\ell^6. \tag{6.5}$$

$f \gg 1$ means that the surface can be considered as a singular one, and $f \ll 1$ means that most of the deposited atoms are captured by the steps. The results of this simple argument are confirmed by simulation results on a semi-realistic SOS model for FCC metal surfaces [80].

In the initial phase, before the island density saturates, the mean island separation decreases as new islands are continuously nucleated. Base on scaling arguments, it has been predicted that the mean island separation ℓ_{eff} on a singular surface depends on the coverage $\Theta = F\Omega t$ as

$$\ell_{eff} \sim \left(\frac{\Theta F}{D}\right)^{-\gamma}, \tag{6.6}$$

in the intermediate regime, where the adatom density has saturated, but the island density still increases. The exponent γ scaling exponent for the saturated island separation [96] and it acquires a value $\gamma = 1/(2 + 2d)$ when dimers are assumed stable. Assuming that this applies also for the nucleation on a vicinal surface, the island separation should scale as

$$\ell_D^{eff} \sim \ell \begin{cases} (\Theta f)^{-1} & \text{for } f < 1 \\ (\Theta f)^{-1/6} & \text{for } f > 1 \end{cases} \tag{6.7}$$

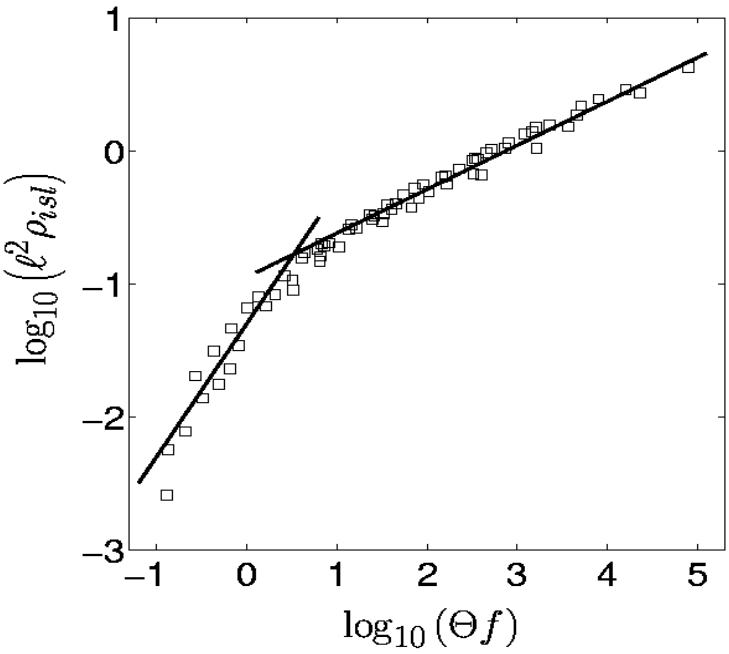

Figure 6.2: The island density on a vicinal surface as a function of the scaled flux $f \equiv F/F_X$ for various coverages Θ. The simulation results are in agreement with the scaling result (6.8). Taken from Ref. [80].

Equivalently to the nucleation length one can measure the island *density*

$$\rho_{isl} = \ell^{-2} \begin{cases} \Theta f & , f < 1 \text{ (stepped surfaces)} \\ (\Theta f)^{1/3} & , f > 1 \text{ (singular surfaces)} \end{cases} \tag{6.8}$$

The coverage dependent island density on a vicinal surface $f \ll 1$ has been derived earlier from a more elaborate theory by Bales [3]. The simple arguments presented here produce the leading order term of the previous result in ℓ. Also the same coverage dependence $\rho_{isl} \sim \Theta, f \ll 1$ is found in the treatment by Bales [3] Simulation results for the island density, shown in Fig. 6.2, are also seen to be in good agreement with the theory.

6.1.2 Mound formation

Similarly to the singular surface the islands nucleated on the terraces form a template for mounds to be grown. In order to have mounds forming, a new island should be nucleated on top of an existing one, before it is incorporated to the advancing step [61].

To calculate the nucleation rate on top of islands a simple mean-field description is not enough; since the number of atoms on an island is very small, the nucleation events are dominated by rare fluctuations in the number of atoms on an island [42, 70]. However the nucleation rate has been readily calculated [25, 42], and these results may be directly applied. The nucleation rate $\omega = FAp_{nuc}$, obviously depends on the size of the island. Here F denotes the deposition flux, A the area of the island and p_{nuc} is the probability for a deposited atom to find another on top of the island and form a dimer before descending over the island edge. Assuming that once an island is nucleated on a terrace, it receives roughly half of the freshly deposited adatoms landing on the terrace segment of length ℓ, the radius of the island grows with a velocity $v \approx (1/2)v_{step}$, where $v_{step} = F\ell\Omega$ is the velocity of a step without an island on the terrace. The number of nucleation events up to time t^* then reads

$$N_{nuc}(t^*) \equiv \int_0^{t^*} \mathrm{d}t\, \omega(t) = \int_0^{t^*} \mathrm{d}\, tFA(t)p_{nuc}(t), \tag{6.9}$$

where the nucleation probability depends on time as the size of the island changes. A criterion for the mound formation is that during deposition of one monolayer one new island will be nucleated on top of terrace island, on average [61]. Otherwise the island collides with an advancing step and is incorporated into it. A quantitative criterion for the destabilization of the step flow against mound formation is given by

$$N_{nuc}(t^* = (\Omega F)^{-1}) > 1. \tag{6.10}$$

The nucleation probability p_{nuc} is approximately given by the probability that two adatoms are present at the same time on top of a single island, *i.e.* it is assumed that the atoms on an island always meet. The result for the nucleation rate then follows as [42]

$$\omega = FAp_{nuc} = \frac{\pi^2 F^2 r^4}{2D}\left(r^2 + \frac{Dr}{k_-}\right) \tag{6.11}$$

for a circular island of radius r, here D is the diffusion coefficient on a flat terrace and k_- the rate of attachment to the step edge from a terrace above, encountered already in the BCF theory. Inserting the approximation $r = (1/2)v_{step}t \approx (1/2)\Omega F\ell t$ into ω and integrating over time, the criterion (6.10) reads

$$\int_0^{(\Omega F)^{-1}} \omega(t)\,\mathrm{d}t = \frac{\pi F}{\Omega D}\left(\frac{\ell}{2}\right)^5 \left(\frac{\ell}{28} + \frac{\ell_{ES}}{12}\right) > 1, \tag{6.12}$$

where $\ell_{ES} \equiv (D/k_-) - a \approx (D/k_-)$ is the Ehrlich-Schwoebel length. In the limit of strong ES effect $\ell_{ES} \gg r$ the adatoms travel multiple times across the island before descending and the assumption that if two atoms are present on the island they always meet is valid. In the opposite limit the expression (6.12) is only an upper limit as the true nucleation rate is smaller [42].

When the flux is below the critical flux

$$F < F_c \equiv \frac{\Omega D}{\pi}\left(\frac{2}{\ell}\right)^5\left(\frac{\ell}{28}+\frac{\ell_{ES}}{12}\right)^{-1}, \tag{6.13}$$

islands are nucleated on the terrace, but they are incorporated to the steps before a new island is nucleated on them. Thus the growth retains its 2D character. When islands are nucleated on the terrace the morphology of the steps is also affected by this. As the islands collide with the step, the step jumps discontinuously forward. Simulations show that the step meandering instability takes place also when island are nucleated [80]. However in this case the dynamics of the steps are different from the case described in the previous section and the results cannot be directly applied. In fact, there is evidence from MC simulations that the meandering wavelength is neither of the two, BZ- or KESE- length, but something else [80]. The asymptotic regime of the growth was not accessible in the simulations of Ref. [80], so the asymptotic wavelength of the meander in the presence of terrace nucleation is not yet clear. It is also plausible that eventually the terrace nucleation ceases as the steps come closer to each other due to the strong meander.

$F < F_C, \ell \sim \tilde{\ell}_D$ is an intermediate state between pure step-flow and mound growth. For larger fluxes (or wider terraces) the mounding instability sets in and the step-flow growth is only transient state, asymptotic state being a genuine 3D mound growth [43], and the morphology of the surface is qualitatively the same as on singular surfaces [76].

In growth experiments on vicinal Cu surfaces [50] mounds formed on terraces appear in highly ordered rows. This suggests that the mounds do not grow independently and that the nucleation events of terrace islands are correlated. Thus the simple scenario presented here for island nucleation may not be sufficient.

6.2 Appearance of vacancy islands

Another possibility for termination of the step-flow growth is provided by the formation of *vacancies* on the terraces. A vacancy island is formed when the step crosses itself due to a very strong meander. Such step configurations are formed when an adatom island collides with the step creating a large perturbation on the step profile, or due to large amplitude (late time) meandering due to BZ- or KESE- instability.

6.2.1 Relevant length scales

The relevant length scale naturally depends on the mechanism through which the vacancies are nucleated. When they are due to strong meandering, the length scale for the separation between vacancies is the wavelength of the meandering instability λ_M.

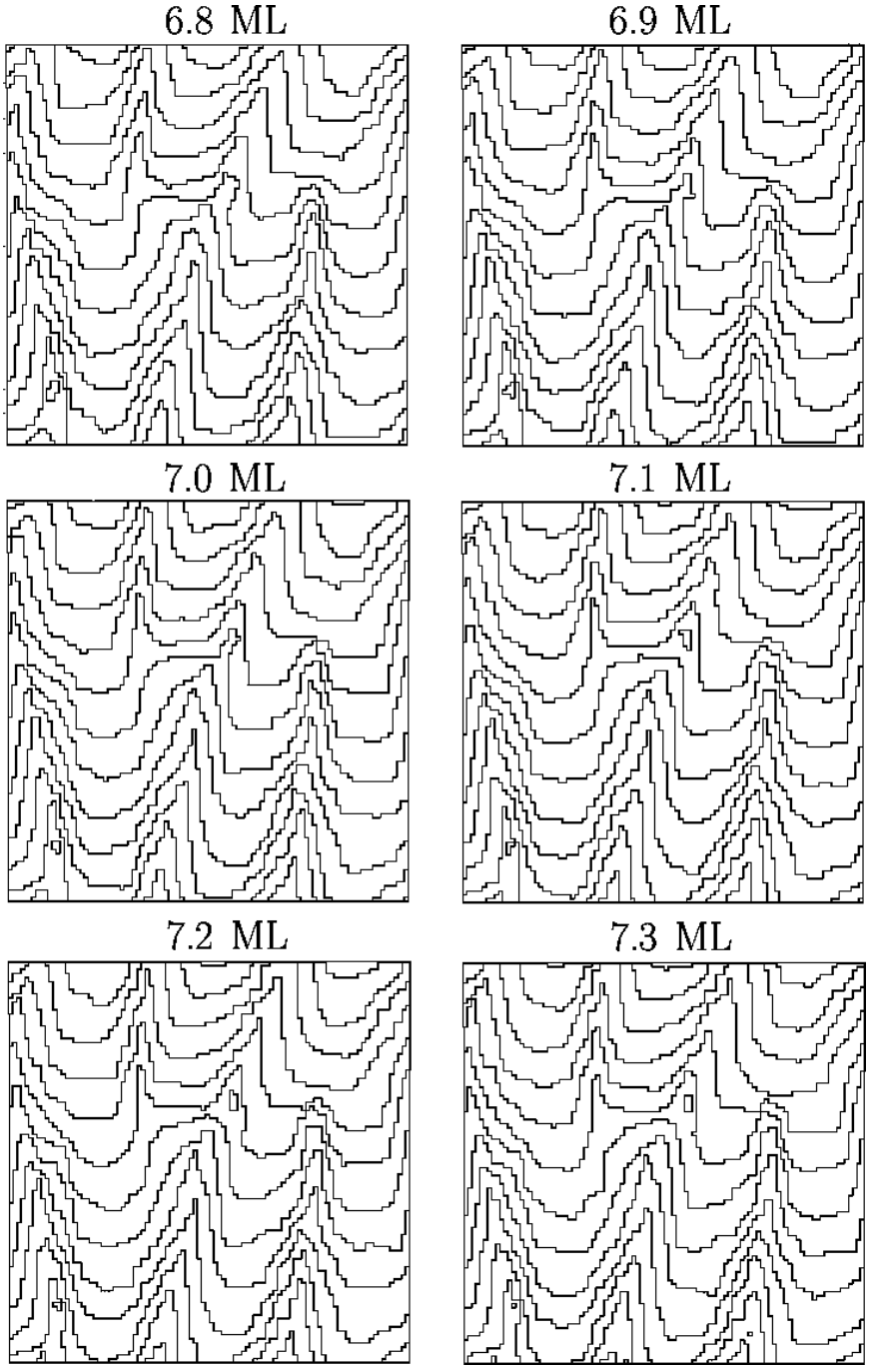

Figure 6.3: Subsequent step configurations in the MC simulations of the SOS model at time interval 0.1 ML after deposition of 6.8 ML. Vacancy islands are formed where the phase difference between the steps is large. The simulation parameters were $F = 1.0\,\mathrm{ML/s}\,, T = 400K\,, E_s = 0.35\mathrm{eV}\,, E_n = 0.15\mathrm{eV}\, E_{BB} = 0.20\mathrm{eV}\, E_{ES} = 0.20\mathrm{eV}, \ell = 10\,a$ and system size $100 \times 100\,a^2$.

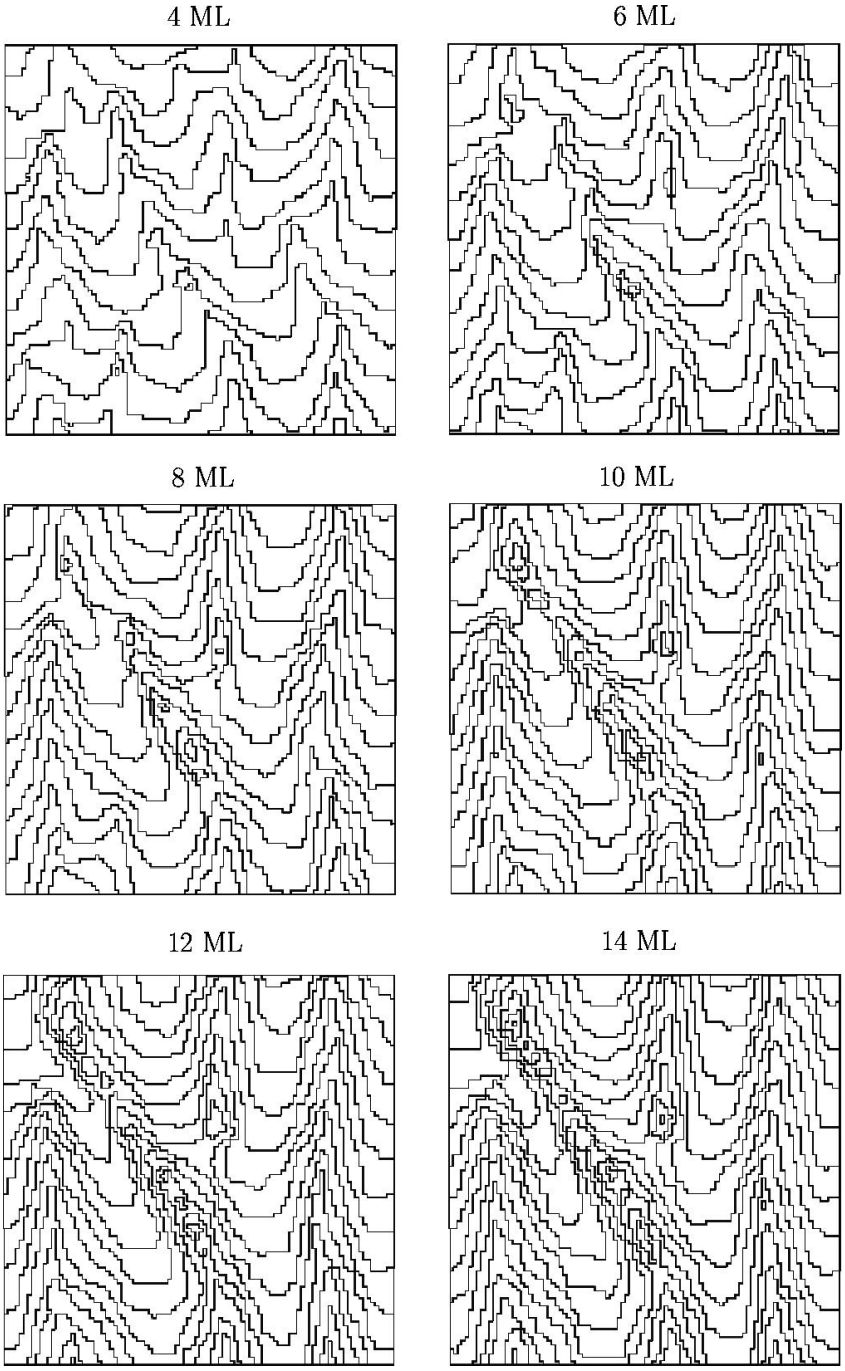

Figure 6.4: A vacancy island acts as a pinning center for the following steps. As the following steps are pinned, they might form a closed loop around the vacancy, forming thus a deepening crater. Subsequent step configurations in the MC simulations of the SOS model at time interval 2 ML after deposition of 4 ML. The simulation parameters were $F = 2.0\,\mathrm{ML/s}\,, T = 400K\,, E_s = 0.35\mathrm{eV}\,, E_n = 0.15\mathrm{eV}\, E_{BB} = 0.20\mathrm{eV}\, E_{ES} = 0.20\mathrm{eV}, \ell = 10\,a$ and system size $100 \times 100\,a^2$.

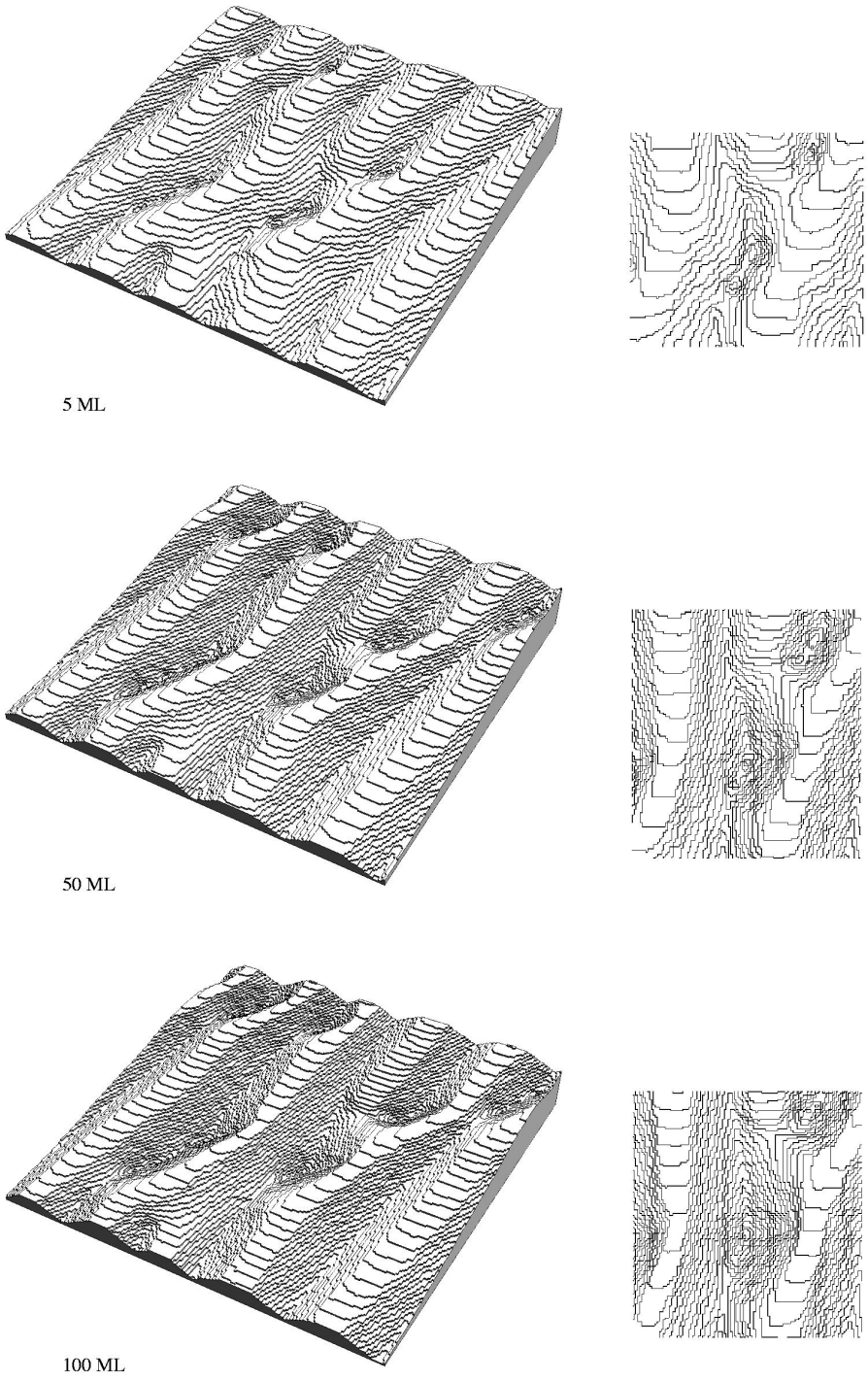

Figure 6.5: The craters deepen and grow in lateral size during further growth. Finally the craters start to coalesce thus leading to mounds on the surface. Snap shots from simulations of the SOS model, the simulation parameters were $F = 1.0\mathrm{ML/s}\,, T = 400\mathrm{K}\,, E_s = 0.35\mathrm{eV}\,, E_n = 0.15\mathrm{eV}\, E_{BB} = 0.20\mathrm{eV}\,, E_{ES} = 0.20\mathrm{eV}, \ell = 10\,a$ and system size $250 \times 250\,a^2$.

When the vacancies are due to island collisions with the steps, the relevant length scale in the step direction would be naturally the mean island separation on the terrace $\tilde{\ell}_D$. In the perpendicular direction the situation is not so simple. For the KESE case it seems that the vacancies are formed at sites where the phase difference in the meander between consecutive steps is large as seen in the snap shots from MC simulations of the SOS model in Fig. 6.3. Thus the distance between the vacancies in the direction of vicinality is related to the phase correlations between the steps. In previous work by Rost *et al.* [76] it was found in MC simulations of an SOS model, and in the continuum description of surface growth, that step-flow growth is unstable against mound formation. They also observed that the mounds were preferably formed at sites where the meander pattern has large phase differences. In the previous work [76] the step meandering was due to the BZ-instability, whereas in this work the meander in the simulations was due to the KESE-instability.

In the initial phase of the KESE-instability each step meander independently, thus the meanders are completely uncorrelated. For the BZ-instability the meander is in-phase from the outset (see. Figs 5.13 and 5.14). Whether vacancies are formed, depends on the rate at which the phase correlations increase compared to the rate of the amplitude growth. Since a theory for the step evolution in the KESE case is still missing one has to resort to simulations.

For this purpose simulations of the SOS model presented in Sect. 3.2 were conducted. The activation energies were set to values $E_S = 0.35$ eV for the terrace diffusion, $E_n = 0.15$ eV controlling the rate of the edge diffusion, $E_{BB} = 0.2$ eV for the bond-breaking barrier and $E_{ES} = 0.2$ eV for the ES barrier. The temperature was set to $T = 400$ K. In this regime the meander is due to the KESE instability. The steps forming a closed loop in the SOS configuration were identified as vacancy islands. This method does does not make a difference between vacancy and adatom islands, but in the parameter regime where the MC simulation were conducted, no island nucleation takes place on the terraces. The loops were searched by first finding the contour lines separating the lattice in parts where the surface height $h(i, j)$ is higher or lower than some reference height h_{ref}. By varying the reference height h_{ref} between the highest and the lowest value of the height found in the configuration, all steps are found. After finding a step it was checked whether the same point appears in the contour twice, indicating a closed loop. Steps having length 4 were neglected as they mark adatoms.

To check the dependence of the vacancy distance in the step direction, the time it takes to create a vacancy island $\langle t \rangle$ starting from straight steps was measured. This was done for various system sizes in the step direction $L_x = 30..250a$. Since the number of potential sites for vacancy nucleation $n \sim L_x/\lambda_M$, the waiting time is expected to scale as $\langle t \rangle \sim L_x^{-1}$. The simulation results confirm this result, as seen clearly in Fig. 6.6.

The length scale in the direction of vicinality is more difficult to obtain. Acquiring

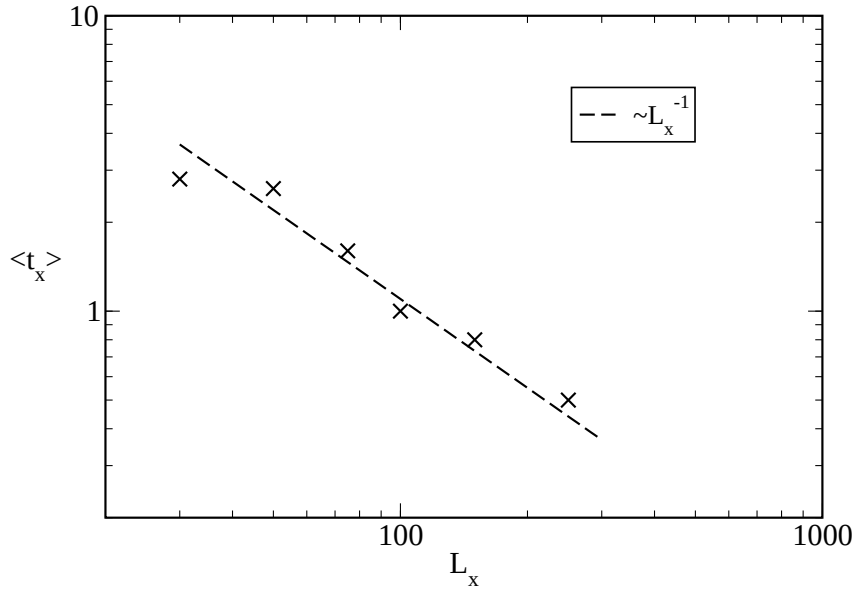

Figure 6.6: Mean waiting time $\langle t_x \rangle$ before a vacancy is created due to strong step meander. The number of potential nucleation sites for vacancies is $n \sim L_x/\lambda_M$, leading to $\langle t_x \rangle \sim L_x^{-1}$ behavior for the waiting time. The results are obtained from 20 independent runs for each point, by measuring the time the first vacancy appears. System size was $30..250 \times 100a^2$, with 10 steps. Simulation parameters are described in the text.

good statistics for the vacancy separation, simulations of extremely large system sizes would be necessary. Here another approach was taken instead. Using relatively small system sizes, $L_y = 40..150a$, with a step distance $\ell = 10a$ it was studied whether vacancies are nucleated at all; if the system is too small the end configuration is a perfect in-phase step train. If there are more steps, vacancies will be created. Thus varying the system size L_y an estimate for the distance between the vacancies in the vicinal direction is obtained. Results from simulations for different system sizes are shown in Fig. 6.7. The probability of creation of a vacancy changes quite rapidly from zero to one as the number of steps in the system increases. The probability of course also depends on the length of the steps L_x since it controls the number of possible nucleation sites (number of meanders). However, the probability may saturate at some asymptotic value when $L_x \to \infty$. For example, for the simulations presented here one could conjecture that for $L_x \to \infty$ the vacancies are created if $L_y > L_y^C \approx 50a$; thus the distance between the vacancies should also be of this order in the direction of the vicinality. The results presented here are quite preliminary as there is far too little data to make justified conclusions.

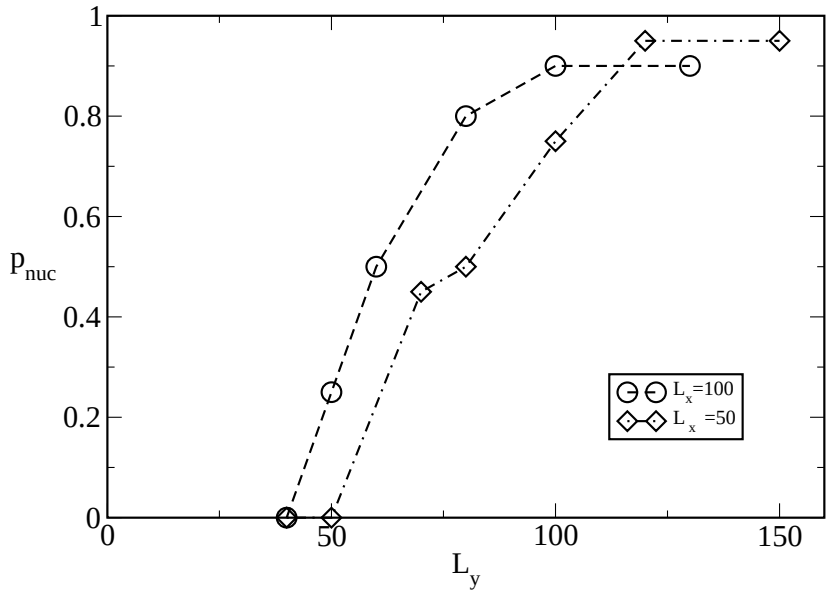

Figure 6.7: The probability of formation of a vacancy in a small system. For small systems the step train reaches an in-phase configuration and no vacancies are formed. The system size $p_{nuc}(L_y) = 0.5$ yields an approximation for the distance between vacancies in the direction of the step train. Results are obtained from 20 independent runs by simply counting the vacancy nucleation events. Simulation parameters are described in the text.

In the case of the BZ instability the steps are in-phase from the outset, due to the collective nature of the meandering instability. However, in simulations the amplitude of the meander grows linearly in time (See Sect. 5.4.3), leading eventually to very strong meander. In this case even a small fluctuation may cause a step to cross itself, creating a vacancy island. Such events are seen in simulations, but they are rare, and their characteristic distance seems to be large compared to the system sizes used in the simulation. Thus no quantitative statements about the relevant length scales can be made.

After the vacancies have been nucleated, they form pinning centers for the following steps. It is then intuitively clear that unless vacancies are rapidly filled, they serve as a nucleus for a crater to be formed. The filling of vacancies is hampered by the ES barriers suppressing the inter-layer transport. Once a crater has been created it grows in depth as well as diameter, similarly to the mounds in the Villain-instability. Eventually the craters start to coalesce and the asymptotic morphology looks similar to the one created through mound formation.

Chapter 7

Summary

In this work the growth instabilities on vicinal surfaces, the Bales-Zangwill instability (BZ) and the instability arising from the kink-Ehrlich-Schwoebel-effect (KESE), leading to formation of long ripples on the surface were studied. In order to explain these instabilities, it is necessary to understand the atomic processes that govern the dynamics of individual atoms on the surfaces. In particular, knowledge of the occurrence rates of these processes is essential, since the length scales of the patterns formed on the surface are determined by the competition between different processes (driving versus relaxation).

Also relaxation dynamics of atomic steps was studied, as they give insight in the relevance of different atomic processes contributing to the step dynamics. Moreover, the studies of relaxation dynamics open a possibility for the experimental determination of the rates of the microscopic processes taking place on the surface.

Two different approaches to the problem of dynamics of vicinal surfaces were taken. To study the effect of different atomic processes on the large scale morphology of a growing surface, a Solid-on-Solid model was applied. The dynamics of the atomic steps on a coarse grained level were studied using partial differential equations, derived from the Burton-Cabrera-Frank model of crystal growth. The applied methods include both analytic and numerical analysis of partial differential equations, governing the time evolution of atomic steps, and Monte-Carlo simulations of the discrete Solid-on-Solid model.

The MC simulations of the SOS model showed that both, BZ- and KESE- instabilities, may occur within the same simple model. Which of the instabilities is dominating depends on the relevance of the step edge diffusion and the rate of atoms going around a kink-site in the step edge diffusion. The wavelength of the instabilities can be calculated analytically, and the simulation results were in good agreement with the theory. The asymptotic evolution of the step profile in the MC simulations differs from the prediction obtained from the step evolution equation describing the dynam-

ics of the BZ-instability; for the KESE instability the theory for asymptotic evolution is still missing. The results obtained in this work are also in partial agreement with the observations of a step meandering instability in growth experiments on vicinal Cu surfaces. The step instability observed on the Cu(1 1 17) surfaces, where the steps have a closed packed structure can be assigned to the KESE instability. Meandering instability has also been observed on the Cu(0 1 12) surface, which differs from the Cu(1 1 17) surface only by the orientation of the steps. On the Cu(0 1 12) surface the steps have an open structure, making the dynamics of the atoms along the steps quite different. This instability remains without explanation at the time.

Also the break-down of the step-flow growth mode through nucleation of islands on the terraces or appearance of vacancy islands was considered and some preliminary results were presented. The nucleation of islands may launch the formation of large mounds on the surface, making the morphology rather 3- than 2- dimensional. The mounding is asymptotically similar to the mounding on singular surfaces, which has been studied extensively in recent years. A strong meandering of steps may also lead to 3D morphology, if the step profile forms a closed loop, thus leading to the appearance of a vacancy island on the terraces. The vacancy island act as pinning centers for the following steps and may lead to formation of a deep crater on the surface.

Appendix A

Evolution equation for in-phase step train

The starting point for the derivation of an evolution equation for the in-phase ($\zeta_i \equiv \zeta$) step profile is the BCF theory introduced in Sect. 3.3. The attachment from the lower terrace is assumed infinitely fast ($k_+ \to \infty$) and from the upper terrace completely suppressed ($k_- = 0$).

$$\begin{aligned} D\nabla^2 c(x,y) + F &= 0 \\ \mathbf{n}\cdot\nabla c(x,\zeta+\ell) &= 0 \\ c(x,\zeta) = c^0_{eq}\Big(1+\beta\tilde{\gamma}\Omega\kappa(x)\Big) & \\ v^n(x) = \Omega D\mathbf{n}\cdot\nabla c(x\,,\zeta) - \sigma\Omega^2\tilde{\gamma}\partial_s^2\kappa(x). & \end{aligned} \tag{A.1}$$

The strategy is to expand all the equations in the long wavelength regime $q\ell \ll 1$ in the small parameter ϵ, defined in the text as [1]

$$\epsilon \equiv 2q_{BZ}\ell = \sqrt{\frac{F\ell^4}{\Omega\tilde{\gamma}\left(\sigma + \ell\beta D c^0_{eq}\right)}} \ll 1. \tag{A.2}$$

For the expansion one needs to know the leading order terms of the variables (see Sect. 5.2)

$$x \sim \epsilon^{-1}\ ,\ \zeta \sim \epsilon^{-1}\ ,\ t \sim \epsilon^{-4}\ ,\ c \sim \epsilon. \tag{A.3}$$

Defining now a new set of dimensionless variables, so that the leading order dependence on ϵ is scaled out

$$\begin{aligned} X &= \frac{\epsilon}{\ell}x\ ,\ Y = \frac{y-\zeta}{\ell}\ ,\ H = \frac{\epsilon}{\ell}\zeta \\ T &= \frac{\epsilon^4 D}{\ell^2}t\ ,\ U = \epsilon^{-1}\Omega(c - c^0_{eq}) \end{aligned} \tag{A.4}$$

[1] In the original work [24, 64] the expansion parameter is ϵ^2

the BCF equations read

$$\begin{aligned}
\epsilon^2\partial_X^2 U + \epsilon\left[\eta - 2(\partial_X H)(\partial_{XY}U) - (\partial_X^2 H)(\partial_Y U)\right] + \rho^2\partial_Y^2 U &= 0 \\
U|_{Y=0} &= -K \\
\rho\partial_Y U|_{Y=1} &= \epsilon(\partial_X H)(\partial_X U)|_{Y=1} \\
(\ell/D)v_0 + \epsilon^3\partial_T H &= \left[\epsilon\rho^2\partial_Y U - \epsilon^2(\partial_X H)(\partial_X U)\right]|_{Y=0} - \epsilon^3\alpha\partial_X\left[\frac{1}{\rho}\partial_X K\right],
\end{aligned} \tag{A.5}$$

where all variables are now of the order $F \sim \epsilon^0$ at most. To keep the notation as simple as possible

$$\begin{aligned}
\eta &\equiv \frac{\Omega F\ell^2}{\epsilon^2 D}(\sim\epsilon^0) \quad , \quad \rho \equiv \sqrt{1+(\partial_X H)^2} \\
K &\equiv \frac{\Omega^2 c_{eq}^0\tilde{\gamma}}{kT\ell}\frac{\partial_{XX}H}{\rho^3} \quad , \quad \alpha \equiv \frac{\sigma kT}{D\ell c_{eq}^0}
\end{aligned} \tag{A.6}$$

Now power series expansions $H = H_0 + \epsilon H_1 + \epsilon^2 H_2 ...$ and $U = U_0 + \epsilon U_1 + \epsilon^2 U_2 ...$ [2]can be inserted into Eqs. (A.5) and the resulting equations solved recursively for each order. One sees that the lowest order equation for the time derivative reads

$$\begin{aligned}
\partial_T H_0 &= \left[\rho_0\partial_Y U_2 + 2\rho_0\rho_1\partial_Y U_1 - (\partial_X H_0)(\partial_X U_1) - (\partial_X H_1)(\partial_X U_0)\right]|_{Y=0} \\
&- \alpha\partial_X\left(\frac{1}{\rho_0}\partial_X K_0\right).
\end{aligned} \tag{A.7}$$

To obtain the time evolution equation one must solve the equation up to second order for U and first order for H.

ϵ^0:

$$\begin{aligned}
\partial_Y^2 U_0 &= 0 && && U_0 = A^{(0)}Y + B^{(0)} \\
U_0|_{Y=0} &= -K_0 && \Longrightarrow && A^{(0)} = 0 \\
\partial_Y U_0|_{Y=1} &= 0 && && B^{(0)} = -K_0
\end{aligned} \tag{A.8}$$

[2]Note that also $\rho(H)$ and $K(H)$ must be expanded in ϵ

ϵ^1:

$$\rho_0 \partial_Y^2 U_1 + \eta = 0 \qquad \Rightarrow \qquad U_1 = \frac{-\eta}{2\rho_0} Y^2 + A^{(1)} Y + B^{(1)} \tag{A.9}$$

And from the b.c.'s:

$$\begin{aligned} U(1)|_{Y=0} = -K_1 \qquad &\Rightarrow \qquad B^{(1)} = -K_1 \\ \left[\rho_0^2 \partial_Y U_1 - (\partial_X H_0)(\partial_X U_0)\right]|_{Y=1} = 0 \qquad &\Rightarrow \qquad A^{(1)} = \frac{\eta - (\partial_X H_0)(\partial_X K_0)}{\rho_0^2} \end{aligned} \tag{A.10}$$

With these results the velocity of a straight step v_0 can be calculated

$$\begin{aligned} \frac{\ell}{D} v_0 &= \epsilon^2 \left[\rho_0^2 \partial_Y U_1 - (\partial_X H_0)(\partial_X U_0)\right]|_{Y=0} = \epsilon^2 \eta \\ &\Rightarrow v_0 = \Omega F \ell \end{aligned} \tag{A.11}$$

ϵ^2:

$$\rho_0^2 \partial_Y^2 U_2 + 2\rho_0 \rho_1 \partial_Y^2 U_1 - 2(\partial_X H_0)(\partial_{XY} U_1) - (\partial_X^2 H_0)(\partial_Y U_1) + \partial_Y^2 U_0 = 0 \tag{A.12}$$

Substituting from Eqs.(A.8) and (A.9) yields

$$\begin{aligned} \partial_Y^2 U_2 &= \left[-2(\partial_X H_0)\partial_X \left(\frac{\eta}{\rho_0^2}\right) - (\partial_X^2 H_0)\frac{\eta}{\rho_0^2}\right] \frac{Y}{\rho_0^2} \\ &+ \left[2\rho_1 \frac{\eta}{\rho_0} + 2(\partial_X H_0)(\partial_X A^{(1)}) + (\partial_X^2 H_0) A^{(1)} - \partial_X^2 B^{(0)}\right] \frac{1}{\rho_0^2} \\ &\equiv aY + b \\ \Rightarrow U_2 &= \frac{aY^3}{6} + \frac{bY^2}{2} + A^{(2)} Y + B^{(2)} \end{aligned} \tag{A.13}$$

The BC's then yield for $A^{(2)}, B^{(2)}$

$$\begin{aligned} B^{(2)} &= -K_2 \\ \left[\rho_0^2 \partial_Y U_2 + 2\rho_0 \rho_1 \partial_Y U_1 - (\partial_X H_0)(\partial_X U_1) - (\partial_X H_1)(\partial_X U_0)\right]|_{Y=1} &= 0 \end{aligned} \tag{A.14}$$

$$\begin{aligned} \Rightarrow \rho_0^2 A^{(2)} &= (\partial_X H_0)\partial_X \left(A^{(1)} + B^{(1)} - \frac{\eta}{2\rho_0^2}\right) + (\partial_X H_1)(\partial_X B^{(0)}) \\ &- \rho_0^2 \left(\frac{a}{2} + b\right) + 2\rho_0 \rho_1 \left(\frac{\eta}{\rho_0^2} - A^{(1)}\right) \end{aligned} \tag{A.15}$$

The time evolution equation (A.7) can be written in a closed from using these results:

$$\begin{aligned}\partial_T H_0 &= \rho_0^2 A^{(2)} + 2\rho_0\rho_1 A^{(1)} - (\partial_X H_0)(\partial_X B^{(1)}) \\ &- (\partial_X H_1)(\partial_X B^{(0)}) - \alpha\partial_X\left(\frac{1}{\rho_0}\partial_X K_0\right)\end{aligned} \tag{A.16}$$

Substituting first $\rho_0^2 A^{(2)}$ from (A.15) gives

$$\begin{aligned}\partial_T H_0 &= (\partial_X H_0)\partial_X\left(A^{(1)} - \frac{\eta}{2\rho_0^2}\right) - \rho_0^2\left(\frac{a}{2} + b\right) + 2\rho_1\frac{\eta}{\rho_0} \\ &- \alpha\partial_X\left(\frac{1}{\rho_0}\partial_X K_0\right).\end{aligned} \tag{A.17}$$

Inserting a and b, defined in Eq. (A.13) yields

$$\begin{aligned}\partial_T H_0 &= (\partial_X H_0)\partial_X\left(A^{(1)} - \frac{\eta}{2\rho_0^2}\right) + (\partial_X H_0)\partial_X\left(\frac{\eta}{\rho_0^2}\right) \\ &+ \frac{1}{2}(\partial_X^2 H_0)\frac{\eta}{\rho_0^2} - 2\rho_1\frac{\eta}{\rho_0} - 2(\partial_X H_0)(\partial_X A^{(1)}) - (\partial_X^2 H_0)A^{(1)} \\ &+ \partial_X^2 B^{(0)} + 2\rho_1\frac{\eta}{\rho_0} - \alpha\partial_X\left(\frac{1}{\rho_0}\partial_X K_0\right) \\ &= -\partial_X\left[\,(\partial_X H_0)A^{(1)}\right] + \frac{1}{2}\partial_X\left[(\partial_X H_0)\frac{\eta}{\rho_0^2}\right] + \partial_X^2 B^{(0)} - \alpha\partial_X\left(\frac{1}{\rho_0}\partial_X K_0\right).\end{aligned} \tag{A.18}$$

And finally, inserting expressions $A^{(1)}, B^{(0)}$ leads to

$$\begin{aligned}\partial_T H_0 &= -\partial_X\left[(\partial_X H_0)\frac{\eta - (\partial_X H_0)(\partial_X K_0)}{\rho_0^2}\right] \\ &+ \frac{1}{2}\partial_X\left[(\partial_X H_0)\frac{\eta}{\rho_0^2}\right] - \partial_X^2 K_0 - \alpha\partial_X\left(\frac{1}{\rho_0}\partial_X K_0\right) \\ &= -\partial_X\left[\frac{\eta}{2}\frac{\partial_X H_0}{\rho_0^2} + (1+\alpha\rho_0)\frac{\partial_X K_0}{\rho_0^2}\right],\end{aligned} \tag{A.19}$$

which after scaling back to physical quantities reads

$$\begin{aligned}\frac{\partial\zeta}{\partial t} &= -\partial_x\left\{\frac{\Omega F\ell^2}{2}\frac{\partial_x\zeta}{1+(\partial_x\zeta)^2}\right. \\ &+ \left.\left(\frac{\Omega^2\beta D\ell c_{eq}\tilde{\gamma}}{1+(\partial_x\zeta)^2} + \frac{\sigma\Omega^2\tilde{\gamma}}{\sqrt{1+(\partial_x\zeta)^2}}\right)\partial_x\left[\frac{\partial_{xx}\zeta}{(1+\partial_x\zeta)^2)^{3/2}}\right]\right\}.\end{aligned} \tag{A.20}$$

References

[1] T. Ala-Nissila, R. Ferrando, and S. C. Ying, *Collective and single particle diffusion on surfaces*, Adv. Phys. **51**, 949 (2002).

[2] T. Ala-Nissila and S. C. Ying, *Theory of Classical Surface Diffusion*, Prog. Surf. Sci. **39**, 227 (1992).

[3] G. S. Bales, *Crossover scaling during submonolayer epitaxy on vicinal substrates*, Surf. Sci. **356**, L439 (1996).

[4] G. S. Bales and A. Zangwill, *Morphological instability of a terrace edge during step flow growth*, Phys. Rev. B **41**, 5500 (1990).

[5] A. L. Barabási and H. E. Stanley, *Fractal concepts in surface growth* (Cambridge University Press, Cambridge, 1995).

[6] M. C. Bartelt and J. W. Evans, *Scaling analysis of diffusion-meditated island growth in surface adsorption processes*, Phys. Rev. B **46**, 12675 (1992).

[7] I. Bena, C. Misbah, and A. Valance, *Nonlinear evolution of a terrace edge during step-flow growth*, Phys. Rev. B **47**, 7408 (1993).

[8] A. Bortz, M. Kalos, and J. Lebowitz, *A new algorithm for Monte Carlo simulation of Ising spin systems*, J. Comp. Phys. **17**, 10 (1975).

[9] K. Bromann, H. Brune, H. Roder, and K. Kern, *Interlayer mass-trnasprt in homoepitaxial and heteroepitaxial metal growth*, Phys. Rev. Lett. **75**, 677 (1995).

[10] W. K. Burton, N. Cabrera, and F. C. Frank, *The growth of crystals and the equilibrium structure of their surfaces*, Phil. Trans. R. Soc. London **243A**, 299 (1951).

[11] A. M. Cadilhe, C. R. Stoldt, C. J. Jenks, P. A. Thiel, and J. W. Evans, *Evolution of far-from-equilibrium nanostructures on Ag (100) surfaces: Protrusions and indentations at extended step edges*, Phys. Rev. B **61**, 4910 (2000).

[12] P. M. Chaikin and T. C. Lubensky, *Principles of condensed matter physics* (Cambridge University Press, Cambridge, 1995).

[13] P. Šmilauer and D. Vvedensky, *Coarsening and slope evolution during unstable spitaxial growth*, Phys. Rev. B **52**, 14263 (1995).

[14] F. Buatier de Mongeot, G. Costantini, C. Boragno, and U. Valbusa, *Mound shape instability in multilayer Ag (001) homoepitaxy: The role of corner-crossing*, Europhys. Lett. **58**, 537 (2002).

[15] M. C. Desjonquères and D. Spanjaard, *Concepts in surface physics*, 2nd ed. (Springer, Berlin, 1996).

[16] G. Ehrlich and F. G. Hudda, *Atomic view of surface diffusion: tungsten on tungsten*, J. Chem. Phys **44**, 1039 (1966).

[17] H. J. Ernst, F. Fabre, R. Folkerts, and J. Lapujoulade, *Observation of a growth instability during low-temperature molecular-beam epitaxy*, Phys. Rev. Lett. **72**, 112 (1994).

[18] R. Ghez and S. S. Iyer, *The kinetics of fast steps on crystal surfaces and its application to the molecular beam epitaxy of silicon*, IBM Res. Dev. **32**, 804 (1988).

[19] M. Giesen, *Scaling transition of the time dependence of step fluctuations on Cu(111)*, Surf. Sci. **442**, 543 (1999).

[20] M. Giesen, *Step and island dynamics at solid/vacuum and solid/liquid interfaces*, Prog. Surf. Sci. **68**, 1 (2001).

[21] M. Giesen, C. Steimer, and H. Ibach, *What does one learn from equilibrium shapes of two-dimensional islands on surfaces?*, Surf. Sci. **471**, 80 (2001).

[22] M. Giesen-Seibert, R. Jentjens, M. Poensgen, and H. Ibach, *Time dependence of step fluctuations on vicinal Cu(1 1 19) surfaces investigated by tunneling microscopy*, Phys. Rev. Lett. **71**, 3521 (1993).

[23] M. Giesen-Seibert, F. Schmitz, R. Jentjens, and H. Ibach, *Time fluctuations of steps on Cu(11n) surfaces investigated by temperature variable tunneling microscopy*, Surf. Sci. **329**, 47 (1995).

[24] F. Gillet, O. Pierre-Louis, and C. Misbah, *Non-linear evolution of step meander during growth of a vicinal surface with no desorption*, Eur. Phys. J. B **18**, 519 (2000).

[25] S. Heinrichs, J. Rottler, and P. Maas, *Nucleation on top of islands in epitaxial growth*, Phys. Rev. B **62**, 8338 (2000).

[26] M. A. Herman and H. Sitter, *Molecular beam epitaxy: fundamentals and current status* (Springer, Berlin, 1989).

[27] H. Ibach, M. Giesen, G. S. Icking-Konert, and D. Stapela, *Step fluctuations on Pt(111) surfaces*, Surf. Sci. **366**, 229 (1996).

[28] T. Ihle, C. Misbah, and O. Pierre-Louis, *Equilibrium step dynamics on vicinal surfaces revisited*, Phys. Rev. B **58**, 2289 (1998).

[29] H. C. Jeong and E. D. Williams, *Steps on surfaces: experiment and theory*, Surf. Sci. Rep. **34**, 171 (1999).

[30] M. Kalff, G. Comsa, and T. Michely, *How Sensitive is Epitaxial Growth to Adsorbates?*, Phys. Rev. Lett. **81**, 1255 (1998).

[31] H. Kallabis, *Theoretical aspects of crystal growth* (PhD Dissertation, University of Duisburg, Duisburg, 1997).

[32] J. Kallunki and J. Krug, *Asymptotic step profiles from a nonlinear growth equation for vicinal surfaces*, Phys. Rev. E **62**, 6229 (2000).

[33] J. Kallunki and J. Krug, *Effect of kink-rounding barriers on step edge fluctuations*, Surf. Sci. **523**, L53 (2003).

[34] J. Kallunki, J. Krug, and Miroslav Kotrla, *Competing mechanisms for step meandering in unstable growth*, Phys. Rev. B **65**, 205411 (2002).

[35] G. L. Kellogg, *Field ion microscope investigations of adatom and dimer diffusion along Rh(100) step edges*, Surf. Sci. **359**, 237 (1996).

[36] M. Kotrla, *Numerical simulations in the theory of crystal growth*, Comp. Phys. Comm. **97**, 82 (1996).

[37] J. Krug, *Origins of scale invariance in growth processes*, Adv. Phys. **46**, 139 (1997).

[38] J. Krug, *Pattern-forming instabilities in homoepitaxial crystal growth*, Physica A **263**, 174 (1999).

[39] J. Krug, *Four lectures on the physics of crystal growth*, Physica A **313**, 47 (2002).

[40] J. Krug, H. T. Dobbs, and S. Majaniemi, *Adatom mobility for the solid-on-solid model*, Z. Phys. B **97**, 281 (1995).

[41] J. Krug and P. Meakin, *Kinetic roughening of Laplacian fronts*, Phys. Rev. Lett. **66**, 703 (1991).

[42] J. Krug, P. Politi, and T. Michely, *Island nucleation in the presence of step-edge barriers: Theory and applications*, Phys. Rev. B **61**, 14037 (2000).

[43] J. Krug and M. Schimschak, *Metastability of Step Flow Growth in 1+1 Dimensions*, J. Phys. I France **5**, 1065 (1995).

[44] R. Kunkel, B. Poelsema, L. Verheij, and G. Comsa, *Reentrant layer-by-layer growth during molecular-beam epitaxy of metal-on-metal substrates*, Phys. Rev. Lett. **65**, 733 (1990).

[45] K. Kyono and G. Ehrlich, *Step-edge barroers: truths and kinetic consequences*, Surf. Sci. **383**, 766 (1997).

[46] C. J. Lanczycki, R. Kotlyar, E. Fu, Y. N. Yang, E. D. Williams, and S. Das Sarma, *Growth of Si on the Si(111) surface*, Phys. Rev. B **57**, 13132 (1998).

[47] D. P. Landau and K. Binder, *Monte Carlo simulations in statistical physics* (Cambridge University Press, Cambridge, 2000).

[48] A. C. Levi and M. Kotrla, *Theory and simulation of crystal growth*, J. Phys.: Cond. Mat **9**, 299 (1997).

[49] I. V. Markov, *Crystal growth for beginners: fundamentals of nucleation, crystal growth and epitaxy* (World Scientific, Singapore, 1995).

[50] T. Maroutian, *Étude expérimentale d'instabilités de croissance des faces vicnales* (PhD Dissertation, Université Paris 7, Paris, 2001).

[51] T. Maroutian, L. Douillard, and H.-J. Ernst, *Wavelength selection in unstable homoepitaxial step flow growth*, Phys. Rev. Lett. **83**, 4353 (1999).

[52] T. Maroutian, L. Douillard, and H.-J. Ernst, *Morphological instability of Cu vicinal surfaces during step-flow growth*, Phys. Rev. B **64**, 165401 (2001).

[53] H. Mehl, O. Biham, I. Furman, and M. Karimi, *Models for adatom diffusion on fcc (001) metal surfaces*, Phys. Rev. B **60**, 2106 (1999).

[54] J. Merikoski, I. Vattulainen, J. Heinonen, and T. Ala-Nissila, *Effect of kinks and concerted diffusion mechanisms on mass transport and growth on stepped metal surfaces*, Surf. Sci. **387**, 167 (1997).

[55] K. Morgenstern, G. Rosenfeld, E. Laegsgaard, F. Besenbacher, and G. Comsa, *Measurement of energies controlling ripening and annealing on metal surfaces*, Phys. Rev. Lett. **80**, 556 (1998).

[56] M. V. Ramana Murty and B. H. Cooper, *Instability in Molecular Beam Epitaxy due to Fast Edge Diffusion and Corner Diffusion Barriers*, Phys. Rev. Lett. **83**, 352 (1999).

[57] J. Mysliveček, C. Schelling, F. Schäffler, G. Springholz, P. Šmilauer, J. Krug, and B. Voigtlander, *On the microscopic origin of the kinetic step bunching instability on vicinal Si(001)*, Surf. Sci. **520**, 193 (2002).

[58] N. Néel and L. Douillard, private communication.

[59] J. E. Van Nostrand, S. J. Chey, and D. G. Cahill, *Low-temperature growth morphology of singular and vicinal Ge(001)*, Phys. Rev. B **57**, 12536 (1998).

[60] D. W. Pashley, *A historical review of epitaxy*, in Epitaxial Growth ed. J. W. Matthews, Part A 2 (1975).

[61] O. Pierre-Louis, private communication.

[62] O. Pierre-Louis, *Step bunching with general step kinetics: stability analysis and macroscopic models*, Surf. Sci. **529**, 114 (2003).

[63] O. Pierre-Louis, M. R. D'Orsogna, and T. L. Einstein, *Edge diffusion during growth: The kink Ehrich-Schwoebel effect and resulting instabilities*, Phys. Rev. Lett. **82**, 3661 (1999).

[64] O. Pierre-Louis, C. Misbah, Y. Saito, J. Krug, and P. Politi, *New nonlinear equation for steps during molecular beam epitaxy on vicinal surfaces*, Phys. Rev. Lett. **80**, 42212 (1998).

[65] A. Pimpinelli, I. Elkiani, A. Karma, C.Misbah, and J. Villain, *Step motions on a high-temperature vicinal surface*, J. Phys. Cond. Mat. **6**, 2661 (1994).

[66] A. Pimpinelli and J. Villain, *Physics of crystal growth* (Cambridge University Press, Cambridge, 1998).

[67] A. Pimpinelli, J. Villain, and D. E. Wolf, *Fractal terraces in MBE growth*, J. Phys I (France) **3**, 447 (1993).

[68] A. Pimpinelli, J. Villain, D. E. Wolf, J. J. Métois, J. C. Heyraud, I. Elkiani, and G. Uimin, *Equilibrium step dynamics on vicinal surfaces*, Surf. Sci. **295**, 1434 (1993).

[69] P. Politi, *Different regimes in the Ehrlich-Schwoebel instability*, J. Phys. I **7**, 797 (1997).

[70] P. Politi and C. Castellano, *Process of irreversible nucleation in multilayer growth. I. Failure of the mean-field approach*, Phys. Rev. E **66**, 031605 (2002).

[71] P. Politi, G. Grenet, A. Marty, A. Ponchet, and J. Villain, *Instabilities in crystal growth by atomic or molecular beams*, Phys. Rep. **324**, 271 (2000).

[72] P. Politi and J. Krug, *Crystal symmetry. step-edge diffusion and unstable growth*, Surf. Sci. **446**, 89 (2000).

[73] P. Politi and A. Torcini, *Coarsening in surface growth models without slope selection*, J. Phys. A **33**, L77 (2000).

[74] P. Politi and J. Villain, *Ehrlich-Schwoebel instability in molecular-beam epitaxy: A minimal model*, Phys. Rev. B **54**, 5114 (1996).

[75] W. H. Press, S. A. Teukolsky, W. T. Vetterling, and B. P. Flannery, *Numerical recipes in C: The art of scientific computing* (Cambridge University Press, New York, 1992).

[76] M. Rost, P. Šmilauer, and J. Krug, *Unstable epitaxy on vicinal surfaces*, Surf. Sci. **369**, 393 (1996).

[77] M. Rusanen, private communication.

[78] M. Rusanen, I. T. Koponen, T. Ala-Nissila, C. Ghosh, and T. S. Rahman, *Morphology of ledge patterns during step flow growth of metal surfaces vicinal to fcc (001)*, Phys. Rev. B **65**, 041404(R) (2002).

[79] M. Rusanen, I. T. Koponen, J. Heinonen, and T. Ala-Nissila, *Instability and wavelength selection during step-flow growth of metal surfaces vicinal to fcc(001)*, Phys. Rev. Lett. **86**, 5317 (2001).

[80] M. Rusanen, I. T. Koponen, and J. Kallunki, *Mixing the length scales: step meandering and island nucleation on vicinal surfaces*, Submitted to Eur. Phys. J. B (2003).

[81] Schwenger, R. L. Folkerts, and H.J. Ernst, *Bales-Zangwill meandering instability observed in homoepitaxial step-flow growth*, Phys. Rev. B **55**, 7406 (1997).

[82] R. L. Schwoebel and E. J. Shipsey, *Step motion on crystal surfaces*, J. Appl. Phys. **37**, 3682 (1966).

[83] V. A. Shchukin and D. Bimberg, *Spontaneous ordering of nanostructures on crystal surfaces*, Rev. Mod. Phys. **71**, 1125 (1999).

[84] M. Siegert, *Coarsening Dynamics of Crystalline Thin Films*, Phys. Rev. Lett. **81**, 5481 (1998).

[85] P. Stoltze, *Simulation of surface defects*, J. Phys.: Cond. Mat. **6**, 9495 (1994).

[86] S. Stoyanov, *New type of step bunching instability at vicinal surfaces in crystal evaporation affected by electromigration*, Surf. Sci. **416**, 200 (1998).

[87] R. Stumpf and M. Scheffler, *Theory of self-diffusion and growth of Au(111)*, Phys. Rev. Lett. **72**, 254 (1994).

[88] B. S. Swartzentruber, N. Kitamura, M. G. Lagally, and M. B. Webb, *Behavior of steps on Si(001) as a function of vicinality*, Phys. Rev. B **47**, 13432 (1993).

[89] Lei-Han Tang, P. Šmilauer, and D. D. Vvedensky, *Noise-assisted mound coarsening in epitaxial growth*, Eur. Phys. J. B **2**, 409 (1998).

[90] C. Teichert, *Self-organization of nanostructures in semiconductor heteroepitaxy*, Phys. Rep. **365**, 335 (2002).

[91] P. Tejedor, P. Šmilauer, P. C. Roberts, and B. A. Joyce, *Surface-morphology evolution during unstable homoepitaxial growth of GaAs(110)*, Phys. Rev. B **59**, 2341 (1999).

[92] K. Thurmer, R. Koch, M. Weber, and K. H. Rieder, *Dynamic evolution of pyramid structures during growth of epitaxial Fe(001) films*, Phys. Rev. Lett. **75**, 1767 (1995).

[93] N. G. van Kampen, *Stochastic processes in physics and chemistry* (Cambridge University Press, Cambridge, 1998).

[94] J. Villain, *Continuum models for crystal growth from atomic beams with and without desorption*, J. de Physique I **1**, 19 (1991).

[95] J. Villain and A. Pimpinelli, *Physique de la Croissance Cristalline* (Éditions Eyrolles, Paris, 1995).

[96] D. E. Wolf, *Computer simulation of molecular beam epitaxy*, in Scale invariance, interfaces and non-equilibrium dynamics ed. M. Droz, A. J. McKane, J. Vannimenus and D. E. Wolf 215 (1994).

[97] Z. Zhang and M. G. Lagally, *Atomistic processes in the early stages of thin-film growth*, Science **276**, 377 (1997).

[98] J. Zhong, T. Zhang, Z. Zhang, and M. G. Lagally, *Island-corner barrier effect in two-dimensional pattern formation at surfaces*, Phys. Rev. B **63**, 113403 (2001).

[99] J. K. Zuo and J. F. Wendelken, *Evolution of mound morphology in reversible homoepitaxy on Cu(100)*, Phys. Rev. Lett. **78**, 2791 (1997).

Acknowledgement

I would like to thank the numerous people who have helped me on the way in finishing this work. In particular, I thank Prof. Joachim Krug for the excellent guidance throughout the work. I am also grateful to Tapio Ala-Nissilä, Claudio Castellano, Jens Eggers, Heike Emmerich, Ismo Koponen, Miroslav Kotrla, Olivier Pierre-Louis, Paolo Politi, Marko Rusanen and many others for the enlightening scientific (and non-scientific) discussions. I am grateful to Ludovic Douillard, Hans-Joachim Ernst and Nicolas Néel for providing experimental results.

I also wish to thank Philipp Kuhn, Christian Karl, Uwe Börner, Henryk Pinnow, Carlos Viviescas and the whole department of theoretical physics of University of Essen for the friendly working atmosphere. Particular thanks goes to Rüdiger Oberhage for the assistance in the everlasting battle with the computers.

And last, but certainly not least, I thank Licia for her priceless support during the whole period.

Apart from the University of Essen, this work has been done during the enjoyable visits in MPI für Physik komplexer Systeme in Dresden, Université Joseph Fourier in Grenoble, Academy of Sciences of the Czech Republic in Prague and Technical University of Helsinki, which I thank for their hospitality

This work has been financed by the Deutsche Forschungsgemeinschaft within the SFB 237.